Electrodynamics of Non-topological Solitons

by

Michael Peter Kinach

A THESIS SUBMITTED IN PARTIAL FULFILLMENT
OF THE REQUIREMENTS FOR THE DEGREE OF

Doctor of Philosophy

in

THE FACULTY OF GRADUATE AND POSTDOCTORAL STUDIES
(Physics)

The University of British Columbia
(Vancouver)

December 2024

The following individuals certify that they have read, and recommend to the Faculty of Graduate and Postdoctoral Studies for acceptance, the thesis entitled:

Electrodynamics of Non-topological Solitons

submitted by **Michael Peter Kinach** in partial fulfillment of the requirements for the degree of **Doctor of Philosophy** in **Physics**.

Examining Committee:

Matthew Choptuik, Professor, Physics and Astronomy, University of British Columbia
Supervisor

Jeremy Heyl, Professor, Physics and Astronomy, University of British Columbia
Supervisory Committee Member

Chen Greif, Professor, Computer Science, University of British Columbia
University Examiner

Joerg Rottler, Professor, Physics and Astronomy, University of British Columbia
University Examiner

Vitor Cardoso, Professor, Physics, University of Copenhagen and University of Lisbon
External Examiner

Additional Supervisory Committee Members:

Stefan Reinsberg, Associate Professor, Physics and Astronomy, University of British Columbia
Supervisory Committee Member

Moshe Rozali, Professor, Physics and Astronomy, University of British Columbia
Supervisory Committee Member

Abstract

In this thesis, we study a class of non-topological solitons known as "Q-balls" which arise in complex scalar field theories with $U(1)$ symmetry. We focus on the case where the $U(1)$ symmetry is gauged and the theory admits a coupling to electromagnetism; the corresponding solitons are known as "gauged Q-balls". Using numerical simulations, we examine the dynamical behaviour of these objects in various scenarios. First, we investigate the classical stability of gauged Q-balls under assumptions of axial symmetry. Considering two different forms for the scalar field potential, we find evidence for gauged Q-ball configurations which remain stable with respect to axisymmetric perturbations of the fields. We also find evidence for unstable configurations which are quickly destroyed in response to the perturbations (for example, through dispersal of the fields or via fragmentation into smaller structures). Next, we investigate head-on collisions of gauged Q-balls at relativistic velocities. We test the effects of the electromagnetic coupling strength, initial velocity, relative phase, and relative charge of the colliding binary on the outcome of the collision. Depending on the values of these parameters, we observe a variety of distinct phenomena such as gauged Q-ball mergers, fragmentation, charge transfer, charge annihilation, Q-ring formation, and electromagnetic radiation production. Finally, we investigate the dynamics of gauged Q-balls using fully three-dimensional numerical simulations. Extending the previous analyses, we find evidence for configurations which remain classically stable against generic perturbations in three spatial dimensions. We also consider off-axis collisions of gauged Q-balls and find that the impact parameter can play a significant role in determining the outcome of the collision. Together, these results address several key questions about the dynamics of non-topological solitons in general and the stability of gauged Q-balls in particular.

Lay Summary

Many physical processes can be described in terms of waves. Typically, we imagine waves as being dispersive: they spread out and lose their identity as time marches on. However, under the proper circumstances, we can also find examples of waves which remain forever localized and coherent. These special waves are known as *solitons*. In this thesis, we use computer simulations to study how electromagnetic fields can influence soliton behaviour in one particular model. Our simulations show that electromagnetic effects can play a significant role—in some cases, they cause the solitons to quickly fall apart, while in other cases, they lead to the formation of entirely new structures. We also find that high-energy collisions of these solitons can be extremely violent processes which exhibit a range of extraordinary phenomena. Ultimately, we expect these results to be important for understanding the many physical scenarios in which solitons naturally arise.

Preface

This thesis contains the original work of Michael P. Kinach (MPK) with supervision from Matthew W. Choptuik (MWC). The content of Chapter 2, Chapter 3, and Chapter 4 has previously been published in [1], [2], and [3], respectively. In these chapters, MPK performed all calculations, developed the necessary research software, performed the data analysis, and wrote the manuscripts. MWC assisted with the identification of the research problem, offered technical advice at various stages, and provided feedback on the manuscripts. Chapter 1 contains background information on the research problem which is summarized from the cited sources.

Table of Contents

List of Tables

List of Figures

Acknowledgments

I would like to express my gratitude to the many individuals who have supported me during my graduate studies. First and foremost, I thank my advisor, Matthew Choptuik, for his mentorship and guidance. I am also very grateful to Matt for giving me considerable freedom in choosing the topic and direction of this thesis. Second, I thank the members of my graduate committee (Jeremy Heyl, Moshe Rozali, and Stefan Reinsberg) for generously sharing their time and feedback. Third, I thank my colleagues in the Choptuik research group for their assistance and camaraderie over the years. Finally, I thank my friends and family for their support from the beginning—you know who you are.

Chapter 1

Introduction

Advancements in computing technology have consistently driven scientific progress and discovery. In the past fifty years, processing power has grown exponentially; so, too, has the scale of problems which can be solved with computer software. Today, one could say that scientific computing has reached a state of maturity. It is now a standard practice to use hundreds or thousands of computer cores to address research questions in many disciplines. This is especially prevalent in technical fields (such as theoretical physics) where a significant level of mathematical sophistication is required to make progress on modern problems. With increasing frequency, numerical algorithms are being called upon to handle these complexities and to provide insights into physical theory. At the same time, numerical approaches are also revealing new dynamical solutions which may be difficult—or outright impossible—to treat exactly. There are many different classes of these solutions in field theory. In this thesis, we will use computational methods to study one notable example: the coherent, particle-like objects known as *solitons*.

In casual terms, a soliton can be described as a stable, localized "lump of energy" [4] which propagates at a constant speed and with a constant shape. They arise in many areas of Nature ranging from biology to fluid mechanics to particle physics (see [5] for a review) where the dynamics are governed by non-linear wave equations. More precisely, a soliton can be defined as any classical solution of a non-linear field theory whose energy density remains localized in space and which can travel undistorted at a constant velocity[1]. With this definition, a soliton resembles a rudimentary model of a particle which can be constructed from smooth classical fields and which has a finite total energy. This has made them particularly attractive in theoretical physics as a simple model for matter.

[1] In some fields, the definition of a soliton also requires that they are not deformed during scattering processes involving other solitons [6]. Solutions which do not obey this condition are sometimes called *solitary waves*. Here we will adopt the practice which is common in high-energy physics of using "soliton" interchangeably with "solitary wave" [7].

When discussing solitons, it is useful to highlight how they differ from ordinary wavepackets. It is well-known that basic wave equations (for example, the Klein-Gordon equation) permit wavepacket solutions which outwardly resemble solitons. These solutions can be described in terms of their Fourier modes as the sum of many waveforms with distinct frequencies. Over short timescales or small distances, these wavepackets can even propagate as particle-like "lumps" whose energy density remains localized. However, this behaviour cannot be maintained indefinitely because the dynamics of each Fourier mode will be governed by a dispersion relation which is generally non-trivial. For all but the simplest wave equations, this relation will dictate that each mode corresponds to a different phase velocity, resulting in the eventual dispersal of the wavepacket. In order to counteract this natural tendency, it is typically required that the equations of the theory include explicit non-linearities or some topological constraint. These properties can provide the necessary restoring force to balance the dispersion and give rise to solitons.

The study of solitons began in 1834 with John Scott Russell's observations of shallow-water waves moving in a narrow channel [8]. These initial observations were given a full analytic treatment by Korteweg and de Vries in 1895 [9]. However, little further work was done on the subject until the revival of the field by Fermi, Pasta, Ulam, and Tsingou in 1955 [10]. Leveraging the computational advances of the time, they were among the first to apply numerical analysis to the study of soliton behaviour (in this case, to the study of waves propagating along one-dimensional lattices of coupled oscillators). In 1965, Zabusky and Kruskal coined the term "soliton" to describe the non-dispersive phenomena they observed during numerical experiments involving the Korteweg–de Vries equation [11]. Around the same time, Skyrme proposed a soliton model for the nucleon [12, 13] (the so called "skyrmion") while Toda described soliton behaviour in the context of solid-state physics [14, 15]. In the latter half of the twentieth-century, a serious research effort began to emerge in response to these early discoveries.

Generally speaking, solitons can be classified into two main categories: *topological* or *non-topological*. Topological solitons are characterized as field configurations which cannot be continuously deformed into one another due to constraints on the space of non-singular finite-energy solutions which can exist in the model (i.e., due to topological constraints). The classic example of topological solitons are the "kink" and "anti-kink" solutions which can arise in theories of a real scalar field in one spatial dimension with quartic non-linearities [6]. In this case, the potential of the theory supports degenerate minima which the field must approach at the spatial boundaries in order to ensure a finite total energy. If the field tends toward distinct minima at each of these boundaries, the solution becomes non-trivial and resembles a sigmoid-shaped "kink" which smoothly interpolates between the minima. Likewise, there exists a dual solution which interpolates between the minima in the opposite

direction (the "anti-kink"). No matter how the field evolves according to the equations of motion, these solutions cannot be continuously transformed into one another (or into the trivial solution) without violating the requirement of finite total energy. This provides a mechanism to stabilize the solitons. Besides the kink and anti-kink, there are many other types of topological solitons in field theory. Some notable examples include monopoles, vortices, domain walls, and skyrmions [16].

In some cases, one can find solitons which are not contingent upon the topology of the underlying model. These solitons (which are said to be "non-topological") instead arise due to a competition between attractive non-linear effects and the intrinsic dispersion of the equations of motion. Additionally, these solitons are often characterized by the presence of conserved quantities which are associated with the symmetries of the theory. The shallow-water waves first observed by Russell were of this type [17]. However, the existence of a general class of non-topological solitons in D spatial dimensions is severely restricted by Derrick's theorem [18] which states that static real scalar field configurations with a non-trivial potential cannot be stable for $D > 1$. In order to obtain non-topological solitons in higher spacetime dimensions, one is typically required to introduce additional fields or consider solutions with some internal time dependence. Among the many possibilities in this regard, perhaps the simplest examples are the bound configurations of a complex scalar field known as *Q-balls*.

1.1 Overview of Q-balls

Q-balls are non-topological solitons arising in complex scalar field theories with $U(1)$ symmetry and a non-linear attractive potential. The Lagrangian density of a typical theory can be written as

$$\mathcal{L} = -\partial_\mu \phi^* \partial^\mu \phi - V(|\phi|), \tag{1.1}$$

where ϕ is the complex scalar field and $V(|\phi|)$ is the scalar potential. The equation of motion for the scalar field can be found by varying (1.1) with respect to ϕ or ϕ^* to yield

$$\partial_\mu \partial^\mu \phi - \frac{\partial}{\partial \phi^*} V(|\phi|) = 0. \tag{1.2}$$

It is straightforward to see that (1.1) and (1.2) remain invariant under transformations which affect the global phase, $\phi \to e^{-i\alpha}\phi$. By Noether's theorem, this continuous symmetry corresponds to a conserved current,

$$j^\nu = -i(\phi^* \partial^\nu \phi - \phi \partial^\nu \phi^*), \tag{1.3}$$

from which we can define a conserved Noether charge, $Q = \int d^3x\, j^0$. Likewise, there exists a conserved energy, $E = \int d^3x\, T_{00}$, which can be derived from the energy-momentum tensor of the theory,

$$T_{\mu\nu} = \partial_\mu\phi\partial_\nu\phi^* + \partial_\nu\phi\partial_\mu\phi^* - g_{\mu\nu}(\partial_\alpha\phi\partial^\alpha\phi^* + V(|\phi|)). \tag{1.4}$$

To find non-topological solitons in the theory, one can make a time-harmonic ansatz for the scalar field,

$$\phi(t, \vec{x}) = f(r)e^{i\omega t}, \tag{1.5}$$

where ω is a real constant and $f(r)$ is a spherically-symmetric function in terms of the radial coordinate r. With this ansatz, the scalar field oscillates in the complex plane at a frequency ω and the restrictions of Derrick's theorem (which only apply to completely static configurations) can be avoided. By inserting (1.5) into the equation of motion (1.2), one can arrive at an ordinary differential equation for $f(r)$:

$$f''(r) + \frac{D-1}{r}f'(r) + \omega^2 f(r) - \frac{1}{2}\frac{d}{df}V(f) = 0, \tag{1.6}$$

where D denotes the number of spatial dimensions. Localized solutions to (1.6) can be found by imposing the asymptotic boundary condition $\lim_{r\to\infty} f(r) = 0$. Additionally, it is required that $f'(0) = 0$ so that the solution remains regular near and at the origin. When these conditions are applied, it becomes possible to obtain Q-balls for a variety of choices of the scalar potential $V(|\phi|)$. In some cases, the solutions can be found analytically [19–22], but in the general case one must resort to numerical techniques (such as the shooting method [23]) in order to determine the Q-ball profile. A representative example of a Q-ball solution is plotted in Figure 1.1.

The study of Q-balls can be traced back to the early work of Rosen [24] who investigated the possibility of classical particle-like solutions in non-linear scalar field theories. Shortly thereafter, Friedberg *et al.* [25] introduced the concept of non-topological solitons which are stabilized due to the symmetries of the underlying equations (see also [26]). However, the identification of Q-balls as a specific class of solitonic object would not be made until 1985 when Coleman established the basic conditions for their existence in three spatial dimensions [27, 28]. Using a step function model for $f(r)$ in (1.5), Coleman computed several of their elementary properties (such as their total charge and energy) and described the requisite features of the scalar potential $V(|\phi|)$. In the same paper, Coleman also introduced a convenient mechanical analogy between the Q-ball solutions of (1.6) and the classical trajectory of a point particle in an effective potential subject to friction. Following this work, research interest in Q-balls began to intensify as their relevance to particle physics and cosmology was quickly realized. In particular, it was shown that Q-balls are a generic

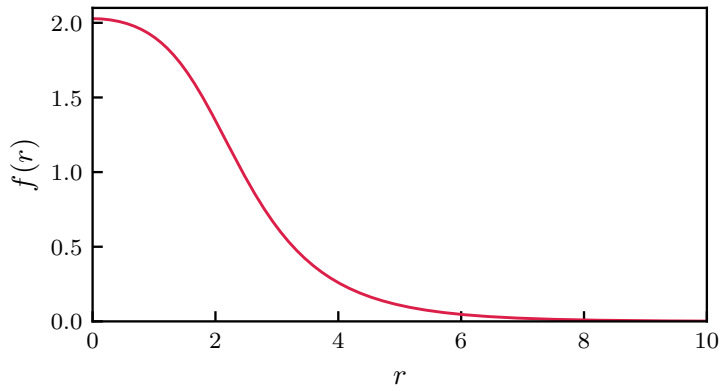

Figure 1.1: Representative example of a Q-ball solution. Plotted is the scalar field profile $f(r)$ found by solving (1.6) with boundary conditions set by $f'(0) = 0$ and $\lim_{r\to\infty} f(r) = 0$. In this case, we select $D = 3$ and use a numerical shooting technique. The scalar field potential is chosen to take the form (1.7) with $m = k = 1$ and $h = 0.2$. The characteristic oscillation frequency for this solution is $\omega = 0.75$.

prediction of supersymmetric extensions of the Standard Model and may have been created in early-Universe processes which invoke supersymmetry [29]. This means that Q-balls could be relevant for baryogenesis [30, 31], cosmological phase transitions [32, 33], and the dark matter problem [34, 35]. In parallel to these developments, several gravitating counterparts to Q-balls (such as boson stars and oscillatons [36]) were also identified.

Over the years, many distinct varieties of Q-balls have been studied in the literature. Perhaps the simplest variations of the basic theory involve different possibilities for the scalar field potential $V(|\phi|)$ in (1.1). The most general potential admitting Q-ball solutions is usually considered to be a sixth-order polynomial,

$$V_6(|\phi|) = m^2|\phi|^2 - \frac{k}{2}|\phi|^4 + \frac{h}{3}|\phi|^6, \tag{1.7}$$

where m, k, and h are real constants [22, 37]. While the $|\phi|^6$ term renders this potential non-renormalizable from the perspective of quantum field theory, the contemporary viewpoint is that such a potential could arise from an effective field theory description involving additional heavy scalars [37]. Another possibility for the scalar potential is the one admitting logarithmic non-linearities,

$$V_{\log}(|\phi|) = -\mu^2|\phi|^2 \ln(\beta^2|\phi|^2), \tag{1.8}$$

where μ and β are real constants [38, 39]. Potentials of this type may correspond to flat directions in the field space of supersymmetric models [40, 41]. Other possibilities include the piecewise parabolic potential [19, 20] and the "V-shaped" potential given by $V(|\phi|) =$

$\lambda|\phi|$ [42]. In each case, the unique functional form of $V(|\phi|)$ can lead to distinct properties of the corresponding Q-ball solutions. One can also consider more exotic modifications to the basic framework such as spinning Q-balls [43–46], charge-swapping Q-balls [47–49], and non-spherical configurations such as Q-tubes [50–52].

As stated previously, interest in Q-balls has largely been motivated by their potential relevance to cosmology and astroparticle physics. In particular, it has been proposed that Q-balls could have been created through several possible mechanisms such as the fragmentation of a scalar field condensate [30, 31] or through a process reminiscent of nucleosynthesis [33, 53]. If these primordial Q-balls can survive until present day, they may be detectable through terrestrial experiments. One possible experimental setup involves a global network of atomic magnetometers which are sensitive to the interactions between the Q-ball field and the intrinsic spins of elementary particles [54, 55]. In this scenario, a transient Q-ball passing through the Earth would induce spin-dependent energy shifts in the probe particles of the magnetometer. Another possible mechanism involves the detection of various particles such as neutrinos [56] or pions [57, 58] when a Q-ball passes through the Earth. It has also been proposed that current or next-generation gravitational wave experiments could observe the background signatures of Q-ball production [59, 60], interactions [61], or decay [62, 63]. Other potential detection mechanisms include atomic clocks [64, 65], opto-mechanical sensing arrays [66], and gravitational microlensing surveys [67].

Despite these efforts, experimental evidence for cosmological Q-balls remains elusive. However, their non-relativistic analogues have been observed in laboratory experiments involving condensates of superfluid ^{3}He [68–70]. This provides an example of a physical system in which the properties of Q-balls can be studied experimentally.

Regardless of their physical applications, Q-balls also hold significant theoretical and mathematical interest. Their very existence may be surprising from the perspective of linear wave theory where the dispersion relation is expected to govern the long-term dynamics of ordinary wave equations. It is a remarkable consequence of non-linearity that Q-balls can remain stable against this natural tendency; more surprising still is the range of non-linear scalar field theories which admit these solutions. At the same time, the equations governing Q-ball dynamics are relatively simple in comparison to many other types of bound structures. This has made them a useful mathematical prototype for more complicated physical objects such as black holes [71, 72]. Another fascinating aspect of Q-balls (and solitons in general) relates to their behaviour during interactions and collisions. Unlike Newtonian point particles, Q-balls are extended objects without definitive sizes or positions. Instead, the fields themselves are the fundamental dynamical entities and the notions of force and momentum become difficult to precisely define. Since there is no inherent restriction on the number of Q-balls in a field configuration of total charge Q, the creation and destruction

of Q-balls is also unfettered during interactions and collisions. Ultimately, the interplay of these factors can lead to a variety of remarkable time-dependent phenomena.

To conclude this section, let us review the salient features of Q-ball interactions which have been reported in previous studies. To our knowledge, the earliest numerical experiments involving Q-ball-type solitons were performed by Makhankov *et al.* [73] in two spatial dimensions. Investigating head-on collisions at relativistic velocities, they were among the first to identify the existence of distinct scattering regimes depending on the incident velocity. In particular, it was reported that Q-ball interactions become increasingly elastic as the collision velocity approaches the speed of light. On the other hand, collisions at lower incident velocities were found to be primarily inelastic and could result in bound-state formation or the dissipation of the solitons after the collision. In the same paper, they also identified the Q-ball oscillation frequency ω as a relevant parameter in determining the approximate velocity threshold for the onset of quasielasticity. These early results were extended by various authors who considered more complicated Q-ball models and collision scenarios [74–78]. Perhaps the most comprehensive study of this type has been performed by Battye and Sutcliffe [77] who explored Q-ball collisions in one, two, and three spatial dimensions. Focusing on the sixth-order polynomial potential (1.7), the authors reaffirmed the velocity-dependent behaviour observed in previous studies and explored Q-ball/anti-Q-ball scattering processes along with collisions between Q-balls with differing phase. For the Q-ball/anti-Q-ball case, the partial or total annihilation of the Noether charge was found to be a generic outcome for a large range of initial conditions. The authors also identified a novel dynamical process called "charge transfer" for collisions involving a relative phase difference wherein one Q-ball would transfer a portion of its field content to the other. Later studies would refine this understanding of Q-ball behaviour using analytical arguments [79] or more advanced numerical techniques [80]. In aggregate, these investigations have illustrated that collisions between Q-balls are complicated dynamical processes exhibiting a broad range of outcomes.

1.2 Overview of Gauged Q-balls

One of the simplest ways to extend the basic Q-ball model is to promote the global $U(1)$ symmetry of the theory to a local $U(1)$ symmetry. In this case, the Lagrangian density can be written as

$$\mathcal{L} = -\left(D_\mu \phi\right)^* D^\mu \phi - V\left(|\phi|\right) - \frac{1}{4} F_{\mu\nu} F^{\mu\nu}, \tag{1.9}$$

where ϕ is the complex scalar field, A_μ is the $U(1)$ gauge field, $F_{\mu\nu} = \partial_\mu A_\nu - \partial_\nu A_\mu$ is the electromagnetic field tensor, $D_\mu = \nabla_\mu - ieA_\mu$ represents the gauge covariant derivative with coupling constant e, and $V(|\phi|)$ is the scalar potential. Mathematically, the introduction of

the $U(1)$ gauge field in this manner represents a coupling of the theory to electromagnetism [81]. The equations of motion take the form

$$D_\mu D^\mu \phi - \frac{\partial}{\partial \phi^*} V(|\phi|) = 0, \tag{1.10}$$

$$\nabla_\mu F^{\mu\nu} + e j^\nu = 0, \tag{1.11}$$

where j^ν can be identified as the Noether current density,

$$j^\nu = -i(\phi^* D^\nu \phi - \phi (D^\nu \phi)^*). \tag{1.12}$$

The local $U(1)$ symmetry of the theory implies that (1.9)–(1.11) remain invariant under spacetime-dependent phase transformations and gauge transformations,

$$\phi \to e^{-ie\alpha(x)} \phi, \tag{1.13}$$

$$A_\mu \to A_\mu - \partial_\mu \alpha(x). \tag{1.14}$$

This symmetry corresponds to a conserved Noether charge, $Q = \int d^3x \; j^0$, from which we can define the total electric charge, $Q_e = eQ$. A conserved energy, $E = \int d^3x \; T_{00}$, can also be derived from the energy-momentum tensor,

$$\begin{aligned} T_{\mu\nu} = & F_{\mu\alpha} F_{\nu\beta} g^{\beta\alpha} - \frac{1}{4} g_{\mu\nu} F_{\alpha\beta} F^{\alpha\beta} \\ & + D_\mu \phi (D_\nu \phi)^* + D_\nu \phi (D_\mu \phi)^* \\ & - g_{\mu\nu} (D_\alpha \phi (D^\alpha \phi)^* + V(|\phi|)). \end{aligned} \tag{1.15}$$

To obtain non-topological solitons in the theory, one can adapt the basic Q-ball ansatz of (1.5) in the following way:

$$\phi(t, \vec{x}) = f(r) e^{i\omega t}, \tag{1.16}$$

$$A_0(t, \vec{x}) = A_0(r), \tag{1.17}$$

$$A_i(t, \vec{x}) = 0. \tag{1.18}$$

Here, $A_0(t, \vec{x})$ represents the time-component of the gauge field while $A_i(t, \vec{x})$ represents its spatial components. We assume that the spatial dimensionality of the system is $D = 3$ to maintain consistency with the standard formulation of Maxwell electrodynamics. When this ansatz is inserted into (1.10)–(1.11), one can derive a system of coupled ordinary differential

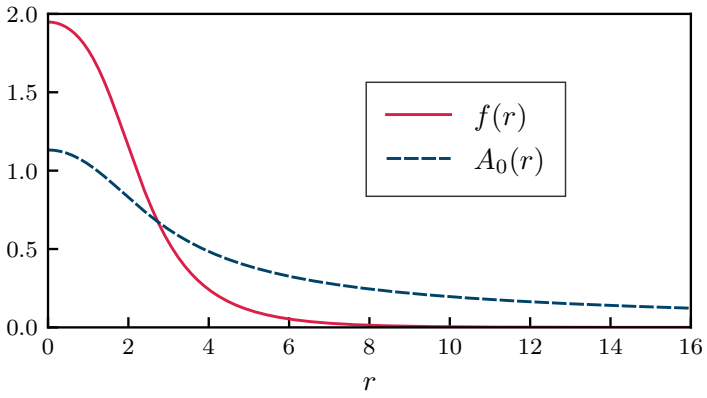

Figure 1.2: Representative example of a gauged Q-ball solution. Plotted is the scalar field profile $f(r)$ and the gauge field profile $A_0(r)$ found by solving (1.19)–(1.22). In this case, we select $e = 0.1$ and use a numerical shooting technique. The scalar field potential is chosen to take the form (1.7) with $m = k = 1$ and $h = 0.2$. The characteristic oscillation frequency for this solution is found to be $\omega \approx 0.863$.

equations for the spherical functions $f(r)$ and $A_0(r)$,

$$f''(r) + \frac{2}{r}f'(r) + f(r)(\omega - eA_0(r))^2 - \frac{1}{2}\frac{d}{df}V(f) = 0, \tag{1.19}$$

$$A_0''(r) + \frac{2}{r}A_0'(r) + 2ef(r)^2(\omega - eA_0(r)) = 0. \tag{1.20}$$

These equations must be supplemented by appropriate boundary conditions in order to ensure regularity of the fields and finiteness of energy:

$$\lim_{r\to\infty} f(r) = 0, \qquad \frac{df}{dr}(0) = 0, \tag{1.21}$$

$$\lim_{r\to\infty} A_0(r) = 0, \qquad \frac{dA_0}{dr}(0) = 0. \tag{1.22}$$

Together, the differential system (1.19)–(1.22) is akin to an eigenvalue problem for ω which can be solved numerically. The non-topological solitons which arise from these equations are known as *gauged Q-balls.* A representative example of a gauged Q-ball solution is plotted in Figure 1.2.

As with ordinary (i.e., non-gauged) Q-balls, the study of gauged Q-balls began with the work of Rosen [82] who sought to construct a Lorentz-invariant classical model for a charged elementary particle which was singularity-free and which had a positive-definite energy density. In this foundational work, the basic conditions for gauged Q-ball existence were established and an approximate solution of the form (1.16)–(1.18) was derived. In [83], the same problem was examined using a Hamiltonian formalism. The properties of gauged

Q-balls were further studied in [84, 85] and precise numerical solutions to the differential system (1.19)–(1.22) were obtained for the first time. These papers also identified some distinct features of gauged Q-balls in comparison to non-gauged Q-balls. For example, it was shown in [84] that the electric charge of a gauged Q-ball results in a Coulomb repulsion which can place an upper limit on their size. However, the same effect can also lead to qualitatively new types of non-topological solitons in the model such as gauged Q-shells [86–88]. In another impactful work [89], it was shown that the properties of gauged Q-balls can be derived through an analytic correspondence with non-gauged Q-balls. This can greatly simplify the required analysis for many problems of interest [90–92]. We also point out [93–96] as significant contributions to the literature over the years.

Although gauged Q-balls have been studied for some time now, it remains a challenging issue to understand their stability[2]. If gauged Q-balls are not dynamically robust against generic perturbations, they may cease to represent a physically-viable object because any interaction of the gauged Q-ball (e.g., with the external environment) could quickly cause it to fall apart. This would severely limit their relevance for many scenarios of interest. Despite the importance of this question, a definitive answer has so far remained elusive. In [95], it was shown that a well-known criterion which predicts the stability of non-gauged Q-balls, $(\omega/Q)\, dQ/d\omega < 0$, cannot be applied to gauged Q-balls in the general case. In the same paper, it was further demonstrated through numerical simulations that one can find examples of gauged Q-balls which remain stable with respect to spherically-symmetric perturbations. However, the authors also speculated that these solutions might become unstable if more general types of perturbations were introduced into the system. In [99], the same problem was analyzed in a related model by computing the stress and shear relations which arise from the energy-momentum tensor of the theory. Inspired by similar calculations for non-gauged Q-balls [100, 101], it was shown that internal forces may destabilize some gauged Q-balls even when the von Laue stability condition (which states that the radial pressure distribution must contain at least one node [102, 103]) is satisfied. One can also recall [104, 105] where stable gauged Q-balls were argued to exist provided that the gauge coupling is small.

Assuming they are not generically unstable, the study of gauged Q-balls can be motivated by both physical and theoretical considerations. Regarding the physical aspect, gauged Q-balls have recently been proposed as a type of soliton dark matter which might have been formed through hypothetical early-Universe mechanisms such as Affleck-Dine

[2]We are referring here to the notion of "classical stability" (i.e., stability of the solutions with respect to small perturbations of the fields). This lies in contrast to "quantum-mechanical stability" [97, 98] which concerns the decay of the Q-balls via quantum processes such as collective tunnelling. In this thesis, we make no consideration of any quantum aspects of the problem and treat gauged Q-balls as entirely classical objects.

baryogenesis [106–108] or a cosmological first-order phase transition [109]. Similar to non-gauged Q-balls, these processes may result in a relic abundance which could be detectable through terrestrial experiments (though the net electric charge of these objects would necessarily alter the means of detection [110]). However, aside from these few papers, the historical motivations for studying gauged Q-balls have largely been theoretical. As stated above, Rosen's initial investigations were driven by the desire for a consistent classical description of a charged elementary particle. This desire arises from several well-known problems related to point charges in classical electromagnetism such as their infinite total energy [111]. From this perspective, gauged Q-balls represent a satisfying example of an extended particle-like object which emerges quite naturally from the dynamical equations of electromagnetism coupled to a scalar field. At the same time, gauged Q-balls are also interesting in a mathematical sense due to their solitonic nature. It is somewhat surprising that one can find an electrically-charged soliton which is not stabilized by topological effects. One might naively expect that such a field configuration would be nonviable due to the repulsive nature of the Coulomb force, yet this is apparently not the case. Moreover, gauged Q-balls exist as a straightforward extension of the non-gauged Q-ball theory. As remarked in [84], "many of the theories that we know of (or at least believe in) involve gauge or local symmetries" and so it is reasonable to ask how the basic Q-ball model might be generalized along these lines. With this context in mind, we adopt the viewpoint in this thesis that gauged Q-balls are fascinating classical objects that are worthy of study in their own right.

Lastly, we comment that our study of gauged Q-balls is also motivated by a general interest in soliton dynamics. Unlike their non-gauged counterparts, the collisions and interactions of gauged Q-balls have not been investigated in the literature to any significant extent (at least to our knowledge). However, it might be expected that electromagnetic effects could substantially alter the collision picture due to the presence of the $U(1)$ gauge field. Addressing this question is a major focus of this thesis.

1.3 Numerical Methodology

In this section, we provide a brief overview of the numerical techniques which are employed throughout this thesis. For a more detailed discussion, we refer the reader to several comprehensive works on the subject [23, 112–115]. We also describe the software libraries used and the computational resources required for typical calculations in our study.

1.3.1 Finite-Difference Approximations

When solving coupled systems of non-linear partial differential equations, it is often impossible to find exact analytical solutions. In many cases, one must turn to numerical methods in order to render the calculations tractable. While there are several approaches to doing so, we shall focus on the technique of *finite-difference approximations* wherein the derivative operators are replaced by algebraic expressions which can be solved on a computer.

To illustrate the method, let us begin by describing a system of differential equations using abstract notation [114],

$$Lu = f, \tag{1.23}$$

where L denotes a differential operator, u denotes a smooth function representing the solution to the equation, and f is a source term[3]. We assume that the differential system (1.23) is defined on some continuous domain and is supplemented with appropriate boundary conditions. In order to obtain a representation of the system on a discrete grid, we proceed by dividing the domain among N uniformly-spaced points with spacing h. We can then define the finite-difference approximation of (1.23) as

$$L^h u^h = f^h, \tag{1.24}$$

where L^h, u^h and f^h are the discrete versions of L, u, and f. In solving (1.24), it is expected that the discrete solution u^h should yield the continuum solution u in the limit $h \to 0$.

As a simple example of this procedure, we use the one-dimensional advection equation,

$$\partial_t \psi(t,x) = \partial_x \psi(t,x). \tag{1.25}$$

In the abstract notation of (1.23), we can identify $L = \partial_t - \partial_x$ with $u = \psi(t,x)$ and $f = 0$. Typically, the solution to (1.25) will be desired within some spatial domain (e.g., $\{x : x_{\min} \leq x \leq x_{\max}\}$) for which we can define a discrete spacing $h_x = (x_{\max} - x_{\min})/(N_x - 1)$. An illustration of the basic grid structure is given in Figure 1.3. At this stage, the spatial part of the differential operator L^h can be constructed from the Taylor expansion of $\psi(t,x)$ about the points $x = x_0 \pm h_x$. Ignoring the time dependence for notational convenience, these expansions take the following form:

$$\psi(x_0 + h_x) = \psi(x_0) + h_x \psi'(x_0) + \frac{h_x^2}{2}\psi''(x_0) + O(h_x^3), \tag{1.26}$$

$$\psi(x_0 - h_x) = \psi(x_0) - h_x \psi'(x_0) + \frac{h_x^2}{2}\psi''(x_0) + O(h_x^3), \tag{1.27}$$

[3]The discussion in this section will be framed in the context of linear differential systems in 1+1 dimensions. The generalization to non-linear systems or higher spacetime dimensions is straightforward.

where the primes indicate differentiation with respect to x. Through algebraic manipulation of these expansions, one can derive several possible representations of $\psi'(x_0)$:

$$\psi'(x_0) = \frac{\psi(x_0 + h_x) - \psi(x_0)}{h_x} + O(h_x), \tag{1.28}$$

$$\psi'(x_0) = \frac{\psi(x_0) - \psi(x_0 - h_x)}{h_x} + O(h_x), \tag{1.29}$$

$$\psi'(x_0) = \frac{\psi(x_0 + h_x) - \psi(x_0 - h_x)}{2h_x} + O(h_x^2). \tag{1.30}$$

When the time dependence is trivially reinserted, the above equations represent the "forward", "backward", and "centered" discrete approximations, respectively, to the spatial derivative of $\psi(t, x)$. An analogous procedure can be followed to find the temporal derivatives of $\psi(t, x)$. Together, these can be used to construct a finite-difference approximation to the advection equation (1.25):

$$\begin{aligned}\frac{\psi(t_0 + h_t, x_0) - \psi(t_0, x_0)}{h_t} = \frac{1}{2}\Bigg[&\frac{\psi(t_0 + h_t, x_0 + h_x) - \psi(t_0 + h_t, x_0 - h_x)}{2h_x} \\ &+ \frac{\psi(t_0, x_0 + h_x) - \psi(t_0, x_0 - h_x)}{2h_x}\Bigg] + O(h_t^2, h_x^2).\end{aligned} \tag{1.31}$$

Here we have applied a specific discretization scheme which is known as the Crank-Nicolson method [116]. With this method, the spatial derivative in (1.25) is effectively averaged over the $t = t_0$ and $t = t_0 + h_t$ time steps so that the discretization remains centered around a "fictitious" grid point at $t = t_0 + h_t/2$ (see Figure 1.4). It can be shown through Taylor expansion about this point that this scheme is accurate up to terms which are $O(h_t^2, h_x^2)$. In (1.31), the quantity to be determined is the function value at the advanced time, $\psi(t_0 + h_t, x_0)$. Since this depends on the adjacent function values at $t = t_0 + h_t$, it is an implicit method which requires a system of algebraic equations to be solved at every time step (for example, via matrix algorithms or repeated point-wise Newton iteration). Provided that suitable initial data and boundary conditions are used, this procedure can be repeated indefinitely to advance the solution forward in time and obtain a numerical approximation to $\psi(t, x)$.

Having illustrated the basic idea behind finite-difference approximations, it is necessary to comment on some practical aspects which have been overlooked. In particular, we highlight that (1.31) is just one of many possible discrete representations of the advection equation (1.25). Depending on the desired properties of the approximation, one could construct an infinite number of alternative finite-difference schemes which serve the same purpose. However, there is no guarantee that a given scheme will be numerically "stable"

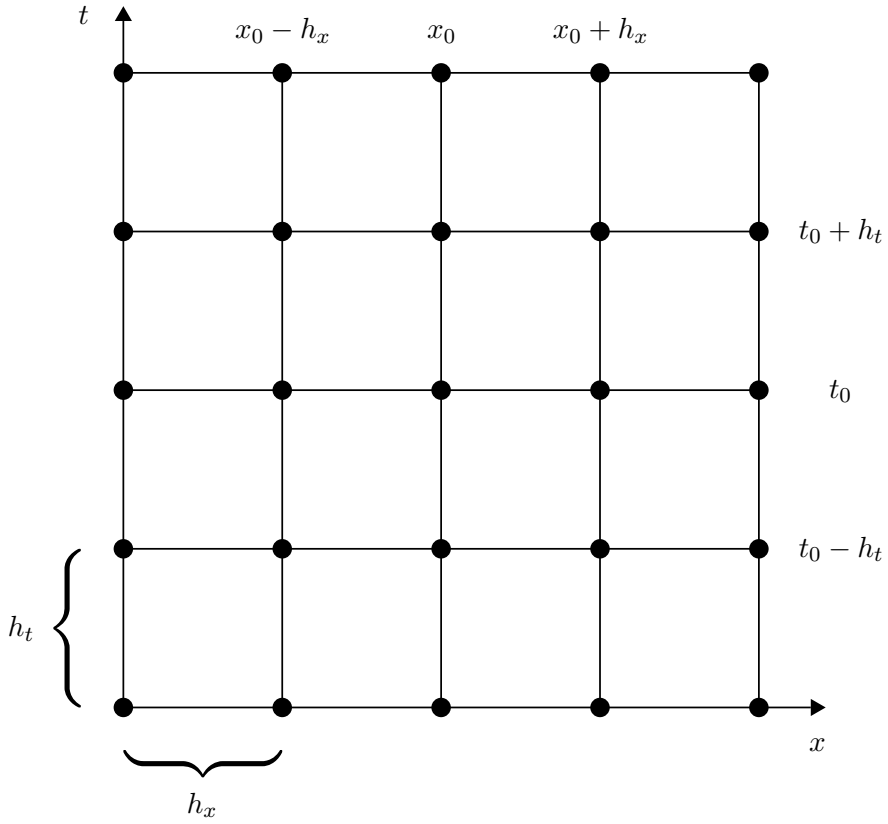

Figure 1.3: Illustration of a finite-difference grid in 1+1 dimensions. The grid is uniform with discrete spacings of h_t and h_x between adjacent points. The line of points corresponding to $x = x_0$ and $x = x_0 \pm h_x$ in the expansions (1.26)–(1.27) are shown at the top of the figure; the corresponding line of points for the temporal dimension are shown to the right.

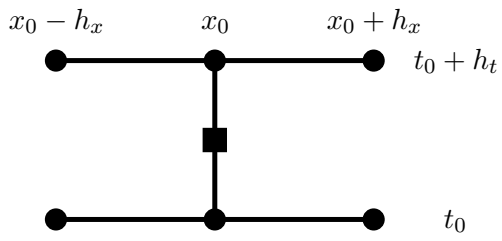

Figure 1.4: Stencil of points used for the Crank-Nicolson finite-difference scheme in (1.31). The locations of $x = x_0$, $x = x_0 \pm h_x$ and $t = t_0$, $t = t_0 + h_t$ are represented using black circles. In this case, the scheme is centered around a "fictitious" grid point at $t = t_0 + h_t/2$ which is marked by a black square.

in the sense that the numerical solution remains bounded for all time (assuming, of course, that the continuum solution is also bounded). In general, this notion of stability can only be established through detailed numerical analysis or empirical testing. However, it can be shown that the Crank-Nicolson method used in (1.31) will remain numerically stable for any choice of h_t and h_x. This makes it a favourable approach for solving many classes of parabolic and hyperbolic partial differential equations; we apply it in Chapter 2 and Chapter 3 of this thesis.

Another technique which we use to solve time-dependent equations is the classic Runge-Kutta method [23]. To illustrate the method, consider a generic differential equation which is first-order in time,

$$\partial_t y(t) = F(t, y). \tag{1.32}$$

Starting from the initial condition $y(t_0) = y_0$, the function value at the advanced time $t = t_0 + h_t$ can be computed using the following iterative procedure:

$$k_1 = F(t_0, y_0), \tag{1.33}$$

$$k_2 = F(t_0 + h_t/2, y_0 + k_1/2), \tag{1.34}$$

$$k_3 = F(t_0 + h_t/2, y_0 + k_2/2), \tag{1.35}$$

$$k_4 = F(t_0 + h_t, y_0 + k_3), \tag{1.36}$$

$$y(t_0 + h_t) = y(t_0) + \frac{h_t}{6}(k_1 + 2k_2 + 2k_3 + k_4). \tag{1.37}$$

This provides a fourth-order approximation of $y(t_0 + h_t)$. Since higher-order differential systems can generally be recast as a set of coupled first-order equations, the above procedure can be applied quite generally. For example, it may be used to solve the advection equation (1.25) with $y(t) = \psi(t, x)$ and $F(t, \psi) = \partial_x \psi(t, x)$ when the spatial derivative is replaced with an appropriate finite-difference operator. We apply the classic Runge-Kutta method in Chapter 4 of this thesis.

1.3.2 Adaptive Mesh Refinement

In the preceding discussion of finite-difference approximations, we have assumed that the underlying solution to the differential system can be well-represented on a uniform grid with spacing h. However, it is often advantageous to adapt the value of h within the computational domain in order to capture features of the solution which may vary on disparate time and length scales. The technique we employ to achieve this functionality is known as *adaptive mesh refinement* (AMR).

The AMR algorithm is based upon a hierarchy of uniform finite-difference grids which differ in the grid spacing h. Typically, the user specifies a base value for h and the number

of additional higher-resolution grids which are desired in the hierarchy. The grid spacing on the l^{th} grid is then related to the spacing on the $(l+1)^{\text{th}}$ grid by the integer ratio $\sigma_l = h_l/h_{l+1} \geq 2$. It is assumed that the grid with spacing h_{l+1} is fully contained within and aligned upon the grid with spacing h_l; this means that grids which are at adjacent levels of the hierarchy will share a number of common grid points. With this setup, it is also possible for multiple non-overlapping grids to exist at the same level of the hierarchy (each covering a different region of the computational domain). A schematic representation of an AMR grid hierarchy is given in Figure 1.5.

The key feature of the AMR algorithm is its ability to dynamically reconstruct the grid hierarchy depending on the emerging behaviour of the numerical solution. If the solution is found to require greater resolution in some region of the domain, the grid structure can be adjusted to increase the effective resolution in this region while simultaneously decreasing the effective resolution where such precision isn't needed. The location of these high- and low-precision regions is determined by computing the approximate error in the numerical solution at regular intervals (see [117] for details of this procedure). After determining the location of these regions and adjusting the grid structure accordingly, the solution is evolved on each grid for a short time and then propagated downward through the hierarchy at common grid points. By repeating these basic steps, one can significantly improve the accuracy of the finite-difference implementation.

In this thesis, we use an AMR algorithm due to Pretorius and Choptuik [118] which is adapted from the work of Berger and Oliger [112]. The use of AMR turns out to be crucial for our calculations involving gauged Q-ball dynamics in axisymmetry and 3D.

1.3.3 The Multigrid Method

A second algorithm which we rely on to accelerate finite-difference calculations is known as *multigrid*. This method is well-suited for solving time-independent (elliptic) partial differential equations of the type which arise in Chapter 3 and Chapter 4 of this thesis. To begin the discussion, let us return to the abstract notation of (1.24) and define the *residual* of a finite-difference scheme as

$$r^h = L^h \tilde{u}^h - f^h. \tag{1.38}$$

Here, $\tilde{u}^h$ represents our current approximation (or "best guess") to the true solution of the discrete problem, u^h. If the finite-difference equations were to be satisfied exactly, then the residual would vanish everywhere in the computational domain. Unfortunately, this is difficult to achieve in practice and one must usually settle for the case where r^h is driven to some small value. With this goal in mind, there are several possible approaches; perhaps the most commonly-used are the "relaxation" techniques which strive to reduce

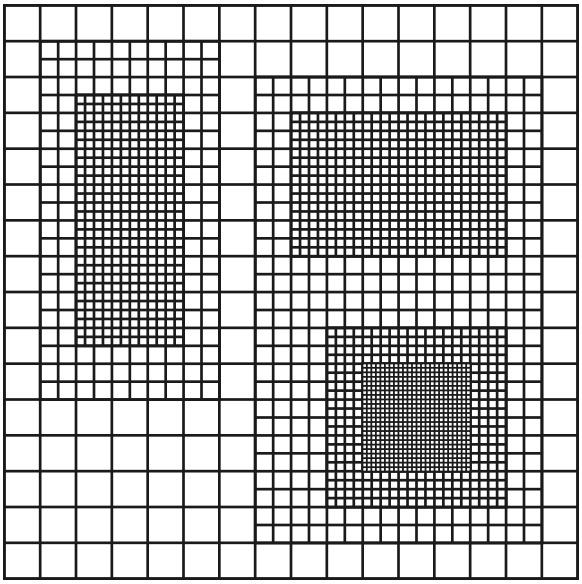

Figure 1.5: Representation of a grid hierarchy with adaptive mesh refinement (AMR). In this example, there are four levels of uniform finite-difference grids which differ in the grid spacing by factors of two. The AMR algorithm can adapt the number of higher-resolution grids in the hierarchy (along with their sizes and locations) depending on the emerging features of the solution.

r^h through repeated corrections to the grid function values. Examples of basic relaxation methods are the Jacobi, Gauss-Seidel, and successive over-relaxation (SOR) algorithms [23]. However, a central issue with these methods is their slow rate of convergence when the residual contains significant "low-frequency" components (from the viewpoint of Fourier analysis and in comparison to the grid spacing h) [114]. On the other hand, these relaxation methods are typically very good at quickly reducing the "high-frequency" components of the residual. Herein lies the main advantage of multigrid: by defining a hierarchy of grids with differing resolutions, one can efficiently eliminate the low-frequency components on the coarser grids of the hierarchy (where they effectively become high-frequency components with respect to the coarse grid spacing) and then propagate the relevant corrections up to the finer grids where the full problem can be solved.

To illustrate the method further, we define the *solution error* of a finite-difference scheme as

$$e^h = u^h - \tilde{u}^h. \tag{1.39}$$

Through algebraic substitution of (1.39) into (1.24), one can obtain

$$L^h(e^h + \tilde{u}^h) = f^h. \tag{1.40}$$

From the residual definition (1.38) and assuming the linearity of L^h, this becomes

$$L^h e^h = -r^h. \tag{1.41}$$

One can treat this as a new finite-difference equation to be solved for the unknown e^h using standard techniques (such as repeated relaxation sweeps). Once e^h is computed, an improved approximate solution $\tilde{u}^h$ can be obtained via $\tilde{u}^h \leftarrow \tilde{u}^h + e^h$ which follows from (1.39). The residual r^h can then be updated from (1.38). By itself, this sequence does not offer much improvement over a direct attempt to solve (1.24) because we have done nothing to deal with the problematic low-frequency components of r^h and e^h. However, the key idea of multigrid is to transfer the updated residual onto a coarser grid in the hierarchy which has a grid spacing $H = 2h$. On the coarser grid, the problematic low-frequency components of the solution are effectively transformed into higher-frequency components which can be more easily smoothed via relaxation. The problem on the coarser grid,

$$L^H e^H = -r^H, \tag{1.42}$$

can be treated in an analogous way and the corresponding residual can be transferred further along the multigrid hierarchy. Eventually, the residual computed on the coarsest grid can be propagated back onto the grid with spacing h where (1.41) can again be solved. This completes one "cycle" of the multigrid algorithm. Through repeated application of this procedure, one can achieve significant speedups in the solution of elliptic problems due to the increased efficiency of relaxation on the coarsest grids.

In this thesis, we use a full-approximation storage (FAS) multigrid algorithm as implemented by Pretorius [117]. This is necessary for the enforcement of physical constraints on the initial data in Chapter 3 and Chapter 4.

1.3.4 Error Analysis

When solving differential equations numerically, it is useful to have some mechanism for establishing the validity of the solutions. In the ideal case, one would prefer to compute the solution error directly from (1.39). However, the true solution is not known for most problems of dynamical interest and one must instead resort to indirect tests of the implementation. For this purpose, we apply two techniques which are known as *convergence testing* and *independent residual evaluation* [114].

The idea of convergence testing is based upon an ansatz due to Richardson [119] which states that the discrete solution due to a finite-difference approximation should admit an

expansion around the continuum solution in powers of the grid spacing:

$$u^h(t,x) = u(t,x) + hE_1(t,x) + h^2E_2(t,x) + h^3E_3(x,t) + \dots \tag{1.43}$$

Here, $E_1(t,x)$, $E_2(t,x)$, $E_3(t,x)$, ... are continuum error functions which do not depend on h. We have also assumed for simplicity that the problem is defined on a uniform grid in one time and one space dimension and uses a first-order-accurate finite-difference scheme. While the forms of the error functions are generally not known, it is clear from (1.43) that $u^h(t,x) \to u(t,x)$ as $h \to 0$. This implies that if the finite-difference calculations are repeated with decreasing values of h, one should observe the discrete solution "converging" to the continuum one. To make this explicit, we define the *convergence factor* of the finite-difference implementation as

$$Q_c(t) = \frac{\|u^{4h} - u^{2h}\|}{\|u^{2h} - u^h\|}, \tag{1.44}$$

where u^n denotes the discrete solution corresponding to the grid spacing n and $\|\cdot\|$ denotes the L_2-norm of point-wise differences of the argument. In this case, we use a definition of the L_2-norm which is normalized by the total number of points N in the corresponding grid,

$$\|v^n\| = \left(\frac{\sum_{i=1}^{N} |v_i^n|^2}{N} \right)^{1/2}, \tag{1.45}$$

so that the magnitude of $\|v^n\|$ is roughly independent of the specific grid resolution. By evaluating the expansion (1.43) for the different grid spacings listed in (1.44), it can be shown that $Q_c(t) = 2$ for a first-order-accurate finite-difference scheme in the ideal case. The strategy is then to compute the numerical solution at grid spacings of h, $2h$, and $4h$ and plot $Q_c(t)$ to assess the trends in convergence. If $Q_c(t)$ approaches a value of 2^n, and if the trend improves as $h \to 0$, one can reasonably conclude that the numerical implementation is converging at a rate which is $O(h^n)$.

While convergence testing can establish that the numerical solution is approaching a continuum limit, it does not guarantee that this continuum limit will be the expected one. By this we mean that convergence testing cannot protect against the class of errors which produce a convergent numerical solution to an erroneous differential system (for example, if a programming mistake has altered the finite-difference equations in some way). To mitigate this risk, one can try to back-substitute the numerical solution found using the original finite-difference scheme into a wholly independent discretization of the equations of motion. Let us define $\bar{L}^h$ as the *independent residual operator* which is constructed by discretizing the continuum operator L in a way that is distinct from L^h. We will further

assume that $\bar{L}^h$ admits an expansion in powers of the grid spacing,

$$\bar{L}^h = L + h\bar{L}_1 + h^2\bar{L}_2 + h^3\bar{L}_3 + \ldots, \tag{1.46}$$

where the differential operators $\bar{L}_1$, $\bar{L}_2$, $\bar{L}_3$, ... may involve higher-order derivatives than L. To proceed, one can evaluate the discrete equation (1.24) using $\bar{L}^h$ in place of L^h:

$$\begin{aligned} \bar{L}^h u^h - f^h &= (L + h\bar{L}_1 + \ldots)(u(t,x) + hE_1(t,x) + \ldots) - f^h \\ &= Lu(t,x) - f(t,x) + h(LE_1(t,x) + \bar{L}_1 u(t,x)) + O(h^2). \end{aligned} \tag{1.47}$$

In the above, we have utilized the Richardson ansatz (1.43) and also replaced f^h with its continuum representation. The terms $Lu(t,x)$ and $f(t,x)$ on the right-hand side of (1.47) will exactly cancel while the remaining terms will vanish as $h \to 0$ at the corresponding order in h (first-order in this example). This means that the independent residual is expected to converge to zero if u^h correctly represents a discrete solution to the differential system. On the other hand, if an error has been made in the implementation, the ansatz (1.43) will necessarily contain some $O(1)$ component which prevents $u^h \to u$ as $h \to 0$. It can then be shown that the independent residual (1.47) will also tend to a finite quantity. This provides a straightforward mechanism to check that the discrete numerical solution is converging to the expected continuum one.

1.3.5 Software and Performance

To apply the numerical techniques discussed above, we utilize a number of pre-existing software libraries. These libraries are designed to handle many of the technical details associated with adaptive finite-difference calculations such as memory management, data input/output, and parallelism.

For implementing the discrete equations of motion which arise in Chapter 2 and Chapter 3, we use Rapid Numerical Prototyping Language (RNPL) [120]. Within this framework, the user provides a high-level description of the finite-difference equations using an operator-based syntax and the RNPL compiler automatically generates Fortran or C code which solves the system. For implementing the discrete equations of motion which arise in Chapter 4, we use the Finite Difference Toolkit (FD) [121] built upon Maple [122]. Similar to RNPL, the FD package provides a high-level mechanism to generate Fortran and C code which solves the system of discrete equations. For implementing the adaptive mesh refinement and multigrid algorithms, we use the PAMR/AMRD libraries [117, 118]. These libraries provide an interface through which the user can specify custom functions (such as solution update routines and residual calculations) without concerning themselves with low-level programming issues related to managing grid hierarchies in parallel. Aside from the

software listed here, we have also written a number of supplementary programs to support the objectives of our study.

When discussing numerical simulations, it is useful to provide some sense of the scale of the required computing resources. For this purpose, let us define the "cost" of a given calculation as the approximate amount of time required for its execution on a single processing unit. While a full complexity analysis is beyond the scope of this work, we comment that the cost of grid-based numerical methods scales with both the number of grid points and the dimensionality of the problem. The use of adaptive mesh refinement significantly improves performance by reducing the total number of grid points required to achieve the desired accuracy. Additional speedup is achieved by parallelizing the calculations across 32 to 256 CPUs. For our analysis of gauged Q-ball dynamics in axisymmetry (Chapter 2 and Chapter 3), we find that a typical simulation requires $O(1$ week$)$ of CPU time. For our analysis of gauged Q-ball dynamics in three spatial dimensions (Chapter 4), we find that a typical simulation requires $O(1$ month$)$ of CPU time. This difference in CPU time arises primarily from the reduced dimensionality of the problem under the assumptions of axisymmetry. Overall, the simulations described in this thesis required approximately 130 years of collective CPU time. These simulations were performed on the Graham and Cedar clusters of the Digital Research Alliance of Canada.

1.4 Outline of the Thesis

This thesis is concerned with the dynamical behaviour of gauged Q-balls. As stated previously, there are several open questions in the literature related to the stability and interactions of these objects. The remainder of this work is devoted to addressing these questions using the numerical techniques discussed in Section 1.3.

In Chapter 2, we study gauged Q-ball stability in axisymmetry. We begin our analysis by mapping the space of gauged Q-ball configurations in the polynomial (1.7) and logarithmic (1.8) scalar field models. We then evolve some of these configurations forward in time to assess their stability and determine the fate of any unstable configurations. In both models studied, we find evidence for configurations which can remain stable with respect to general axisymmetric perturbations. We also find that some configurations are unstable and can be destroyed in various ways (for example, by fragmentation or dispersal of the fields). For the case of small gauge coupling, we further observe that some unstable modes appear to be non-spherical and we map the approximate regions of stability and instability in the solution space. The content of Chapter 2 has previously been published in [1]; hereafter, any references to [1] can also be assumed to refer to the content of Chapter 2.

In Chapter 3, we study the dynamics of gauged Q-balls during relativistic head-on collisions in axisymmetry. We test the effects of various collision parameters such as the initial

velocity, relative charge, relative phase, and gauge coupling strength on the outcome of the collision. When the gauge coupling is small, our results are found to be in broad agreement with previous work on the collisions of non-gauged Q-balls. When the gauge coupling is large, we find that electromagnetic effects can significantly alter the collision picture (for example, by accelerating the Q-balls prior to impact and by reducing the elasticity of the collisions at large velocities). We also find that collisions between gauged Q-balls can result in the creation of an electromagnetic radiation pulse. The content of Chapter 3 has previously been published in [2]; hereafter, any references to [2] can also be assumed to refer to the content of Chapter 3.

In Chapter 4, we revisit the analyses of Chapter 2 and Chapter 3 using fully three-dimensional numerical simulations. The principal new result from this study is the observation of gauged Q-ball configurations which can remain stable with respect to generic three-dimensional perturbations. This addresses an open question in the literature as to whether gauged Q-balls can be classically stable when symmetry assumptions are relaxed. We also investigate gauged Q-ball collisions in three spatial dimensions, finding the dynamics to be dependent on the impact parameter (among other quantities). The content of Chapter 4 has previously been published in [3]; hereafter, any references to [3] can also be assumed to refer to the content of Chapter 4.

In Chapter 5, we provide some concluding remarks and comment on future directions of research. The appendices provide supplementary material for Chapter 2, Chapter 3, and Chapter 4; this material has previously appeared in [1–3].

Throughout this work, we adopt units where $c = \hbar = 1$ and employ the metric signature $(-,+,+,+)$. We use index notation for tensor quantities with summation implied over the repeated indices:

$$v_\mu v^\mu = \sum_{\mu=0}^{D} v_\mu v^\mu, \tag{1.48}$$

where D is the number of spatial dimensions. Throughout this thesis, we will interchangeably use the terms "Q-ball" and "gauged Q-ball" when the distinction between the gauged and non-gauged solutions is obvious by context. This is done for brevity.

Chapter 2

Dynamical Evolution of $U(1)$ Gauged Q-balls in Axisymmetry

2.1 Introduction

Solitons are a fundamental prediction of many physical theories[1]. They are characterized as stable, localized solutions to non-linear field equations that behave in many ways like particles. Broadly speaking, solitons can be classified as either topological or non-topological. Topological solitons owe their existence and stability to the specific topological constraints of a given model. Non-topological solitons, in contrast, can arise simply due to the balance of attractive and repulsive self-interactions in the theory. In addition, the stability of non-topological solitons is often associated with the presence of conserved charges which emerge from the theory's underlying symmetries (though one can also construct solitonic configurations in the absence of such charges [123]).

Perhaps the simplest example of a non-topological soliton in field theory is the Q-ball: a stable, localized solution of a complex scalar field theory with a non-linear attractive potential and a global or gauge $U(1)$ symmetry. In recent years, Q-balls have attracted significant attention due to their prevalence in supersymmetric theories [29] and their possible cosmological consequences. In particular, it has been suggested that Q-balls may be relevant for baryogenesis [30, 31], cosmological phase transitions [32, 33], and the dark matter problem [34, 35]. The formation of Q-balls could also lead to detectable gravitational wave signatures [124]. However, regardless of their physical applications, Q-balls are also interesting from a theoretical perspective as stable, particle-like objects that can be constructed from smooth classical fields and that have vanishing topological charge.

The properties of Q-balls under a global $U(1)$ symmetry have been studied extensively

[1]The content of this chapter has previously been published in [1].

in the literature. Starting with the work of Rosen [24], Q-ball solutions have been found in a variety of physically-motivated models using various scalar field potentials (see [125] for a recent review). For some special potentials, the equations can be solved exactly [19–21, 38], but in the general case one must use approximations or numerical methods in order to determine the characteristic features of Q-balls. Associated with each solution in a given model, there is a conserved energy E and a conserved Noether charge Q (from which the Q-ball gets its name) corresponding to the particle number. Each solution is also characterized by an internal oscillation frequency ω which can be interpreted as the chemical potential of the configuration [22]. In addition to ordinary (ground state) Q-balls, one can construct excited Q-balls which have additional radial nodes or non-zero angular momentum [25, 43, 101, 126, 127]. The basic theory has also been extended by coupling Q-balls to gravity [128–130], by introducing a massless or massive gauge field [82, 84, 90], and by considering non-spherical configurations such as Q-tubes [50], Q-rings [131], and composite systems of Q-balls [47].

When the global $U(1)$ symmetry of the theory is gauged, the Q-balls acquire an electric charge and are known as *gauged Q-balls* [84]. Gauged Q-balls have properties that can differ significantly when contrasted to their global (non-gauged) counterparts. The presence of a massless gauge field introduces a long-range repulsive force that can destabilize the solutions for large gauge couplings. This repulsive force can give rise to novel scalar field configurations such as Q-shells [86–88], but it can also place limits on the maximum size and charge of gauged Q-balls for some scalar field potentials [87, 94]. The existence of this maximal charge corresponds with the limits of the allowed range of the frequency ω, and in general the gauged Q-ball configurations cannot be uniquely characterized by the value of ω [94]. Despite these differences, there exists a correspondence which allows for the properties of gauged Q-balls to be approximated from the properties of non-gauged (global) Q-balls, which are often much simpler [89]. In addition, when the interaction between the scalar field and gauge field is weak, gauged Q-balls are expected to closely resemble their non-gauged counterparts [93].

One of the essential properties of Q-balls relates to their dynamical stability. In order to be physically viable, solitons must be robust against perturbations. However, the problem of establishing the stability of solitons is often complicated by the non-linear nature of the governing field equations. In some cases, linear perturbation analyses and stability theorems can be applied to determine the expected regions of stability and instability.

For non-gauged Q-balls, it has been shown that the simple relation

$$\frac{\omega}{Q}\frac{dQ}{d\omega} < 0 \tag{2.1}$$

serves as an effective criterion for establishing regions of stability [25, 132]. However, the case of gauged Q-balls is more complicated due to the presence of the repulsive gauge field. It was recently shown in Ref. [95] that the sign of $dQ/d\omega$ cannot be used to assess the stability of gauged Q-balls in the general case. In the absence of such a criterion, one can still analyze the stability of these solutions using (among other alternatives) a numerical approach: dynamically evolving perturbed configurations through direct solution of the non-linear equations of motion. This method was applied in Ref. [95] to show that gauged Q-balls in several models can be stable with respect to spherical perturbations. However, it remains an open question as to whether gauged Q-balls can be classically stable against decay from more general perturbations beyond spherical symmetry. In addition, the instability mode for non-gauged Q-balls is always spherical [133], but it is not known whether gauged Q-ball decay can be mediated by non-spherical modes.

In this paper, we make progress toward understanding some aspects of gauged Q-ball dynamics by performing fully non-linear numerical simulations of the field equations in axisymmetry. There are two main questions we shall explore: (i) what is the range of stability of gauged Q-balls in axisymmetry? And (ii), what is the final fate of those configurations which are unstable? To answer these questions, we construct spherical gauged Q-ball initial data using a numerical shooting technique. We then assess the stability of these configurations by dynamically perturbing the system and observing the subsequent behaviour.

Numerical results presented below suggest that there exist both stable and unstable branches of solutions in axisymmetry. We find that stable gauged Q-balls, when perturbed, can survive over timescales which are long compared to the dynamical time with no evidence of measurable growing modes which destroy the configuration. These solutions respond to perturbation by oscillating continuously or weakly radiating before returning to the initial configuration. Unstable gauged Q-balls, in contrast, are typically short-lived and can decay in one of several ways. Some unstable solutions break apart into many smaller gauged Q-balls or shed scalar field until they relax into a smaller stable configuration. Other unstable solutions fragment into non-spherical ring-like structures which propagate away from the axis of symmetry and can survive for some time. In addition, for the case of a logarithmic potential we observe that the maximum magnitude of the scalar field can grow without bound. We interpret this behaviour as a consequence of the potential being unbounded from below. Finally, we test the effect of the gauge coupling strength on the stability, finding that gauged Q-balls closely resemble their non-gauged counterparts when the coupling is small.

This paper is organized as follows: in Section 2.2, we present the equations of motion of the theory. In Section 2.3, we discuss the procedure for obtaining axisymmetric initial

data which is used in the numerical evolutions. In Section 2.4, we briefly discuss the types of perturbations that are applied to the system. In Section 2.5, we present the results for several representative evolutions. We conclude with some final remarks in Section 2.6.

Throughout this work, we use natural units where $c = \hbar = 1$ and employ the metric signature $(-,+,+,+)$. We focus on unexcited gauged Q-ball solutions (those for which the scalar field modulus attains only one maximum). For brevity, we will use the term "Q-ball" interchangeably with "gauged Q-ball" when the distinction between the gauged and non-gauged solutions is obvious by context.

2.2 Equations of Motion

The Lagrangian density of the theory takes the form

$$\mathcal{L} = -\left(D_\mu\phi\right)^* D^\mu\phi - V\left(|\phi|\right) - \frac{1}{4}F_{\mu\nu}F^{\mu\nu}, \tag{2.2}$$

where ϕ is the complex scalar field, $F_{\mu\nu} = \partial_\mu A_\nu - \partial_\nu A_\mu$ is the electromagnetic field tensor for the $U(1)$ gauge field A_μ, and $D_\mu = \nabla_\mu - ieA_\mu$ denotes the gauge covariant derivative with coupling constant e. Here, $V(|\phi|)$ is a $U(1)$-invariant scalar field potential that permits Q-ball solutions in the limit $e \to 0$. In this work, we consider the following scalar field potentials:

$$V_{\log}(|\phi|) = -\mu^2|\phi|^2\ln(\beta^2|\phi|^2), \tag{2.3}$$

$$V_6(|\phi|) = m^2|\phi|^2 - \frac{k}{2}|\phi|^4 + \frac{h}{3}|\phi|^6, \tag{2.4}$$

where μ, β, m, k, and h are assumed to be positive, real-valued parameters of the potentials. The potential (2.3) has previously been studied in various forms in Refs. [38, 39, 87, 93, 95, 111, 133] while potential (2.4) has been studied in Refs. [22, 43, 84, 89, 96, 99, 126, 127]. Further details about the scalar potentials (2.3) and (2.4) will be discussed in the sections that follow.

The evolution equations for the theory can be found by varying the Lagrangian density (2.2) with respect to the scalar and gauge fields to obtain

$$D_\mu D^\mu\phi - \frac{\partial}{\partial\phi^*}V(|\phi|) = 0, \tag{2.5}$$

$$-\nabla_\mu F^{\mu\nu} - ie\phi(D^\nu\phi)^* + (ie\phi^*)D^\nu\phi = 0. \tag{2.6}$$

From (2.6) we identify the conserved Noether current

$$j^\mu = -i(\phi^* D^\mu\phi - \phi(D^\mu\phi)^*) \tag{2.7}$$

which corresponds with invariance of the theory under the $U(1)$ transformations

$$\phi \to e^{-ie\alpha(x)}\phi, \tag{2.8}$$

$$A_\mu \to A_\mu - \partial_\mu \alpha(x). \tag{2.9}$$

The conserved current (2.7) can be integrated to obtain a conserved Noether charge $Q = \int j^0 \, d^3x$. Also associated with the theory is the energy-momentum tensor

$$\begin{aligned} T_{\mu\nu} =& F_{\mu\alpha}F_{\nu\beta}g^{\beta\alpha} - \frac{1}{4}g_{\mu\nu}F_{\alpha\beta}F^{\alpha\beta} \\ &+ D_\mu\phi(D_\nu\phi)^* + D_\nu\phi(D_\mu\phi)^* \\ &- g_{\mu\nu}(D_\alpha\phi(D^\alpha\phi)^* + V(|\phi|)) \end{aligned} \tag{2.10}$$

and the corresponding conserved energy $E = \int T_{00} \, d^3x$.

To solve the field equations of motion, we adopt the usual cylindrical coordinates (t, ρ, φ, z) and write the spacetime line element as

$$ds^2 = -dt^2 + d\rho^2 + \rho^2 d\varphi^2 + dz^2. \tag{2.11}$$

In three spatial dimensions, computational constraints would limit the range of possible field configurations that could be explored. We therefore reduce the computational complexity of the problem by imposing axisymmetry on the system: no dependence of any of the fields on the azimuthal angle φ is assumed. This results in a system of six coupled non-linear partial differential equations which are described in Appendix A.1.

Evolution of the fields is subject to the constraints

$$\nabla \cdot \vec{E} = \rho_c \, , \tag{2.12}$$

$$\nabla \cdot \vec{B} = 0 \, , \tag{2.13}$$

where $\vec{E}$ and $\vec{B}$ are the electric and magnetic fields, respectively, and ρ_c is the electric charge density

$$\rho_c = ie(\phi^*\partial_t\phi - \phi\partial_t\phi^*) + 2e^2A_0\phi\phi^*. \tag{2.14}$$

Equation (2.13) will be trivially satisfied in axisymmetry while equation (2.12) can be re-expressed in terms of the gauge field components using the relation

$$E_i = F_{i0} = \partial_i A_0 - \partial_0 A_i. \tag{2.15}$$

We also impose the Lorenz gauge condition

$$\nabla_\mu A^\mu = 0 \tag{2.16}$$

to simultaneously fix the gauge and simplify the equations. It is expected that a numerical solution to the equations of motion will also satisfy the constraint equations at a given time.

2.3 Initial Data

To generate suitable initial data, we make a spherically-symmetric ansatz for the scalar and gauge fields

$$\phi(t, \vec{x}) = f(r)e^{i\omega t}, \tag{2.17}$$

$$A_0(t, \vec{x}) = A_0(r), \tag{2.18}$$

$$A_i(t, \vec{x}) = 0. \tag{2.19}$$

Inserting this ansatz into the equations of motion yields the following system of coupled equations:

$$f''(r) + \frac{2}{r}f'(r) + f(r)g(r)^2 - \frac{1}{2}\frac{d}{df}V(f) = 0, \tag{2.20}$$

$$A_0''(r) + \frac{2}{r}A_0'(r) + 2ef(r)^2 g(r) = 0. \tag{2.21}$$

Here, $V(f)$ is the scalar potential and $g(r) = \omega - eA_0(r)$. This system constitutes an eigenvalue problem for the parameter ω subject to the boundary conditions

$$\lim_{r\to\infty} f(r) = f'(0) = 0, \tag{2.22}$$

$$\lim_{r\to\infty} A_0(r) = A_0'(0) = 0, \tag{2.23}$$

which are required to ensure finiteness of energy and regularity at the origin.

Gauged Q-ball solutions can be found by solving the system of equations (2.20)–(2.21) using an iterative shooting technique [23] to simultaneously determine $f(r)$ and $A_0(r)$. In this method, an initial choice is made for the value of $g(0)$ and a corresponding guess is made for $f(0)$. The equations are then integrated on a uniform grid using a fourth-order classical Runge-Kutta method out to a finite radius r_0. Depending on the asymptotic behaviour of $g(r)$ and $f(r)$ at r_0, the value of $f(0)$ is adjusted through iterative bisection until the boundary conditions (2.22) and (2.23) are approximately satisfied at large r. Once a solution is found, the eigenvalue ω can be determined from the asymptotic value of $g(r)$ using the boundary condition (2.23) and $A_0(r)$ can be determined as $A_0(r) = (\omega - g(r))/e$.

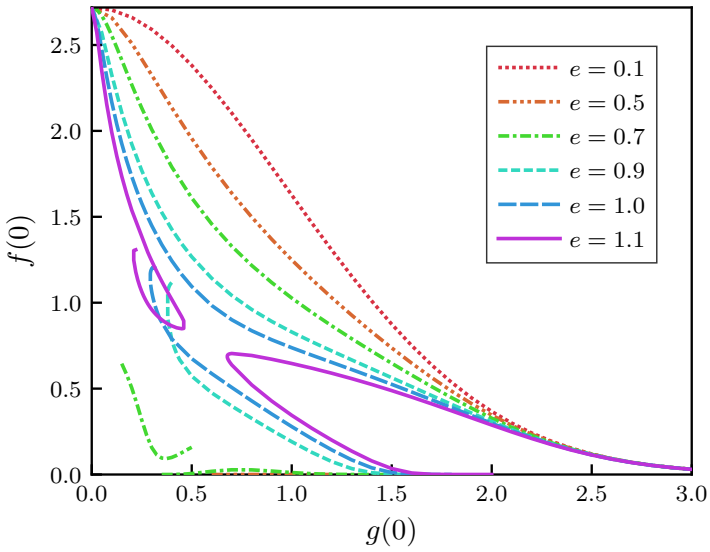

Figure 2.1: Shooting results for the logarithmic model (2.3) with $\mu = \beta = 1$. Plotted is the gauged Q-ball's central scalar field value $f(0)$ versus $g(0) = \omega - eA_0(0)$ for increasing values of e. Note that only unexcited gauged Q-ball solutions are presented here. The abrupt endpoints in the parameter space of curves with $e \geq 0.7$ correspond to the appearance of additional radial nodes in the solution.

One of the main computational challenges associated with this procedure is the high numerical accuracy required in order to find satisfactory solutions. Typically, the number of digits required for convergence will exceed the capacity of double-precision floating-point numbers. To overcome this limitation, we employ the arbitrary-precision arithmetic capabilities of Maple [122]. The software precision is adjusted and the integration is carried out until the asymptotic behaviour of $f(r)$ is observed to decay exponentially at large r. At this point, the value of $f(r)$ is typically very small (one part in 10^8 or smaller) and so the fields $g(r)$ and $f(r)$ approximately decouple in equations (2.20) and (2.21). In this asymptotic region, we fit a $1/r$ tail to $g(r)$ and an exponentially-decaying tail to $f(r)$ [94] so that the solution is determined to an arbitrarily large radius.

In Figure 2.1, we present the results of our shooting procedure for the logarithmic potential (2.3). For numerical purposes, we find it convenient to set $\mu = \beta = 1$ in the model. The central scalar field value $f(0)$ is plotted against $g(0) = \omega - eA_0(0)$ for various values of e. When the value of e is small (representing weak gauge coupling), the curve of solutions is monotonically decreasing and single-valued, closely resembling the behaviour of non-gauged Q-balls. However, when e is increased, the curves are no longer single-valued and they begin to bifurcate with some curves ending abruptly in the solution space. These distinct endpoints generally correspond to the appearance of additional radial nodes in the solution, representing excited gauged Q-balls [25, 43, 101, 126, 127]. Also notable is the

appearance of distinct curves close to the horizontal axis where $f(0)$ is very small. These solutions correspond to Q-shells [86–88] which attain their maximal field values away from $r = 0$ and resemble shell-like concentrations of the fields.

Plotted in Figure 2.2 are the results of our numerical shooting procedure for the polynomial potential (2.4) with $m = k = 1$ and $h = 0.2$. In order to clearly distinguish the curves, and following Ref. [96], we plot $g(0) = \omega - eA_0(0)$ versus ω for various values of e. We restrict our shooting to solutions where $\omega \leq 1$, which is required in order to ensure that the solutions have finite energy [84, 94, 96]. The case of $e = 0.0$ (corresponding to non-gauged Q-balls) is represented by a linear line in the solution space. As e is increased, a minimal value $\omega_{\rm min}$ appears which separates each curve into an upper and lower branch. The value of $\omega_{\rm min}$ increases with e until $\omega_{\rm min} > 1$, at which point no gauged Q-ball solutions can be found in the model. We note that while Q-shell solutions are known to exist for the polynomial potential [88], no such solutions are found for our choice of the potential parameters.

As a basic check of our shooting procedure, we have compared our numerical solutions to those reported in previous publications on $U(1)$ gauged Q-balls in logarithmic and polynomial models [95, 96]. We find good agreement with the previously reported results.

In order to generate initial data that is suitable for evolution in axisymmetry, we transform the spherical solutions in (2.17)–(2.19) to cylindrical coordinates by performing a fourth-order polynomial interpolation of the spherical solution in the ρ–z plane. This provides axisymmetric initial data that will subsequently be used in our numerical simulations.

2.4 Diagnostics

Here we discuss several diagnostics which are useful in characterizing the stability of each gauged Q-ball configuration. For the purposes of this work, a configuration is defined to be stable if small perturbations to the initial state remain bounded during the course of the evolution. Unstable configurations are those for which small perturbations grow exponentially on top of the solution, eventually leading to the destruction of the Q-ball (such as through fragmentation or dispersal of the fields). Note that with this definition, we classify as stable those configurations for which the fields may be weakly oscillating or radiating but are not destroyed by the initial perturbation.

There are several physical quantities associated with the scalar and gauge fields which are relevant when monitoring the evolution of each configuration. Principal among these are the conserved Noether charge Q and the total energy E. The Noether charge is given

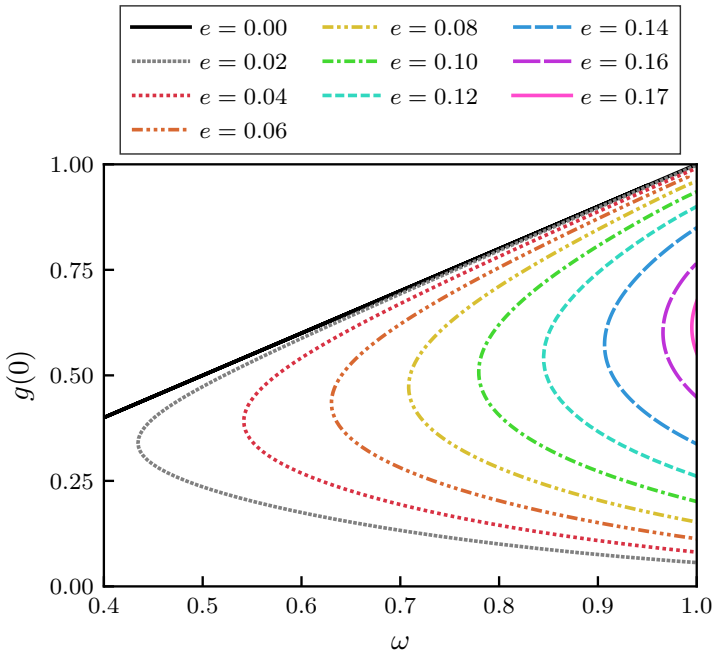

Figure 2.2: Shooting results for the polynomial model (2.4) with $m = k = 1$ and $h = 0.2$. Plotted is $g(0) = \omega - eA_0(0)$ versus the eigenfrequency ω for various values of e. A linear dependence can be observed for $e = 0.0$ (representing non-gauged Q-balls). For $e > 0$, the curve bifurcates into an upper and lower branch. As the value of e is increased, the range of the solutions decreases significantly.

by

$$Q = 2\pi i \iint d\rho\, dz\, \rho \left[\phi (D^0\phi)^* - \phi^* (D^0\phi)\right] \tag{2.24}$$

and the total energy is given by

$$\begin{aligned} E = 2\pi \iint d\rho\, dz\, \rho \Big[& F_{0\alpha} F_0{}^{\alpha} + \frac{1}{4} F_{\alpha\beta} F^{\alpha\beta} + V(|\phi|) \\ & + (D_\alpha \phi)(D^\alpha \phi)^* + 2(D_0\phi)(D_0\phi)^* \Big]. \end{aligned} \tag{2.25}$$

Both Q and E are time-independent quantities which are expected to be conserved as long as the fields remain localized within the simulation domain.

We will now discuss how we add small perturbations to the stationary initial data. The solutions are perturbed in two ways: (i) perturbation through the inherent numerical truncation error of the finite-difference scheme, and (ii) perturbation by an auxiliary scalar field designed to explicitly excite all underlying modes of the configuration.

2.4.1 Perturbation by Numerical Truncation Error

As a first test of the stability of our gauged Q-ball configurations, we numerically evolve the fields forward in time using the axisymmetric initial data described in Section 2.3. Upon evolution, the fields will be subject to small numerical perturbations due to the finite-difference discretization which is used to solve the evolution equations. This can be understood from the observation that the discrete solution of a uniform centered finite-difference scheme admits a truncation error expansion around the continuum solution in powers of the grid spacing [119]. While the exact form of this expansion is generally not known (making the perturbations effectively random), the magnitude of the associated truncation error is tied closely to the numerical resolution of the simulation and can therefore be indirectly controlled. In the sections that follow, we will refer to perturbations of this form as "Type 0".

One consequence of this type of perturbation is that any potential instabilities will take longer to manifest for higher-resolution simulations than for lower resolution ones. This is because the magnitude of the truncation error becomes smaller at higher resolutions. It is therefore necessary to evolve the configuration over sufficiently long times in order to assess stability. The notion of a "sufficiently long time" is difficult to make precise, but this timescale can generally be estimated by observing the oscillations of the scalar field modulus $|\phi|$ when subject to a perturbation. Even for small perturbations, the maximum value of $|\phi|$ will tend to oscillate at frequencies which correspond to the underlying modes of the configuration. The dynamical time can then be identified as the inverse frequency of the longest mode. For the problem at hand, we evolve each configuration with this timescale in mind so that any slowly-growing unstable modes have the opportunity to manifest. We find that this procedure provides an adequate preliminary test of stability which can be further verified using additional perturbation methods (to be discussed immediately below).

2.4.2 Perturbation by an Auxiliary Scalar Field

As a second test of stability, we dynamically perturb the gauged Q-balls by simulating the implosion of an asymmetric shell of matter onto the stationary configurations. We do this by introducing a massless real scalar field $\chi(t, \rho, z)$ that couples to the complex Q-ball field $\phi(t, \rho, z)$ in the modified theory:

$$\begin{aligned} \mathcal{L} = &- \left(D_\mu \phi\right)^* D^\mu \phi - V\left(|\phi|\right) - \frac{1}{4} F_{\mu\nu} F^{\mu\nu} \\ &- \partial_\mu \chi \partial^\mu \chi - U(|\phi|, \chi), \end{aligned} \tag{2.26}$$

where $U(|\phi|,\chi)$ describes the interaction potential of the fields ϕ and χ. We compute the modified equations of motion from (2.26) to obtain

$$-\nabla_\mu F^{\mu\nu} - ie\phi(D^\nu\phi)^* + (ie\phi^*)D^\nu\phi = 0, \tag{2.27}$$

$$D_\mu D^\mu\phi - \frac{\partial}{\partial\phi^*}V(|\phi|) - \frac{\partial}{\partial\phi^*}U(|\phi|,\chi) = 0, \tag{2.28}$$

$$\nabla_\mu\nabla^\mu\chi - \frac{1}{2}\frac{\partial}{\partial\chi}U(|\phi|,\chi) = 0. \tag{2.29}$$

One can see from (2.27)–(2.29) that by choosing an interaction potential $U(|\phi|,\chi)$ such that $U(|\phi|,\chi)\to 0$ in the limit of $\chi\to 0$, then the modified equations (2.27) and (2.28) reduce to equations (2.5) and (2.6) (with (2.29) just representing an independent wave equation for χ). This means that χ and ϕ will elicit some mutual influence when the fields overlap, but the influence will disappear if the fields become well-separated. In this sense, χ can act as an external perturbing agent. We initialize χ as an ingoing asymmetric shell of the form

$$\chi(0,\rho,z) = A\exp\left[-\left(\frac{\sqrt{\frac{(\rho-\rho_0)^2}{a^2}+\frac{(z-z_0)^2}{b^2}}-r_0}{\delta}\right)^2\right], \tag{2.30}$$

$$\partial_t\chi(0,\rho,z) = \frac{\chi+\rho\partial_\rho\chi+z\partial_z\chi}{\sqrt{\rho^2+z^2}}, \tag{2.31}$$

where A, a, b, δ, r_0, ρ_0 and z_0 are parameters specifying the characteristics of the initial pulse. If r_0 is made large, the field approximately vanishes in the vicinity of the gauged Q-ball at the initial time and so χ can be considered an external perturbation with a size controlled by A. Strictly speaking, the notion of an "external" perturbation cannot be made precise because gauged Q-balls do not have a finite radius. However, since the scalar field decays exponentially away from the center of the configuration, initializing the auxiliary field sufficiently far away from the center will serve as a good approximation to an external perturbation. Note also that the auxiliary field couples only to the scalar field so that the long-range behaviour of the gauge field is not a significant factor.

During the evolution, the massless scalar field implodes toward the origin and collides with the gauged Q-ball. The two fields temporarily interact before the massless field passes through the origin and explodes outward to $r\to\infty$, leaving the gauged Q-ball perturbed at the origin. Due to the asymmetry of the imploding pulse, the interaction of the two scalars is expected to excite the underlying modes of the system and induce the disruption of any unstable configurations. For our purposes, we choose

$$U(|\phi|,\chi) = c|\phi|^2\chi^2 \tag{2.32}$$

where c is a coupling constant that controls the coupling strength between χ and ϕ. In the sections that follow, we will refer to perturbations of this form as "Type I". This technique resembles the methods of Ref. [134] to investigate the stability of boson stars.

We note that configurations which are subject to perturbations of this type will inevitably also be perturbed by the inherent truncation error of the numerical simulation (Type 0). However, since Type 0 perturbations are typically very small and effectively random, Type I perturbations provide an additional level of control in determining the stability of a given configuration. For the results presented here, the simulations are repeated for various values of the Type I perturbation parameters A and c. This is done to verify that the response of the Q-ball field to the perturbation (as measured, for example, by the magnitude of the induced oscillations of the scalar field modulus $|\phi|$) remains in the linear regime: an increase of A or c leads to a corresponding increase in the magnitude of oscillations of the perturbed $|\phi|$.

2.5 Numerical Results

Here we present results from the dynamical evolution of gauged Q-balls in the potentials (2.3) and (2.4). For each simulation, we numerically solve the evolution equations using a second-order Crank-Nicolson finite-difference scheme implemented using the Rapid Numerical Prototyping Language (RNPL) framework [120]. Fourth-order Kreiss-Oliger dissipation is applied as a mild low-pass filter to damp poorly-resolved and potentially problematic (from a numerical stability viewpoint) high-frequency solution components. We implement a modified Berger-Oliger adaptive mesh refinement (AMR) algorithm via the PAMR/AMRD libraries [118] to increase the numerical resolution of our simulations. In all examples presented below, the base grid is taken to be 129×257 grid points in $\{\rho, z\}$ and up to five additional levels of mesh refinement are used with a refinement ratio of 2:1. The domain is taken to be finite with outgoing boundary conditions imposed at the outer boundaries. Reflective (or anti-reflective) boundary conditions are imposed at the axis of symmetry in order to ensure regularity of the fields. We choose a Courant factor of $\lambda = dt/\min\{d\rho, dz\} = 0.25$ and evolve the configurations until at least $t \approx 1000$ to assess stability, though in many cases we evolve for longer in order to observe the late-time dynamics. Further details about the numerical implementation and code validation are given in Appendix A.2.

To illustrate the general behaviour of stable and unstable configurations, we focus on several specific solutions for the potentials (2.3) and (2.4). These solutions are listed in Table 2.1. Configurations L1–L4 correspond to the logarithmic potential while configurations P1–P2 correspond to the polynomial potential. We note that besides L1–L4 and P1–P2, we have also performed hundreds of additional evolutions along the solution curves of Figure 2.1 and Figure 2.2 in order to determine the general regions of stability. This stability

Configuration	Result	$\phi(0,0)$	$A_0(0,0)$	e	ω	E	Q	d_{max}	Perturbation	c	A
L1	stable	0.6461	1.383	1.1	2.522	52.08	-22.37	50	Type I	0.1	0.1
L2	unstable	1.179	3.159	1.1	3.695	281.5	-94.34	50	Type 0	–	–
L3	unstable	2.448×10^{-13}	0.9803	1.1	3.078	260.3	-92.76	75	Type 0	–	–
L4	unstable	1.539	2.254	1.1	2.680	95.18	-38.13	50	Type 0	–	–
P1	stable	1.973	2.515	0.17	0.9976	405.1	-387.5	50	Type I	0.1	0.1
P2	unstable	1.904	46.94	0.02	0.9958	1.076×10^6	-1.480×10^6	150	Type 0	–	–

Table 2.1: Results for several representative gauged Q-ball evolutions. The configurations L1–L4 correspond to solutions found using the logarithmic potential (2.3). P1–P2 represent configurations found using the polynomial potential (2.4). The second column indicates the outcome of the numerical evolution. From left to right, the remaining columns give the initial central scalar field amplitude $\phi(0,0)$, the initial central gauge field value $A_0(0,0)$, the electromagnetic coupling constant e, the eigenfrequency ω, the total integrated energy E, the total Noether charge Q, the size of the simulation domain spanning $\{\rho : 0 \leq \rho \leq d_{max}\}$ and $\{z : -d_{max} \leq z \leq d_{max}\}$, the type of perturbation used, and the perturbation parameters c and A (if applicable).

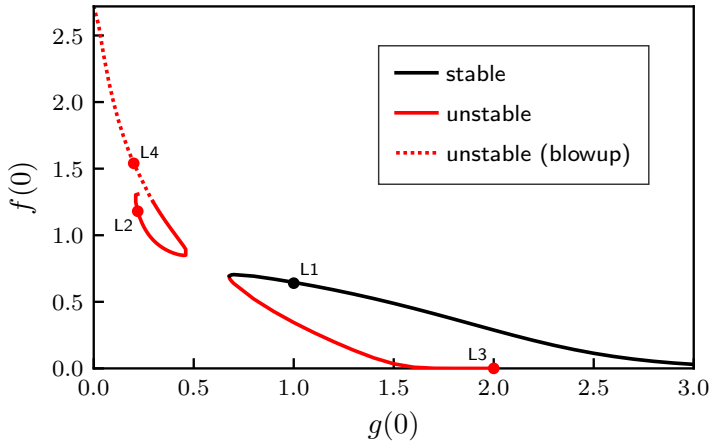

Figure 2.3: Regions of stability and instability for gauged Q-balls in the $V_{\log}$ model with $e = 1.1$. The points L1–L4 correspond with the configurations listed in Table 2.1. The solid black line represents stable configurations while red lines represent regions of instability. The dashed red line indicates regions where blowup of the solutions is observed; see the main text for details.

investigation will be discussed below.

2.5.1 $V_{\log}$ Model

Here we consider the dynamical stability of gauged Q-balls in the logarithmic model (2.3). Most relevant for this work are the results of Ref. [95] which conducted numerical evolutions of gauged Q-ball configurations for $e = 1.1$ in spherical symmetry. There it was found that both stable and unstable gauged Q-balls can exist in the model, though the classical stability criterion (2.1) provides little information about the stability of a given configuration in the general case. Once again, we set $\mu = \beta = 1$ for numerical purposes. For brevity, and to facilitate comparison with previous work, we focus on the case of $e = 1.1$ where the system is fully coupled.

The relevant properties of each of the configurations L1–L4 are described in Table 2.1 along with the final result of numerically evolving the configuration forward in time. In Figure 2.3, the location of each of these configurations in the solution space is labelled with a dot. L1 corresponds to a solution on the stable branch. L2 corresponds to an unstable configuration which decays through dissipation of the fields. L3 corresponds to an unstable Q-shell solution which breaks apart into several smaller solitonic components. Finally, L4 illustrates the case of an unstable solution which responds to perturbation by growing without bound. Here, only L1 is subject to the Type I perturbation (to illustrate the dynamical stability of the configuration) while L2–L4 are all subject to Type 0 perturbations only.

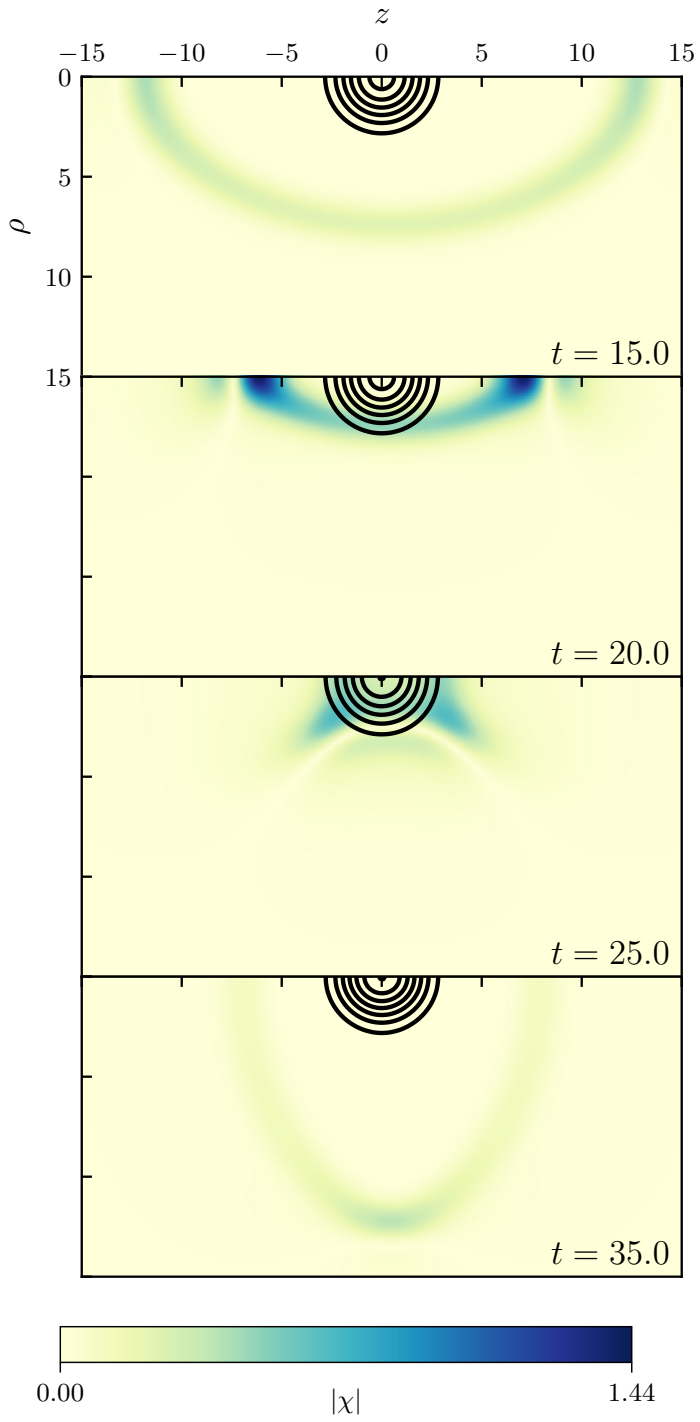

Figure 2.4: Magnitude $|\chi|$ of the perturbative scalar field interacting with a stationary gauged Q-ball (represented by contours) corresponding to configuration L1 in Table 2.1. The contour lines represent the Q-ball field modulus $|\phi|$ in steps of 0.1. The axis of symmetry is coincident with the top edge of each panel. The simulation domain spans $\{\rho : 0 \leq \rho \leq 50\}$ and $\{z : -50 \leq z \leq 50\}$.

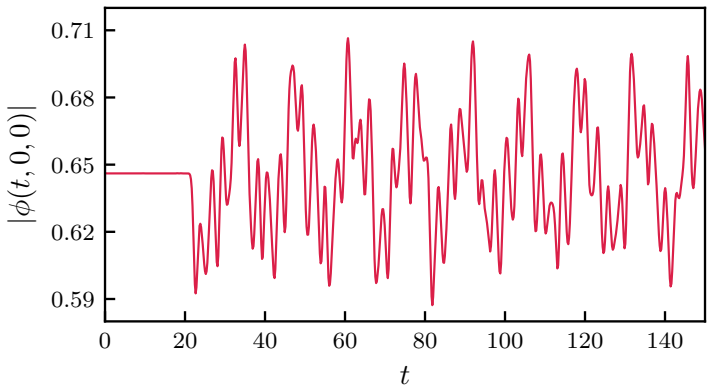

Figure 2.5: Oscillations of the scalar field modulus $|\phi|$ for configuration L1 subject to a Type I perturbation with parameters $c = 0.1$ and $A = 0.1$. Corresponding snapshots for the evolution are given in Figure 2.4. The perturbative field χ implodes upon the Q-ball at $t \approx 20$, causing large oscillations in $|\phi|$. Over the full timescale of the evolution, the Q-ball slowly returns toward the original configuration.

First let us discuss the evolution of configuration L1. This evolution is run for 65000 base-grid time steps up to a final time of $t = 6400$. To assess the stability, we apply a Type I perturbation with parameters $c = 0.1$ and $A = 0.1$. Results for this evolution are shown in Figure 2.4. The contour lines in the figure represent the scalar field modulus $|\phi|$ while the colormap represents the perturbing field modulus $|\chi|$. The imploding pulse, which is centered around the point $\{\rho = 0.0, z = 0.5\}$, interacts with the Q-ball starting at $t \approx 20$ (the second panel of the figure) and explodes through the origin, leaving the simulation domain at $t \approx 70$. This induces small asymmetric distortions in the Q-ball field which can be observed as changes of the contour lines in the subsequent panels. This distortion also creates large oscillations in the maximal value of $|\phi|$ which are plotted in Figure 2.5. Prior to the imploding pulse interacting with the Q-ball, the oscillations of $|\phi|$ are very small and are sourced by Type 0 perturbations. After the pulse interacts with the Q-ball at $t \approx 20$, the amplitude of the oscillations grows significantly as the imploding pulse transfers energy to the configuration. It oscillates continuously around the stationary (unperturbed) solution before slowly returning toward the original configuration.

If configuration L1 was unstable, one would expect that the interaction between ϕ and χ would excite any unstable modes underlying the solution. Once excited, these modes should quickly grow and bring about the destruction of the configuration. However, no such behaviour is observed in our numerical experiments using different values of c and A. In addition, we have also analyzed the behaviour of the configuration when subject to Type 0 perturbations only, finding no evidence of instability. We therefore conclude that L1 is stable.

Next we consider L2, which lies on the upper branch of the solution curve in Figure 2.3. We subject this configuration only to a Type 0 perturbation. The time evolution of L2 is depicted in Figure 2.6. The scalar field modulus retains its initial shape for only a short time before quickly decaying and spreading radially. As the evolution proceeds, the fields continue to propagate toward the boundaries until no significant remnant of the initial configuration remains in the domain. As mentioned previously, the timescale over which the Q-ball survives before dissipating can be extended by increasing the numerical resolution of the simulation (thereby decreasing the size of the perturbation). However, even with five additional levels of refinement, the solution begins to decay within the first few oscillations of the scalar field. Since the outcome of this evolution is the total dispersal of the fields, we classify L2 as unstable.

Consider next L3, which lies on the lower branch of Figure 2.3, near the bottom axis. Notably, $f(0) \approx 0$ near this axis which results in $|\phi|$ attaining its maximal value away from the origin. This configuration resembles a shell-like distribution of matter and is therefore labelled a "gauged Q-shell". The evolution of this configuration subject to a Type 0 perturbation is shown in Figure 2.7. At the initial time (top panel), the shell-like nature of the solution is readily apparent. As time evolves, the spherical symmetry of the configuration is quickly broken as the Q-shell fragments into several individual components which propagate away in different directions. Two of these components remain centered on the axis of symmetry and travel along this axis toward the outer boundaries. These components remain approximately spherical for the entirety of the evolution (aside from oscillations and distortions induced by the fragmentation process) and represent smaller "child" gauged Q-balls of the initial configuration. In addition, we observe that the field also fragments into several distinct components which coalesce away from the axis of symmetry. In three-dimensions, these resemble ring-like structures which we call "gauged Q-rings". Those Q-rings which are closest to the axis quickly collapse back into spherical structures (child gauged Q-balls) which remain on the axis of symmetry for the rest of the evolution. However, those rings which are initially farthest away from the axis of symmetry are observed to propagate outward and can survive for some time. The bottom panel of Figure 2.7 illustrates the behaviour of the gauged Q-rings associated with the decay of L3. The largest Q-ring reaches a maximal distance from the origin of $\rho \approx 40$ before turning around and collapsing back onto the axis of symmetry by $t \approx 500$.

We classify L3 as an unstable configuration. Moreover, we find that all Q-shell solutions on the lower branch of Figure 2.3 are unstable. It is notable that this particular branch of solutions was reported to be stable in Ref. [95] under spherical symmetry assumptions. However, the formation of rings is obviously forbidden under spherical symmetry, so our current results are not inconsistent with previous findings.

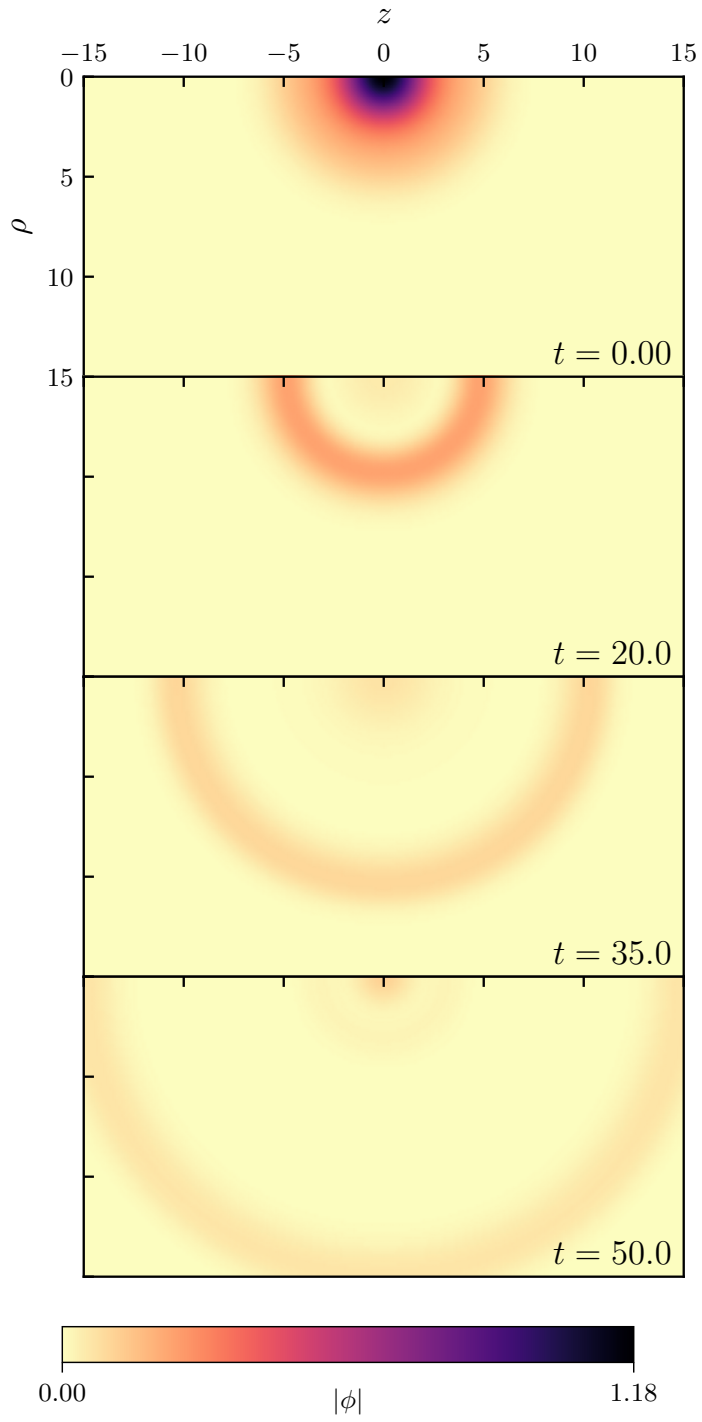

Figure 2.6: Evolution of the scalar field modulus $|\phi|$ for configuration L2 subject to a Type 0 perturbation. Upon evolution, the gauged Q-ball rapidly decays until no significant remnant of the initial configuration remains in the simulation domain. The axis of symmetry is coincident with the top edge of each panel. The simulation domain spans $\{\rho : 0 \leq \rho \leq 50\}$ and $\{z : -50 \leq z \leq 50\}$.

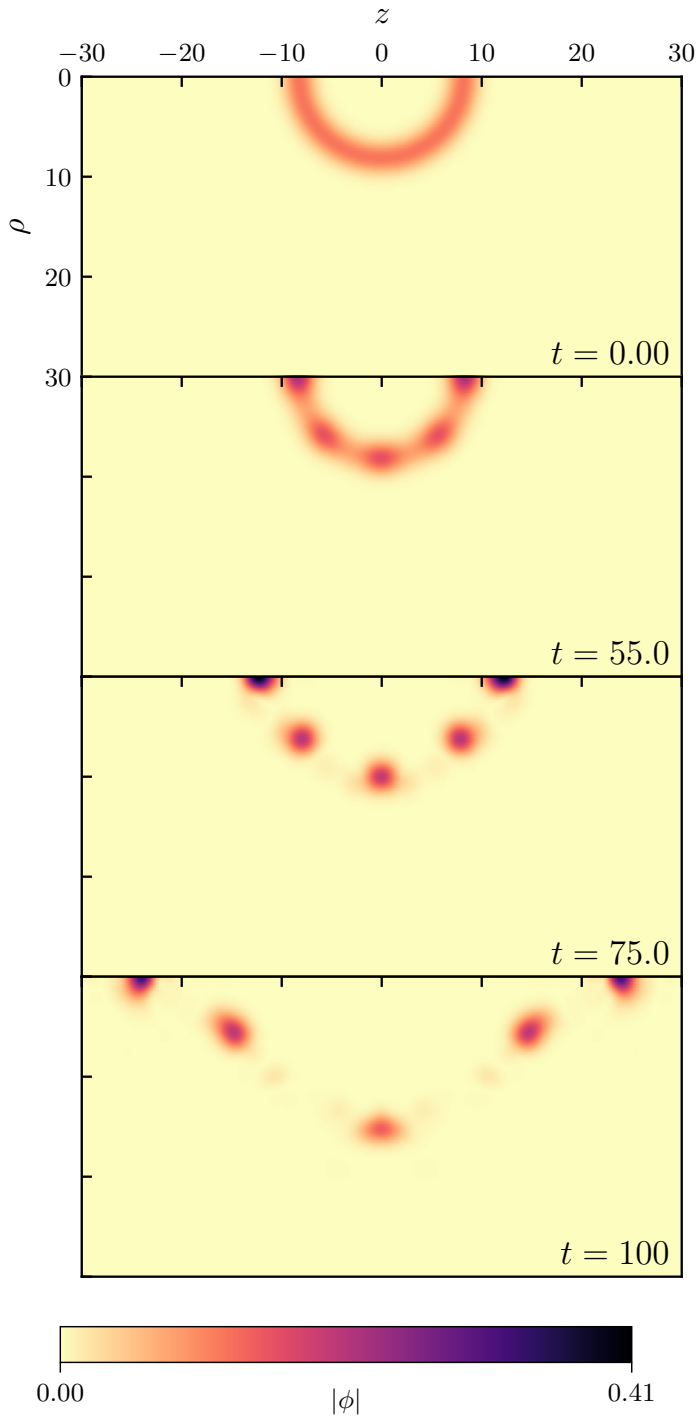

Figure 2.7: Evolution of the scalar field modulus $|\phi|$ for configuration L3 subject to a Type 0 perturbation. Notable in this evolution is the formation of non-spherical ring-like structures which coalesce away from the axis of symmetry and can survive for some time. The axis of symmetry is coincident with the top edge of each panel. The simulation domain spans $\{\rho : 0 \leq \rho \leq 75\}$ and $\{z : -75 \leq z \leq 75\}$.

The formation of gauged Q-rings does not appear to be a unique feature of the decay of L3. We observe a similar phenomenon for other Q-shells on the lower branch of Figure 2.3 as well as for the decay of some unstable gauged Q-balls on the upper branch (though the resulting rings may differ in size and lifetime). We have not been able to find any gauged Q-rings which can survive indefinitely. In each case, the rings propagate outward some finite distance from the axis of symmetry before collapsing back inward and forming a gauged Q-ball. This behaviour is similar to what has been observed for non-gauged Q-balls. In Ref. [77], rings are formed through the high-energy collisions of non-gauged Q-balls which also collapse back inward at late times. Q-ring solitons with semitopological origin have also been considered in Ref. [131]. While the rings observed here do not persist indefinitely, they appear to retain their shape despite the relatively violent dynamics that occur after the decay of L3 (until eventually collapsing onto the axis of symmetry). Since these rings could potentially survive long enough to interact with other structures and produce dynamical effects, we conjecture that they may represent a new type of non-spherical solution in the model.

Finally, let us discuss the evolution of L4. This configuration lies on the upper branch of Figure 2.3 above L2. This configuration is subject only to the Type 0 perturbation. When evolved forward in time, we observe that the modulus of the scalar field quickly grows without bound until large field gradients are produced. These excessive field gradients cannot be numerically resolved by our code even with increasing adaptive mesh refinement, leading to termination of the evolution due to computational constraints. In Figure 2.8, we plot a radial slice of the energy density of the configuration at various points during the evolution. At the initial time, the energy density of the configuration is already negative near the origin. This is likely a consequence of the logarithmic scalar field potential (2.3) being unbounded from below: when the value of $|\phi|$ is large enough, the scalar potential term $V(|\phi|)$ in (2.10) can become negative. If $V(|\phi|)$ dominates locally over the other energies in the system, then the energy density at a point in space can also become negative (even while the total integrated energy remains overall positive). When this configuration is evolved forward in time, it may become energetically favourable for the field in the negative region to grow. At the same time, the field in regions of positive energy density would have to grow to compensate and keep the total integrated energy constant. This runaway process results in the large field gradients and unbounded growth (blowup) observed in Figure 2.8.

While the decay process of L4 may be unphysical, it is not entirely unexpected. Similar phenomena have been observed in other Q-ball models where local energy densities can attain negative values [135, 136]. It is also possible that the decay of L4 could manifest in a different manner (such as dissipation of the fields, similar to L2) if the sign of the initial perturbation to the system could be precisely controlled. However, this level of control is

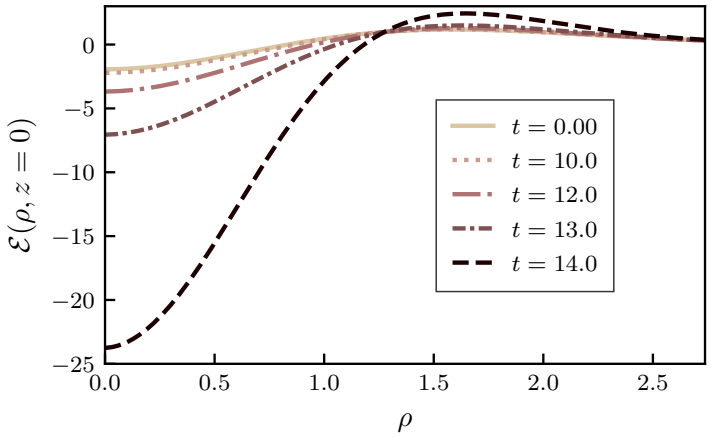

Figure 2.8: Radial slices of the energy density $\mathcal{E}$ of L4 along $z = 0$ at various times during the evolution. Initially, the energy density is negative in a region surrounding the origin and positive elsewhere. As the evolution proceeds, the energy density near the origin grows; the positive region also grows to compensate. Note that the total energy integrates to a positive quantity and is conserved to within 1% over the timescales shown here.

not possible with the Type 0 perturbation, and the fields are found to grow too quickly for Type I perturbations to be effective. In any case, the evolution of L4 results in the destruction of the configuration, and we therefore classify L4 as unstable.

Having discussed the specific configurations L1–L4, we now turn to the general regions of stability and instability depicted in Figure 2.3. The black solid line on the bottom branch indicates the regions of the solution curve which are found to be stable under both Type 0 and Type I perturbations. L1 lies in this region. At the leftmost edge of the bottom branch, we observe a turning point where the gauged Q-ball configurations suddenly become unstable. As this turning point is approached from above, the stable gauged Q-ball configurations become less robust: it becomes possible for a sufficiently large Type I perturbation to "kick" the configuration to the unstable branch, though the same configuration remains stable for smaller-sized perturbations. Due to this effect, it is difficult to exactly determine the location of the onset of instability. However, our numerical experiments suggest that it corresponds with the leftmost edge of the lower branch as depicted in the figure. The region of the curve below this point, marked by a red solid line, is found to be unstable. This region contains L3 along with other Q-shell solutions. Lastly, all portions of the curve along the upper branch (containing L2 and L4) are found to be unstable. The solutions which are found to exhibit the blowup behaviour when subject to Type 0 perturbations (including L4) are indicated by a red dashed line along this curve.

To conclude this section, let us summarize the main dynamical behaviours observed in the logarithmic model. For the stable configurations, we find that small perturbations

remain bounded and the fields remain relatively close to their initial values without any sign of significant growth or decay. For the unstable configurations, we find the most common outcome to be fragmentation into a small number of "child" Q-balls which quickly propagate away along the axis of symmetry. In some cases (such as L3), this process is accompanied by the formation of Q-rings, while in other cases (such as L2), no significant Q-ball or Q-ring remnants are formed. At present, we have been unable to identify a simple criterion which can predict these changes in behaviour. In general, the fragmentation of gauged Q-balls appears to be a complicated non-linear process, with the only guarantee being the conservation of four-momentum and charge.

2.5.2 V_6 Model

Here we consider the dynamical stability of gauged Q-balls in the polynomial model (2.4). For illustrative purposes, we select two configurations P1 and P2 whose properties are listed in Table 2.1. P1 represents an example of a stable evolution for $e = 0.17$ while P2 represents an unstable evolution for $e = 0.02$. For numerical purposes, we set $m = k = 1$ and $h = 0.2$ in all evolutions.

First we consider the evolution of P1. This configuration lies on the shortest curve of Figure 2.2 with $e = 0.17$, which is near the maximum allowable value of $e \approx 0.182$ [96]. The evolution of P1 is subject to a Type I perturbation with parameters $A = 0.1$ and $c = 0.1$ and runs for 65000 base-grid time steps up a final time of $t = 6400$. The maximal value of the scalar field modulus $|\phi|$ and the gauge field component A_0 for this evolution is shown in Figure 2.9. The perturbative scalar field hits the Q-ball at $t \approx 20$ before exploding outward and exiting the simulation domain. After the collision, the Q-ball is left oscillating at the origin around the stationary (unperturbed) configuration. However, the magnitude of this oscillation rapidly decays as the Q-ball quickly returns close to the original configuration. Similar behaviour to P1 is observed for all other solutions tested on the $e = 0.17$ branch depicted in Figure 2.2. We therefore conclude that P1 (as well as all other solutions tested on this branch) is dynamically stable.

Finally, we consider the evolution of P2. This configuration is distinctive in that it occupies a much larger volume than any of the configurations previously considered. In addition, the scalar field profile of P2 is relatively uniform in the center of the Q-ball before dropping off rapidly to zero at a radial distance $r \approx 65$. In this sense it somewhat resembles a Q-ball of the thin-wall type [22]. In Figure 2.10, we show the evolution of P2 subject to a Type 0 perturbation. The distinctive flat-top shape of the configuration is apparent in the first panel of the figure. By $t \approx 525$ (second panel), the original spherical shape of the configuration is lost as the field content begins to concentrate away from the axis of symmetry. At late times, these off-axis concentrations separate into two distinct Q-rings

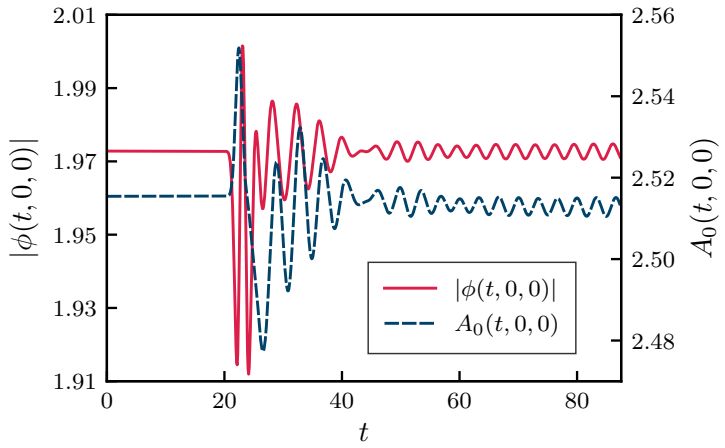

Figure 2.9: Oscillations of the scalar field modulus $|\phi|$ for configuration P1 subject to a Type I perturbation with parameters $c = 0.1$ and $A = 0.1$. Also shown are the oscillations in the maximal value of A_0 (right axis). The perturbative field χ implodes upon the Q-ball at $t \approx 20$ and induces oscillations which quickly decay. By $t \approx 60$, the perturbed Q-ball has returned very nearly to its original configuration.

while a relic region of Q-matter remains near the origin.

In Figure 2.11, we plot the growth of the scalar field modulus $|\phi|$ for configuration P2. Here, the difference $\Delta|\phi| = |\phi(t = 0, \rho, z)| - |\phi(t = 225, \rho, z)|$ illustrates the growth of the solution between the initial time and at a point midway through the evolution (but before the dynamics have entered the non-linear regime). It is clear from the figure that the growth occurs predominantly near the edge of the Q-ball and resembles the pattern of the $Y_{4,0}$ spherical harmonic. This pattern becomes apparent in the evolution by $t \approx 100$ and grows exponentially in amplitude until the Q-ball begins to break apart starting at $t \approx 500$. As mentioned previously, it is well-known that the decay of unstable non-gauged Q-balls is always mediated by a spherically-symmetric mode [133]. However, it remains an open question in the literature as to whether gauged Q-balls can be destroyed by the growth of non-spherical modes. Here we have found an example of an unstable gauged Q-ball where the growth of the dominant unstable mode appears to be non-spherical. Remarkably, this occurs even for a small gauge coupling value of $e = 0.02$. This result is suggestive (though not conclusive) that the destruction of gauged Q-balls can be mediated by non-spherical modes, in contrast to their non-gauged counterparts. However, we emphasize that we have not made any attempt to perform a full stability analysis in this work.

In Figure 2.12, we plot the location of P2 on the $e = 0.02$ curve in the solution space. The curve can be broken down into several distinct branches: an upper unstable branch (I), a stable branch (II), and a lower unstable branch (III) which contains P2. The branch (III) is characterized by solutions which are dominated by a large, nearly-homogeneous

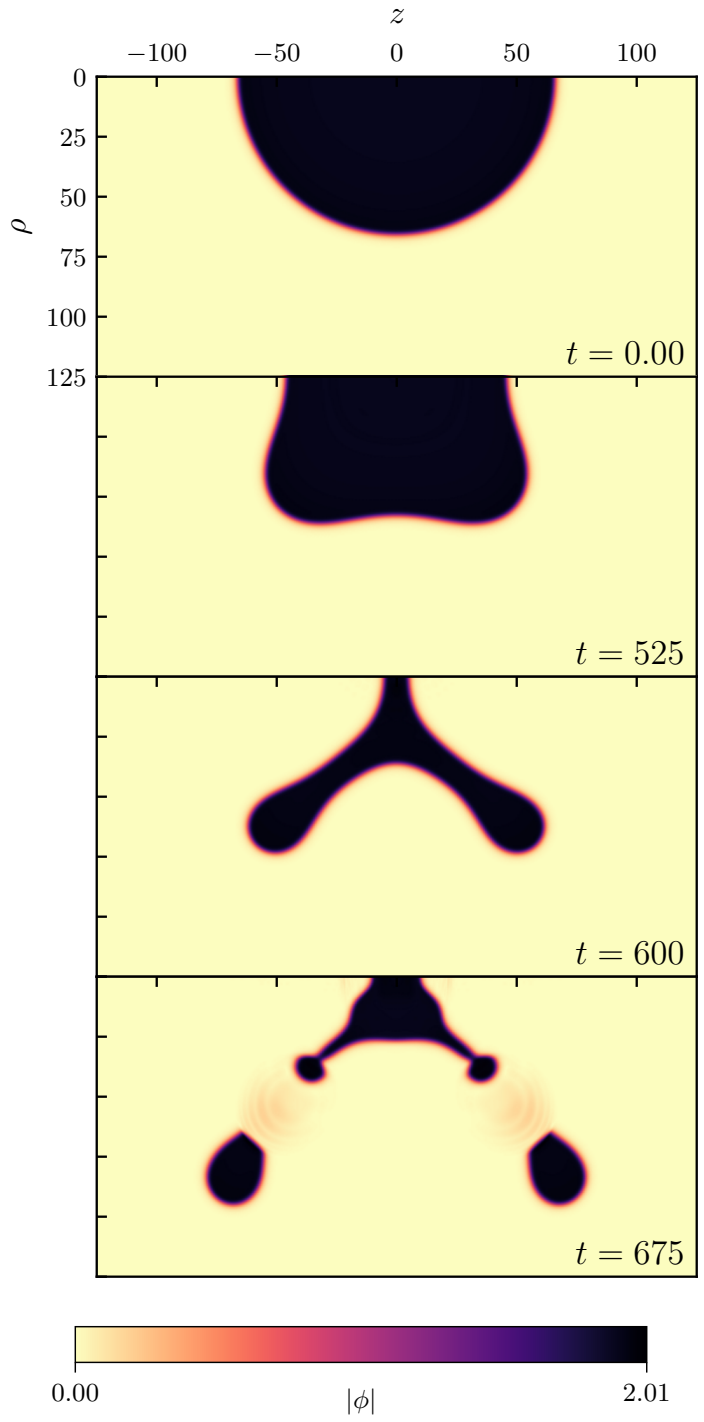

Figure 2.10: Evolution of the scalar field modulus $|\phi|$ for configuration P2 subject to a Type 0 perturbation. As the evolution proceeds, the Q-ball splits into two Q-rings which propagate away from the axis of symmetry. The axis of symmetry is coincident with the top edge of each panel. The simulation domain spans $\{\rho : 0 \leq \rho \leq 150\}$ and $\{z : -150 \leq z \leq 150\}$.

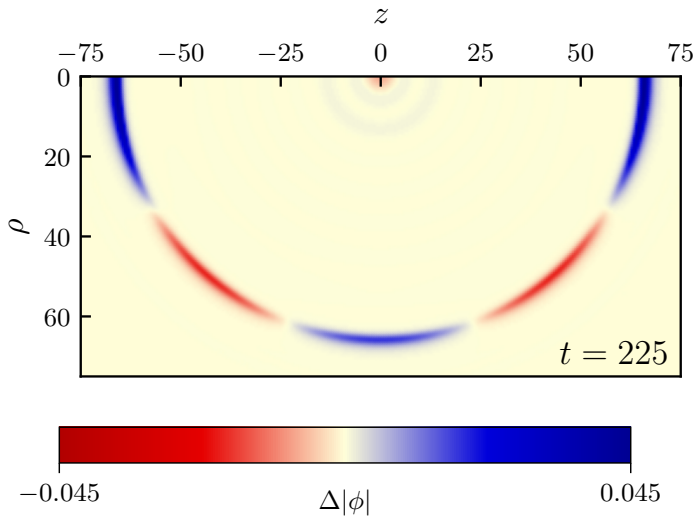

Figure 2.11: Plot of the difference in the scalar field modulus $\Delta|\phi| = |\phi(t = 0, \rho, z)| - |\phi(t = 225, \rho, z)|$ for configuration P2 subject to a Type 0 perturbation. Here, the growth of $|\phi|$ occurs predominantly near the edge of the Q-ball and resembles the pattern of the $Y_{4,0}$ spherical harmonic. The corresponding plot for the full evolution of $|\phi|$ is given in Figure 2.10.

central region and have thin surface boundaries, similar to P2. The radial extent of these solutions increases with ω along branch (III). In most cases, the gauged Q-balls on this branch are found to decay slowly into smaller gauged Q-balls or Q-rings, in contrast to the unstable branch (I) where the instability quickly manifests via complete dispersal of the fields to infinity (similar to L2 in the logarithmic model). However, for some configurations along branch (III) which are close to the transition point with branch (II), we also observe the development of large oscillations in the Q-ball interior which significantly disrupt the shape of the configuration but do not cause the Q-ball to immediately break apart. These oscillations are accompanied by the radiation of charge toward infinity. Since these solutions lose their resemblance to the initial configuration, we also classify them as unstable.

Before concluding, let us comment on the validity of the classical stability criterion (2.1) for $e = 0.02$. Since the gauge coupling is very small for this case, one might expect that the regions of stability should be well-predicted by the sign of $dQ/d\omega$. Indeed, we find this to be the case. The unstable branches (I) and (III) in Figure 2.12 approximately correspond with $(\omega/Q)\, dQ/d\omega > 0$ while solutions on the stable branch (II) approximately correspond with $(\omega/Q)\, dQ/d\omega < 0$. In this sense the gauged Q-balls with $e = 0.02$ closely resemble their non-gauged counterparts. In contrast, we have found the entire space of solutions for $e = 0.17$ to be stable despite the fact that one can find both $(\omega/Q)\, dQ/d\omega > 0$ and $(\omega/Q)\, dQ/d\omega < 0$ for these solutions. This supports the finding that the sign of the

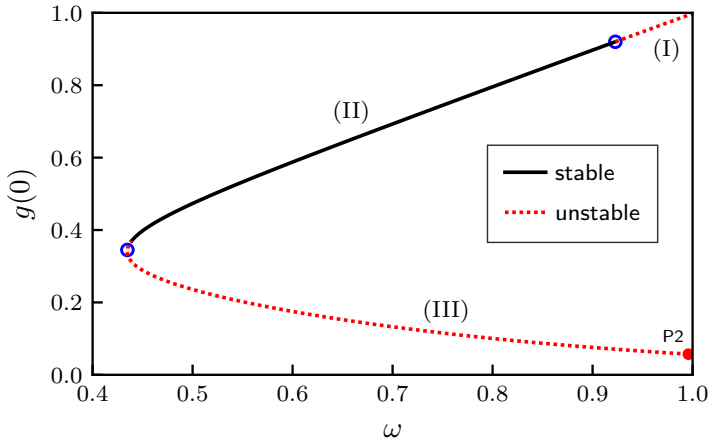

Figure 2.12: Regions of stability and instability for gauged Q-balls in the V_6 model with $e = 0.02$. The point P2 corresponds with the configuration listed in Table 2.1. The dotted red line represents unstable regions (I) and (III) while the solid black line (II) corresponds with stable configurations. The blue circles indicate the transition points between stability and instability as predicted by the classical stability criterion for non-gauged Q-balls (2.1).

criterion (2.1) provides little information on the classical stability of gauged Q-balls when the magnitude of the gauge coupling is appreciable [95].

2.6 Conclusion

We have performed fully non-linear numerical evolutions of $U(1)$ gauged Q-balls in axisymmetry to investigate their stability and dynamics. We assessed this stability in two ways: by perturbing the configurations using the inherent truncation error of the numerical grid, and by introducing an auxiliary massless real scalar field which acts as a perturbing agent designed to explicitly excite any underlying unstable modes. Our simulations suggest that both stable and unstable gauged Q-ball configurations can exist in both the logarithmic and polynomial models. For those solutions which are classified as stable, we observe no evidence of growing modes on the timescales of our evolutions. These solutions respond to perturbations by oscillating continuously or weakly radiating before returning to the original configuration. On the other hand, the decay of unstable configurations can manifest in several different ways, such as total dispersal of the solution, fragmentation into smaller gauged Q-balls, or via the formation of non-spherical ring-like structures which we call "gauged Q-rings". These structures appear to be similar in appearance and behaviour to the rings observed in previous studies of non-gauged Q-ball dynamics [77]. Additionally, for some solutions governed by the logarithmic potential and which attain large field values, we observe that the configurations respond to perturbations by growing without bound. This is similar to behaviour observed in other Q-ball models that permit a negative energy

density and is interpreted as a consequence of the scalar potential being unbounded from below. For the polynomial potential, we have also investigated the dynamical behaviour of gauged Q-balls when the gauge coupling is small. In this case, we find that the regions of stability and instability are well-described by the stability criterion (2.1).

One expected result from our study is that those configurations which were known to be unstable with respect to spherically-symmetric perturbations [95] are also unstable under axisymmetric ones. However, our results indicate that axisymmetric perturbations can lead to new regions of instability in the solution space. Furthermore, we have found that some unstable gauged Q-ball configurations can be destroyed by the growth of modes which appear to be non-spherical. These results suggest that the decay of some gauged Q-ball configurations may be mediated by non-spherical modes, in contrast to non-gauged Q-balls.

While we have presented numerical evidence that gauged Q-balls can be classically stable with respect to axisymmetric perturbations, it is possible that more general perturbations may eventually destroy any gauged Q-ball. Addressing this issue might be accomplished with a fully three-dimensional code. Future work may also focus on trying to explicitly solve for the non-spherical gauged Q-ring configurations and numerically evolving them in order to assess their stability. Another interesting question relates to the interaction of two stable gauged Q-balls, which will be the subject of a future paper.

Lastly, we would like to emphasize that our results have addressed only the classical stability of gauged Q-balls (i.e., stability of the solutions with respect to small perturbations of the fields). For a complete picture of Q-ball behaviour, one may also wish to consider quantum effects. For example, a Q-ball may decay through collective tunnelling or by surface evaporation when coupled to additional fields [98, 137–139]. It is interesting to ask whether the stability of gauged Q-balls is maintained once these effects are considered, though such a question is beyond the scope of the present work.

Chapter 3

Relativistic Head-on Collisions of $U(1)$ Gauged Q-balls

3.1 Introduction

The study of non-linear wave equations has a long and rich history in modern physics[1]. One of the most remarkable insights to emerge from this tradition has been the discovery of *solitons*: localized solutions to the field equations that can propagate without dispersing. In many respects, solitons behave like a rudimentary model of a particle which can be constructed from smooth classical fields. They can generally be classified as either topological or non-topological depending on whether the underlying model has a non-trivial topology. Examples of topological solitons include the kink/anti-kink solutions of quantum field theory, skyrmions and vortices in condensed matter physics, and cosmological domain walls [16, 17]. In contrast, non-topological solitons can arise due a balancing between the effects of non-linearity and dispersion and are often characterized by the existence of a conserved Noether charge [17]. The prototypical examples of non-topological solitons are *Q-balls* which arise in complex scalar field theories admitting a $U(1)$ symmetry.

The study of Q-balls began in earnest with the work of Coleman [27, 28] who described them as localized solutions of a complex scalar field theory with a non-linear attractive potential and a global $U(1)$ symmetry. This work has since been extended to show that Q-ball solutions can arise in a variety of physically-motivated models (see [125] for a review). In the context of cosmology and particle physics, Q-balls may be relevant for various early-Universe scenarios such as baryogenesis and the dark matter problem [30, 31, 34, 35]. They may also arise in the context of non-linear optics [140] and condensed matter systems [68, 69]. Mathematically, Q-balls are characterized by the presence of a conserved Noether

[1]The content of this chapter has previously been published in [2].

charge Q which is associated with the $U(1)$ symmetry of the theory. The global $U(1)$ symmetry can also be made into a local $U(1)$ symmetry via the introduction of a $U(1)$ gauge field; the resulting solutions are called *gauged Q-balls* and represent a coupling of the system to electromagnetism [84].

While the basic properties of Q-balls are well-known, it remains a challenging problem to model their full time-dependent dynamical behaviour. This is due mainly to the non-linear structure of the underlying equations which typically requires a numerical treatment. Early work on this topic revealed that Q-ball dynamics can be remarkably complex, particularly when considering interactions and relativistic collisions of Q-balls. Perhaps the most comprehensive studies of this type were performed by Axenides *et al.* in two spatial dimensions [74] and Battye and Sutcliffe in three spatial dimensions [77]. There it was shown that Q-balls can interact elastically or inelastically depending on the collision parameters. They may also transfer charge, annihilate, or form oscillatory charge-swapping structures [47–49] under the right conditions. Additional studies have also considered different scalar field models, higher collision velocities, or greater numerical resolutions [72, 75, 76, 78, 80]. A general conclusion to be drawn from these studies is that Q-ball behaviour can be quite complex and unexpected.

In the present paper, we continue this exploration of Q-ball dynamics by considering relativistic head-on collisions of $U(1)$ gauged Q-balls in axisymmetry. Intuitively, one might expect that the addition of the $U(1)$ gauge field may lead to novel dynamical behaviour due to the interaction of electromagnetic charges and currents. However, this possibility has remained largely unexplored in the literature. Our aim is to shed light on this topic by performing fully non-linear numerical evolutions of the field equations in axisymmetry. We explore the effects of various collision parameters such as the initial velocity, relative phase, relative charge, and electromagnetic coupling strength in order to gain insight on the general phenomenology of gauged Q-ball collisions.

In a previous paper [1], we numerically investigated the dynamical behaviour of $U(1)$ gauged Q-balls when subject to axisymmetric perturbations. There it was found that stable gauged Q-ball configurations can exist in both logarithmic and polynomial models. Using these solutions as a starting point, we construct binary gauged Q-ball initial data consisting of two stable solutions which are boosted toward each other at relativistic velocities. We then evolve the system according to the equations of motion and observe the subsequent dynamics.

When the gauge coupling is small, our results parallel those found for ordinary (non-gauged) Q-ball collisions. Specifically, we find that the collision dynamics can be divided into three regimes—which we will call the *elastic*, *fragmentation*, and *merger* regimes—depending on the incident velocity of the colliding Q-balls. In the elastic regime (corre-

sponding to high velocities), the collisions are primarily elastic with the Q-balls passing through each other virtually unscathed and forming a destructive interference pattern at the moment of impact. In the merger and fragmentation regimes (corresponding to low and intermediate velocities, respectively), the collisions are primarily inelastic with several possible outcomes. At the lowest velocities, the Q-balls can merge into a single Q-ball of a larger size, while at intermediate velocities they tend to fragment into many pieces. We also investigate collisions of oppositely-charged and phase-shifted Q-balls, finding evidence for annihilation and charge transfer, respectively.

When the gauge coupling is large, we find that electromagnetic effects can significantly alter the outcome of the collision. For gauged Q-balls with charge of equal sign, we find that the Coulomb repulsion tends to decelerate the Q-balls prior to the moment of impact. At low incident velocities, this can prevent the interaction of the Q-ball fields entirely; at higher velocities, it simply reduces the effective collision velocity. We also find that collisions at large gauge coupling are rarely an elastic process. Unlike the free-passage behaviour observed for small gauge coupling, the collision of gauged Q-balls at high-velocities tends to result in the formation of ring-like objects (which we have previously called "gauged Q-rings" [1]) or elongated structures even for collision velocities very close to the speed of light. For collisions involving Q-balls of unequal phase, we again observe charge transfer similar to the case of small gauge coupling. However, we find that the gauged Q-balls created in this process often break apart, presumably due to the reduced range of stable solutions which exist at large gauge coupling. For collisions of oppositely-charged Q-balls, the Coulomb force accelerates the Q-balls prior to the moment of impact. These collisions can result in the annihilation of significant charge and the production of an electromagnetic radiation pulse. In sum, we find that the collision of gauged Q-balls can be a violent process with some striking differences when compared to the non-gauged case.

The outline of this paper is as follows: in Section 3.2, we briefly review the theory of $U(1)$ gauged Q-balls. In Section 3.3, we summarize our numerical approach to the head-on collision problem. In Section 3.4, we present our main results and summarize the general dynamics observed for $U(1)$ gauged Q-ball collisions. In Section 3.5, we provide some concluding remarks.

In this work, we use units where $c = \hbar = 1$ and employ the metric signature $(-,+,+,+)$. For brevity, we will interchangeably use the terms "Q-ball" and "gauged Q-ball" when referring to Q-balls coupled to the electromagnetic field. When referring to Q-balls which do not admit any such coupling, we will explicitly use the term "non-gauged Q-ball".

3.2 Review of $U(1)$ Gauged Q-balls

For a system composed of a complex scalar field ϕ coupled to a $U(1)$ gauge field, A_μ, the Lagrangian density takes the form

$$\mathcal{L} = -\left(D_\mu\phi\right)^* D^\mu\phi - V\left(|\phi|\right) - \frac{1}{4}F_{\mu\nu}F^{\mu\nu}. \tag{3.1}$$

Here, $F_{\mu\nu} = \partial_\mu A_\nu - \partial_\nu A_\mu$ is the electromagnetic field tensor, $D_\mu = \nabla_\mu - ieA_\mu$ describes the gauge covariant derivative with coupling constant e, and $V(|\phi|)$ represents a $U(1)$-invariant scalar field potential. The equations of motion for the theory (3.1) take the form

$$D_\mu D^\mu\phi - \frac{\partial}{\partial\phi^*}V(|\phi|) = 0, \tag{3.2}$$

$$\nabla_\mu F^{\mu\nu} + ej^\nu = 0, \tag{3.3}$$

where j^ν is the Noether current density,

$$j^\nu = -i(\phi^* D^\nu\phi - \phi(D^\nu\phi)^*). \tag{3.4}$$

This quantity can be integrated to obtain the conserved Noether charge $Q = \int j^0\, d^3x$ associated with the $U(1)$ symmetry of the theory. Likewise, there exists a conserved energy $E = \int T_{00}\, d^3x$ which can be computed from the energy-momentum tensor of the theory,

$$\begin{aligned} T_{\mu\nu} = & F_{\mu\alpha}F_{\nu\beta}g^{\beta\alpha} - \frac{1}{4}g_{\mu\nu}F_{\alpha\beta}F^{\alpha\beta} \\ & + D_\mu\phi(D_\nu\phi)^* + D_\nu\phi(D_\mu\phi)^* \\ & - g_{\mu\nu}(D_\alpha\phi(D^\alpha\phi)^* + V(|\phi|)). \end{aligned} \tag{3.5}$$

Solutions to the equations of motion (3.2)–(3.3) which represent gauged Q-balls can be found by making a spherically-symmetric ansatz for the fields,

$$\phi(t,\vec{x}) = f(r)e^{i\omega t}, \tag{3.6}$$

$$A_0(t,\vec{x}) = A_0(r), \tag{3.7}$$

$$A_i(t,\vec{x}) = 0, \tag{3.8}$$

and imposing the boundary conditions

$$\lim_{r\to\infty} f(r) = 0, \qquad \frac{df}{dr}(0) = 0, \tag{3.9}$$

$$\lim_{r\to\infty} A_0(r) = 0, \qquad \frac{dA_0}{dr}(0) = 0. \tag{3.10}$$

This ansatz yields the reduced equations of motion

$$f''(r) + \frac{2}{r}f'(r) + f(r)g(r)^2 - \frac{1}{2}\frac{d}{df}V(f) = 0, \tag{3.11}$$

$$A_0''(r) + \frac{2}{r}A_0'(r) + 2ef(r)^2 g(r) = 0, \tag{3.12}$$

where we have defined $g(r) = \omega - eA_0(r)$. There are several approaches to finding solutions which satisfy the coupled equations (3.11)–(3.12) such as shooting [84], relaxation [94], or via mapping from the profiles of non-gauged Q-balls [89]. Here we utilize an iterative shooting procedure to numerically determine $f(r)$ and $A_0(r)$ which satisfy (3.11)–(3.12) to a good approximation. Further details about this technique are provided in [1].

3.3 Numerical Approach

As a starting point for our evolution, we consider the line element

$$ds^2 = -dt^2 + d\rho^2 + \rho^2 d\varphi^2 + dz^2 \tag{3.13}$$

where (t, ρ, φ, z) are the standard cylindrical coordinates. Further, we impose axisymmetry on the system by requiring all dynamical variables to be φ-independent. This is done purely to reduce the computational cost of modelling the system in fully three spatial dimensions. With this choice, the equations of motion (3.2)–(3.3) can be expressed as a set of six coupled non-linear partial differential equations; these equations are identical to those listed in the appendix of our previous paper [1]. Working in the Lorenz gauge, the equations of motion are supplemented with the gauge condition

$$\nabla_\mu A^\mu = 0, \tag{3.14}$$

and the equations

$$\nabla_i E^i = e j^0\,, \tag{3.15}$$

$$\nabla_i B^i = 0\,, \tag{3.16}$$

where E^i and B^i are the (three-dimensional) electric and magnetic field vectors, respectively, whose components are determined via the electromagnetic field tensor, $F_{\mu\nu}$. Together, the equations (3.14)–(3.16) act as additional constraints on the evolution: it is expected that a numerical solution to the equations of motion will approximately satisfy these constraint equations at any given time.

In order to construct initial data which is suitable for studying head-on collisions, we

interpolate a pair of spherically-symmetric gauged Q-ball solutions in the $\rho - z$ plane using Neville's algorithm to fourth-order in the mesh spacing [23]. The center of each Q-ball is chosen to coincide with the line $\rho = 0$ in order to preserve the spherical symmetry of each Q-ball in the binary. Each Q-ball is also given an initial displacement along the z-axis so that the binary is well-separated at the initial time. Finally, we apply a Lorentz boost to each Q-ball along the z-direction at a relativistic speed v (where $v = 1$ corresponds to the speed of light in our units) so that they travel toward each other. After these operations, the field variables $f \in \{\phi, \partial_t\phi, A_\mu, \partial_t A_\mu\}$ are initialized according to the linear superposition

$$f(\rho, z) = f_A(\rho, z) + f_B(\rho, z), \tag{3.17}$$

subject to the condition

$$f_A(\rho, z) \cdot f_B(\rho, z) \approx 0, \tag{3.18}$$

where the subscripts $\{A, B\}$ identify each individual Q-ball in the binary.

Practically speaking, the condition (3.18) is not trivial to satisfy in general. While the scalar field falls off exponentially away from the Q-ball center (thereby satisfying the condition even at modest separation distances), the same cannot be said for the gauge field, which falls off like $1/r$. This long-range behaviour inherently introduces violations of the constraint equations (3.14)–(3.16) when the gauge fields of each Q-ball significantly overlap. The magnitude of this violation depends on several factors such as the initial separation distance, the boost velocity, and the total charge of the constituent Q-balls. To deal with this problem, we implement an FAS multigrid algorithm [23] to re-solve the equations (3.15)–(3.16) at the initial time and minimize the constraint violation for arbitrary superpositions of the form (3.17). We also monitor the residuals of the constraint equations (3.14)–(3.16) during the evolution to ensure that they do not grow significantly over the timescales under consideration.

For the purposes of this work, we choose several representative examples of gauged Q-ball solutions to act as initial data for the colliding binaries. The properties of these solutions are listed in Table 3.1. In our simulations, we consider two different possibilities for the scalar field potential $V(|\phi|)$ in the model (3.1). These are

$$V_{\log}(|\phi|) = -\mu^2|\phi|^2 \ln(\beta^2|\phi|^2), \tag{3.19}$$

$$V_6(|\phi|) = m^2|\phi|^2 - \frac{k}{2}|\phi|^4 + \frac{h}{3}|\phi|^6, \tag{3.20}$$

where μ, β, m, k, and h are real, positive parameters. In Table 3.1, the solutions pertaining to the logarithmic potential (3.19) are named LogA, LogB and LogC while the solutions due to the polynomial potential (3.20) are named PolyA and PolyB. These solutions, which

are known to be stable against axisymmetric perturbations [1], are specifically chosen to illustrate the range of dynamical features associated with head-on collisions of gauged Q-balls. We emphasize that aside from the examples listed in Table 3.1, we have also studied collisions involving several other configurations and find the dynamics to be consistent with the results reported below.

In addition to varying the scalar potential, we also adjust the values of the electromagnetic coupling constant e, the initial velocity v, the relative phase difference α, and the relative sign of the Noether charge Q for the colliding Q-balls. The value of α is set through a simple modification of the spherical Q-ball ansatz (3.6):

$$\phi(t, \vec{x}) = f(r)\, e^{\epsilon(i\omega t)+i\alpha}, \tag{3.21}$$

where $\alpha \in [0, \pi]$ and $\epsilon = \pm 1$. Since we only consider collisions between Q-balls with identical ω, the value of α determines the relative difference in phase between the colliding Q-balls prior to the moment of impact. The sign of ϵ, meanwhile, provides a mechanism through which we can study both Q-ball/Q-ball and Q-ball/anti-Q-ball collisions. This can be understood from the fact that the sign of the Noether charge Q (and the sign of the electric charge $Q_e = eQ$) of a gauged Q-ball is connected to the sign of the oscillation frequency ω [94]. Therefore, adjusting the sign of ϵ for one Q-ball in the binary (as well as taking $A_0(r) \to -A_0(r)$ in (3.7)) effectively flips the sign of its charge, allowing us to superpose initial data of equal or opposite charge as desired.

After specifying the initial data at $t = 0$, we proceed by evolving the system forward in time. To facilitate this, we invoke a coordinate transformation $x^\mu = (t, \rho, z) \to x^{\mu'} = (t, P, Z)$ according to

$$\rho = d \exp(cP) - d \exp(-cP), \tag{3.22}$$

$$z = d \exp(cZ) - d \exp(-cZ), \tag{3.23}$$

where c and d are positive, real parameters. With appropriate choice of c and d, the transformation (3.22)–(3.23) remains approximately linear near the origin while becoming increasingly compactified at large coordinate values. This is an attractive feature for our numerical domain because it allows us to resolve the dynamics at large length scales without incurring an excessive computational cost. To perform the evolution in this coordinate system, we use a second-order Crank-Nicolson finite-difference scheme implemented with fourth-order Kreiss-Oliger dissipation as a smoothing operator. A modified Berger-Oliger adaptive mesh refinement (AMR) algorithm [118] is used to dynamically increase the numerical resolution of our simulations in the regions of greatest interest. For all results presented below, the base grid is taken to be 129 by 257 grid points in $\{P, Z\}$ with up to 8 levels

Solution	e	$\lvert\phi(0,0)\rvert$	$A_0(0,0)$	ω	E	$\lvert Q\rvert$
LogA	0.1	0.3669	2.697×10^{-2}	2.003	6.769	3.006
LogB	0.1	1.627	0.2682	1.027	45.45	30.03
LogC	1.1	0.6461	1.383	2.522	52.08	22.37
PolyA	0.02	2.062	0.4353	0.6587	476.4	582.9
PolyB	0.17	1.973	2.515	0.9976	405.1	387.5

Table 3.1: Table of several gauged Q-ball solutions used in our collision simulations. The solutions LogA, LogB and LogC correspond to the logarithmic potential (3.19) while PolyA and PolyB correspond to the polynomial potential (3.20). From left to right, the remaining columns indicate the value of the electromagnetic coupling constant e, the initial central value of the scalar field $|\phi(0,0)|$, the initial central value of the gauge field $A_0(0,0)$, the Q-ball oscillation frequency ω, the total energy E of the solution (when stationary), and the total Noether charge $|Q|$ of the solution.

of additional mesh refinement at a refinement ratio of 2:1. We choose a Courant factor of $\lambda = dt/\min\{dP, dZ\} = 0.25$. At the outer boundaries, we impose outgoing (Sommerfeld) boundary conditions in order to accommodate the long-range behaviour of the electromagnetic field and reduce the effects of spurious boundary noise. In addition, we apply reflective or anti-reflective boundary conditions as necessary along the axis of symmetry in order to enforce regularity.

For numerical convenience, we choose $\mu = \beta = m = k = 1$ and $h = 0.2$ in (3.19)–(3.20) following our previous work [1]. We select $c = 0.05$, $d = 10$ in (3.22)–(3.23) and set the domain boundaries to span at least $\{P : 0 \leq P \leq 50\}$ and $\{Z : -50 \leq Z \leq 50\}$ which corresponds to $\{\rho : 0 \leq \rho \lesssim 121\}$ and $\{z : -121 \lesssim z \lesssim 121\}$ in the original coordinate system. With this choice, we find the numerical domain to be large enough to capture the relevant post-collision dynamics of the Q-balls. We emphasize that while all evolutions have been performed using the compactified coordinates P and Z, we will hereafter present all results using the linear coordinates ρ and z. This is done primarily to facilitate the interpretation of the results. Finally, since the numerical code is identical to the one used in [1] (aside from applying the coordinate transformation (3.22)–(3.23) and the generation of binary initial data), we refer the reader to [1] for issues of code validation such as convergence and independent residual tests.

3.4 Numerical Results

We now describe the results of our numerical experiments. In our collision simulations, we consider the effects of the following parameters on the resulting dynamics: gauge coupling

strength e, collision velocity v, relative phase difference α, and relative sign of the Noether charge Q. In most cases, we restrict the collision velocity to the range $0.1 \leq v \leq 0.9$ and the phase difference to $\alpha \in \{0, \pi/4, \pi/2, 3\pi/4, \pi\}$, though in some cases we explore beyond these values to get a complete picture of the dynamics. Further, we test the effects of the choice of scalar potential (logarithmic (3.19) versus polynomial (3.20)) as well as the difference between colliding Q-balls of equal charge and opposite charge. We note that for all simulations presented below, the constituent Q-balls are always composed of identical charge magnitudes (i.e., we do not present any results for collisions between Q-balls of differing $|Q|$). For comparison purposes, we first explore the results at small gauge coupling. We then move on to the case where the gauge field is strongly coupled to highlight the salient dynamics. For presentation purposes, we have relegated some plots of the dynamics in this section to Appendix B.1.

We provide in Table 3.2 a broad, high-level overview of the main results of our numerical experiments. We will devote the remainder of this work to discussing the various phenomena which are reflected in the table.

3.4.1 Small Gauge Coupling

Here we consider collisions involving solutions LogA, LogB, and PolyA from Table 3.1. Since the strength of the gauge coupling is small in these cases (see [93] where this notion is made precise), it is expected that the dynamics of gauged Q-balls in this regime will be similar to the dynamics of ordinary (non-gauged) Q-balls.

Let us begin by discussing the effect of Q-ball velocity on the outcome of the collision. In previous studies [74, 77, 80] it has been shown that the dynamics of equal-charge, non-gauged Q-ball collisions can generally be divided into three regimes: (i) at low velocities, a "merger" regime wherein the Q-balls tend to coalesce, (ii) at intermediate velocities, a "fragmentation" regime wherein the Q-balls tend to break up into smaller components, and (iii) at high velocities, an "elastic" regime wherein the Q-balls tend to pass through each other virtually unscathed. We find that gauged Q-ball collisions with small gauge coupling are generally consistent with these previous findings.

First, consider the low-velocity regime. In Figure 3.1, we plot the collision of two Q-balls of type LogA (see Table 3.1) with equal charge, velocity $v = 0.1$, and phase difference $\alpha = 0$. As the Q-balls collide, they merge temporarily before separating again and propagating a short distance along the axis of symmetry. However, they have insufficient kinetic energy to completely escape their mutual influence and instead repeatedly merge and partially separate. Small amounts of scalar matter are also released during this process. As the evolution proceeds, the field configuration settles down into a single coherent merged state. The final Q-ball is of a larger total size than LogA and remains at the origin lightly perturbed.

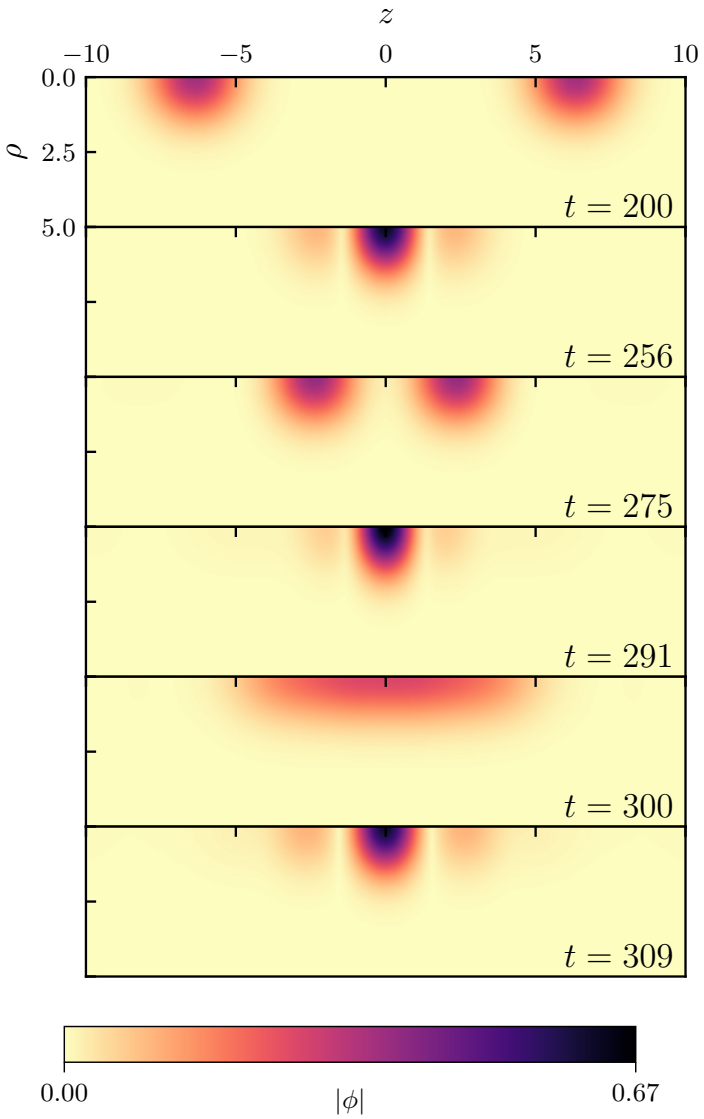

Figure 3.1: Evolution of the scalar field modulus $|\phi|$ for a collision of solutions of type LogA with equal charge, velocity $v = 0.1$, and phase difference $\alpha = 0$. The Q-balls collide at $t \approx 250$ and repeatedly merge and separate. By $t \approx 600$ (beyond what is shown here), the field configuration settles down into a single larger Q-ball which remains perturbed at the origin.

Collision Parameters			Result	
Relative Charge Q	Phase Difference α	Collision Velocity v	Small e	Large e
Equal Q	$\alpha = 0$	Low v	Merger	Coulomb repulsion (no collision)
		Intermediate v	Merger, fragmentation	Merger, fragmentation
		High v	Free-passage	Fragmentation
	$\alpha \in (0, \pi)$	Low v	Charge transfer	Coulomb repulsion (no collision)
		Intermediate & High v		Charge transfer, fragmentation
	$\alpha = \pi$	Low v	Phase repulsion	Coulomb repulsion (no collision)
		Intermediate & High v		Phase repulsion
Opposite Q	All α	All v	Partial annihilation	Partial annihilation, radiation emission

Table 3.2: Summary of the main dynamical results from our collision simulations. Shown are the observed collision outcomes (classified by either "small" or "large" values of the gauge coupling constant e) as a function of various collision parameters: the relative Noether charge Q of the colliding binary (either equal or opposite), the relative phase difference α, and the collision velocity v (heuristically divided into "low-velocity", "intermediate-velocity", and "high-velocity" regimes). We comment that the results listed in this table together capture the dynamics in both the logarithmic (3.19) and polynomial (3.20) scalar field models. These results are explained in further detail throughout Section 3.4.

When boosted to velocities above a certain threshold, the colliding Q-balls have sufficient kinetic energy to avoid a merged final state (for LogA, the velocity threshold is $v \gtrsim 0.125$). At these "intermediate" velocities, a significant quantity of the initial charge of each Q-ball continues propagating along the axis of symmetry after the collision. These resulting Q-balls are highly perturbed and oscillatory. In most cases, this process also results in some relic amount of charge left behind: the Q-balls have partially fragmented into smaller structures. These smaller Q-balls may either remain stationary at the origin or continue to propagate along the axis of symmetry, lagging the main Q-balls at a lower velocity. An example of such a collision for solution LogA at velocity $v = 0.5$ is given in Appendix B.1 (Figure B.1).

At the highest velocities, collisions between the Q-balls are primarily elastic and they emerge from the collision relatively unscathed. An illustration of this phenomenon is given in Appendix B.1 (Figure B.2) for solution LogA at velocity $v = 0.9$. It is also in this regime that the wave-like nature of Q-balls becomes readily apparent through the appearance of interference fringes at the moment of impact. Plotted in Figure 3.2 are the interference fringes observed for collisions of solution LogA at $v = 0.9$. For equal-charge collisions, a clear fringe pattern emerges with fringe spacing inversely proportional to the collision velocity. Also shown are the effects of opposite-charge and phase-difference collisions on the fringe pattern (to be discussed below).

We now comment on the effects of phase difference on the collision dynamics. Recall that a phase difference is introduced into the system by choosing $\alpha \neq 0$ in (3.21). Since the colliding Q-balls in our study always have identical values of ω, this phase difference is preserved until the moment of impact regardless of the initial separation distance or initial velocity. As reported previously [77], the main effect of this phase difference is to induce charge transfer between the colliding Q-balls. This behaviour can be understood in terms of relative phase accelerations [77] or the induced rate of change of momentum for the colliding Q-balls [79]. Testing the effects of phase difference at $\alpha \in \{0, \pi/4, \pi/2, 3\pi/4, \pi\}$, we find that charge transfer is generally maximized at the lowest collision velocities and for small phase differences, in agreement with previous studies.

Plotted in Figure 3.3 is the collision of solution LogA at a velocity of $v = 0.1$ and a phase difference $\alpha = \pi/4$. Initially, the Q-balls are of equal charge. At the moment of impact, the Q-ball with lagging phase (rightmost Q-ball in the figure) suddenly gains charge from the Q-ball with leading phase (leftmost Q-ball). Since Q-balls are extended structures, it can be difficult to precisely determine the total charge Q contained in the resulting objects. However, by integrating Q in the half-volumes $z > 0$ and $z < 0$ after the collision takes place, we can estimate by the deviation from symmetry that approximately 18% of the charge is transferred during this process. We note that the total charge Q over the simulation domain remains conserved to within 0.1% during the evolution. In addition

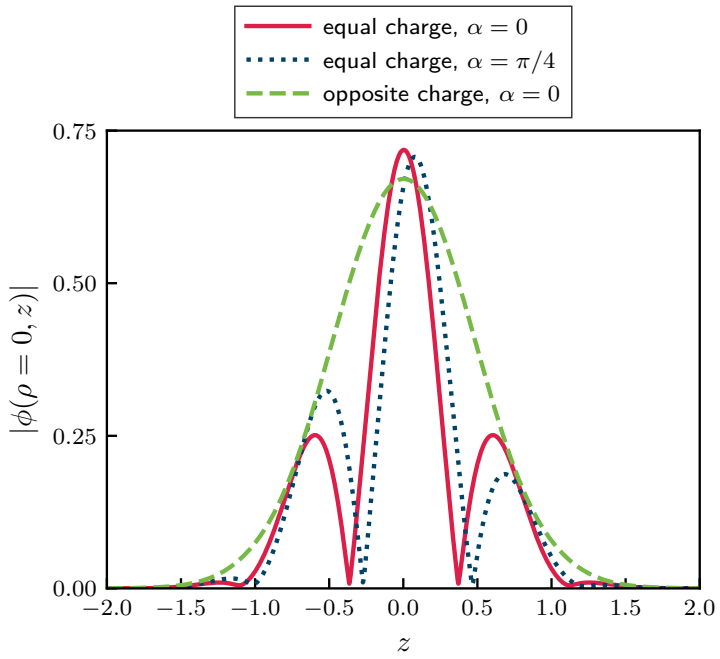

Figure 3.2: Profiles of the scalar field modulus $|\phi|$ evaluated along the axis of symmetry during collisions involving solution LogA with $v = 0.9$. Three cases are shown: an equal-charge collision with no phase difference ($\alpha = 0$), an equal-charge collision with phase difference $\alpha = \pi/4$, and an opposite-charge collision with no phase difference ($\alpha = 0$). In each case, the profile is shown at the moment $|\phi|$ reaches its maximal value. For collisions with equal charge, a destructive interference pattern forms at the moment of impact. For collisions with opposite charge, the interference pattern is purely constructive.

to charge transfer, we observe that the velocities of the resultant Q-balls after the collision are no longer identical: the smaller Q-ball moves faster than the larger one. This can be understood as a straightforward consequence of linear momentum conservation.

At intermediate velocities, we observe the same qualitative behaviour, though with the amount of charge transfer reduced (for instance, only $\sim 7\%$ is transferred at $v = 0.5$, $\alpha = \pi/4$ for solution LogA). In some cases, the charge transfer at these velocities is accompanied by the formation of one or more smaller Q-balls which remain along the axis of symmetry after the collision and lag the main Q-balls, being slightly perturbed. At the highest velocities, the charge transfer is minimal (for instance, $\sim 1\%$ or less of the charge is transferred with $v \gtrsim 0.9$, $\alpha = \pi/4$ for solution LogA) and no significant smaller Q-balls are formed during the collision. However, the phase difference still manifests through a distortion of the interference fringes as illustrated in Figure 3.2.

A notable exception to the charge transfer phenomenon occurs for completely out-of-phase collisions ($\alpha = \pi$). In this case, the Q-balls exhibit a purely repulsive interaction as they "bounce" off each other. At the moment of impact, the Q-balls are compressed in the

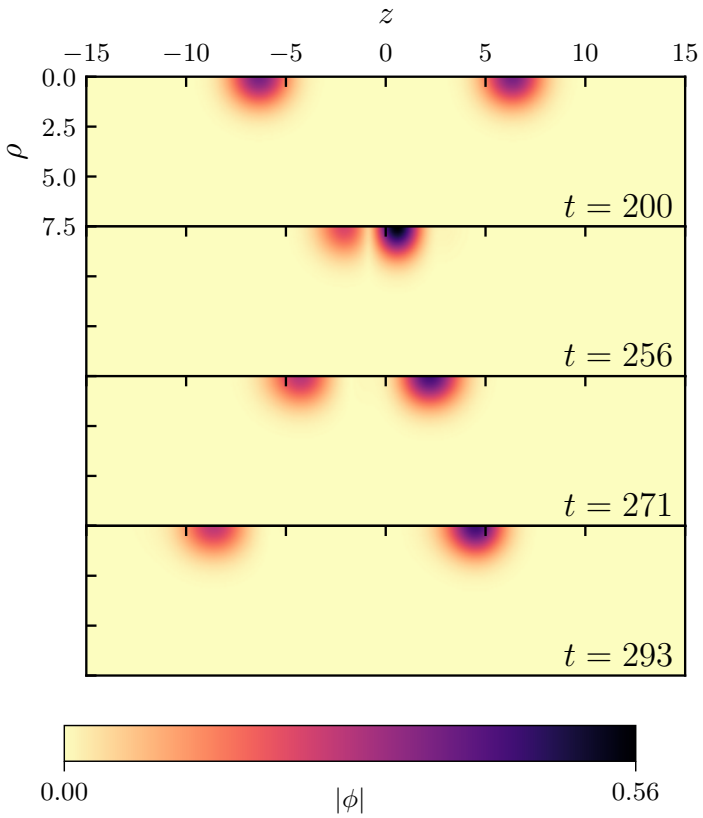

Figure 3.3: Evolution of the scalar field modulus $|\phi|$ for a collision of solutions of type LogA with equal charge, velocity $v = 0.1$, and phase difference $\alpha = \pi/4$. After colliding at $t \approx 250$, the Q-ball with leading phase (left) transfers charge to the Q-ball with lagging phase (right). After the collision, the Q-balls have disparate velocities.

boost direction and the value of $|\phi|$ temporarily grows by an amount which is proportional to the collision velocity. There is no charge transfer observed: the half-volumes $z > 0$ and $z < 0$ contain an identical amount of charge for all time. Note that this repulsive behaviour for out-of-phase collisions has also been observed in other soliton models [141, 142].

We now discuss collisions of oppositely-charged Q-balls. These are the ones for which $\epsilon = -1$ in equation (3.21) for one of the Q-balls in the binary, resulting in a system composed of a gauged Q-ball and gauged anti-Q-ball. These collisions are predominantly characterized by the possibility of charge annihilation at the moment of impact, with the amount of annihilation depending on the collision velocity. For example, an opposite-charge collision corresponding to solution LogA at $v = 0.1$ results in $\sim 48\%$ of the charge annihilated. This situation is depicted in Figure 3.4. The remaining charge emerges from the collision in the form of smaller Q-balls with a larger velocity. In addition, the relatively violent dynamics that occur during the annihilation leave them highly perturbed and oscillatory after the

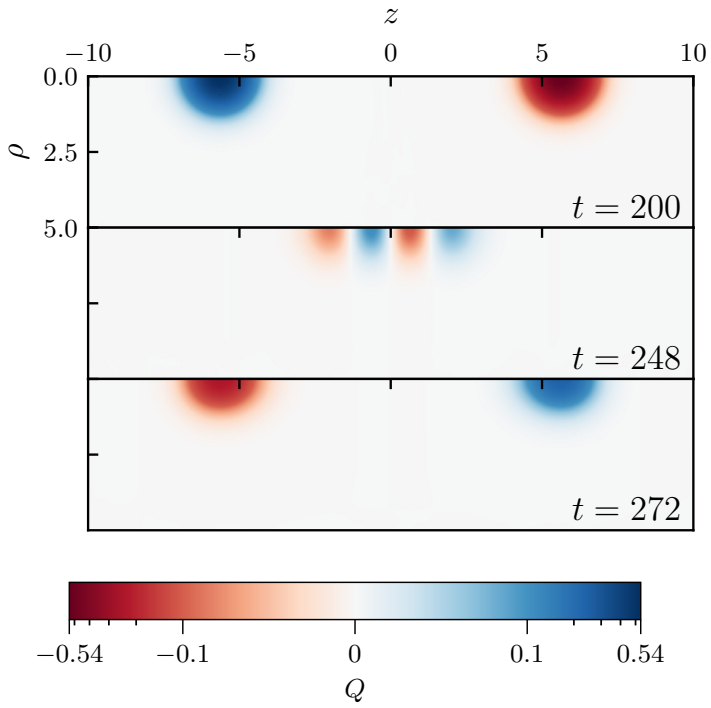

Figure 3.4: Evolution of the Noether charge Q for a collision of solutions of type LogA with opposite charge, velocity $v = 0.1$, and phase difference $\alpha = 0$. The Q-balls collide at $t \approx 248$ and partially annihilate charge. After the collision, the resultant Q-balls pass through each other and continue propagating along the axis of symmetry with a larger velocity. Note that a hybrid colormap is used: charge values below $|Q| = 0.1$ are mapped linearly to zero while values above this threshold are mapped logarithmically to the charge maximum.

collision.

Charge annihilation during opposite-charge Q-ball collisions is also observed at larger velocities, though the amount of annihilation is reduced. For example, the amount of charge annihilated is $\sim 15\%$ at $v = 0.3$ and $\sim 7\%$ at $v = 0.5$ for solution LogA. In addition, the collision at these larger velocities is sometimes accompanied by the creation of smaller Q-balls remnants which remain along the axis of symmetry. At the highest velocities, the Q-ball/anti-Q-ball interaction results in very little annihilation (for example, only $\sim 1\%$ of charge is annihilated at $v = 0.9$). There are also fewer Q-ball remnants produced along the axis of symmetry and the fields interfere constructively at the moment of impact (see Figure 3.2).

We have also tested the effects of phase difference on Q-ball/anti-Q-ball collisions, finding that it has a minimal influence on the dynamics. Charge transfer is not observed and the amount of annihilation is not significantly altered compared to the $\alpha = 0$ case.

Thus far, we have only discussed the dynamics associated with solution LogA. Now we turn to solution LogB in Table 3.1. In this case, we find that a generic outcome of the collision is that the field values tend to grow without bound until the evolution becomes singular. This occurs even when the calculation is repeated using additional levels of mesh refinement. As discussed in [1], we can understand this behaviour as a consequence of the logarithmic potential (3.19) being unbounded from below. In particular, for large scalar field values (such as those achieved at the moment of impact), the potential term $V(|\phi|)$ in (3.5) can become negative and may dominate over the other energies in the system. This can lead to the energy density becoming locally negative in the region of large $|\phi|$. At the same time, the energy density in other areas of the domain must grow so that the total integrated energy remains conserved to a positive quantity. This reciprocal process can result in runaway field growth which quickly causes the evolution to become singular. Due to such pathological effects, we do not consider collisions of Q-balls with sizes much larger than that of LogA for $e = 0.1$ in the logarithmic model.

To conclude this section, let us consider the collision dynamics under the polynomial potential (3.20). For this purpose, we will use solution PolyA in Table 3.1 as an illustrative example. Much like what is observed for solution LogA, we find that equal-charge collisions at low velocities are characterized by a merger regime. Notably, the range of velocities for which the Q-balls merge is quite large—in our experiments, merging occurs for $v \lesssim 0.7$. At higher collision velocities, the Q-balls have sufficient kinetic energy to escape the merged state and continue propagating along the axis of symmetry after passing through each other. This is accompanied by a small portion of field content radiating away from the Q-balls after the moment of impact. We have also tested the effects of phase-difference and opposite-charge collisions involving solution PolyA, finding evidence for charge transfer and annihilation similar to what has been previously discussed.

3.4.2 Large Gauge Coupling

We now turn to collisions involving solutions LogC and PolyB from Table 3.1. Unlike the collisions discussed in the previous section, these solutions involve a gauge coupling which is comparable in magnitude to the scalar potential parameters. We therefore expect that electromagnetic effects may have a non-trivial impact on the dynamics.

Once again, we begin by discussing the effect of the initial velocity on the outcome of the collision. Since the Q-balls can now carry a significant amount of electric charge, the long-range Coulomb force can influence the dynamics prior to the moment of impact. If the colliding Q-balls have equal charge, this results in deceleration and a corresponding decrease in their effective velocity before impact. If the colliding Q-balls have opposite charge, the result is acceleration which increases the effective velocity. In order to fully

capture this behaviour, it would be preferable to initialize the boosted Q-balls at $z = \pm\infty$ and let them travel toward each other. However, limitations in computational resources make it unfeasible to initialize the fields at arbitrarily large separation distances, so instead we initialize the Q-balls at $z = \pm 25$ for a given boost. As mentioned previously, we use a multigrid solver to remedy the unphysical constraint violations which may result from a simple superposition of the scalar and electromagnetic fields. In what follows, we will refer to the collision velocity as the velocity at which the Q-balls are initialized at $z = \pm 25$ rather than their effective velocity at the moment of impact.

To proceed with the analysis, we consider the solution LogC in Table 3.1. Unlike what has been discussed in the case of LogA (corresponding to small gauge coupling), the dynamics of solution LogC during equal-charge collisions cannot be cleanly divided into a merger, fragmentation, and elastic regime. At low velocities, we find instead that the Coulomb repulsion is strong enough to completely prevent the scalar fields of each Q-ball from significantly interacting. This causes the Q-balls to decelerate as they approach each other, reach a turning point of vanishing velocity, and then accelerate away in the opposite direction. This behaviour is found to occur for $0 < v \lesssim 0.3$. At velocities $v \gtrsim 0.3$, the Q-balls have sufficient kinetic energy to overcome the Coulomb repulsion and will eventually collide. In these situations, the general outcome is fragmentation of the gauged Q-ball into smaller components. Plotted in Figure 3.5 is the collision of solution LogC at $v = 0.55$. In contrast to the case of small gauge coupling (where no off-axis remnants were observed in the logarithmic model), here we see the formation of a distinct off-axis component which propagates outward before collapsing back onto the axis of symmetry at late times. As noted in [1], these off-axis components represent ring-like structures in three-dimensions which we call "gauged Q-rings". In addition to the ring, a significant portion of the field content also passes through the origin and continues propagating along the axis of symmetry while being highly perturbed.

At the highest velocities, the colliding Q-balls form a clear destructive interference pattern analogous to that seen for the case of small gauge coupling (Figure 3.2). However, after the collision, the fields emerge primarily in the form of Q-rings which propagate away from the axis of symmetry. In addition, a scalar radiation pattern can be observed in the vicinity of the origin. This situation is depicted in Figure 3.6 for solution LogC at $v = 0.9$, and we have found this phenomenon to be present up to a collision velocity of at least $v = 0.95$. This contrasts what is observed for non-gauged Q-balls where high-velocity collisions primarily exhibit free-passage behaviour. Although computational constraints prevent us from exploring boosts much beyond this range (in part due to the extreme field gradients of the boosted Q-balls at these velocities), one can conclude that high-velocity collisions of gauged Q-balls can be considerably less elastic than collisions of their non-gauged counterparts.

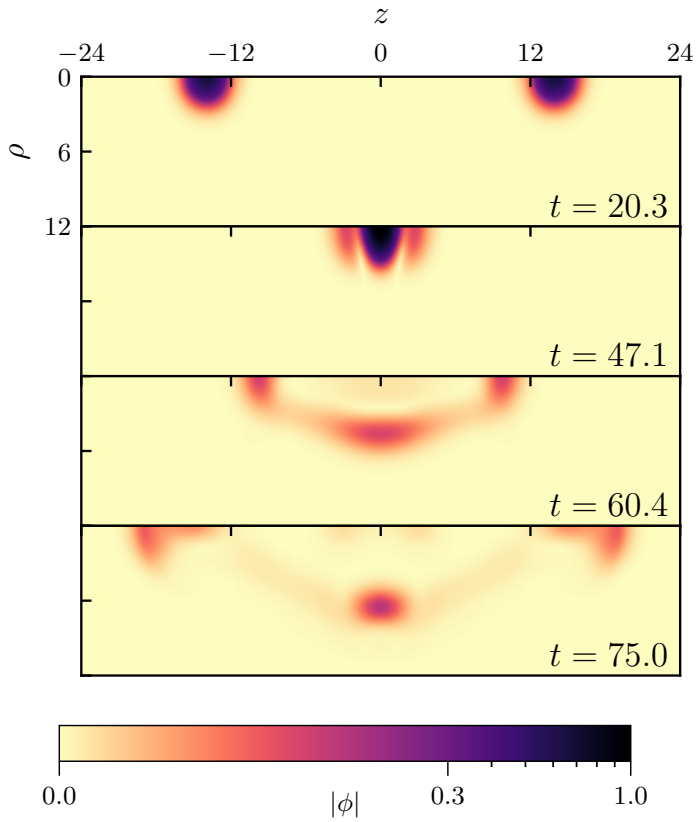

Figure 3.5: Evolution of the scalar field modulus $|\phi|$ for a collision of solutions of type LogC with equal charge, velocity $v = 0.55$, and phase difference $\alpha = 0$. The Q-balls collide at $t \approx 45$. After the collision, the field content contains a mixture of on-axis and off-axis components. Note that a hybrid colormap is used: field values below $|\phi| = 0.3$ are mapped linearly to zero while values above this threshold are mapped logarithmically to the field maximum.

Another challenge is to determine the ultimate fate of the observed Q-rings. While we have made some effort to track the long-term evolution of these structures, the nature of the collision tends to see these remnants propagating away at large velocities and reaching large coordinate distances. While the change of coordinates (3.22)–(3.23) can prevent these components from exiting the domain entirely, they become increasingly compactified as the evolution proceeds. When combined with our use of Kreiss-Oliger dissipation for numerical stability, this effectively decreases the numerical resolution of our simulations and increases the global error (as measured, for instance, by an increase in the total constraint violation). As such, it is difficult to conclusively determine the long-term behaviour of these structures far from the origin, but we make the general observation that they tend to reach a maximum radius before collapsing back inward toward the axis of symmetry. We therefore conjecture

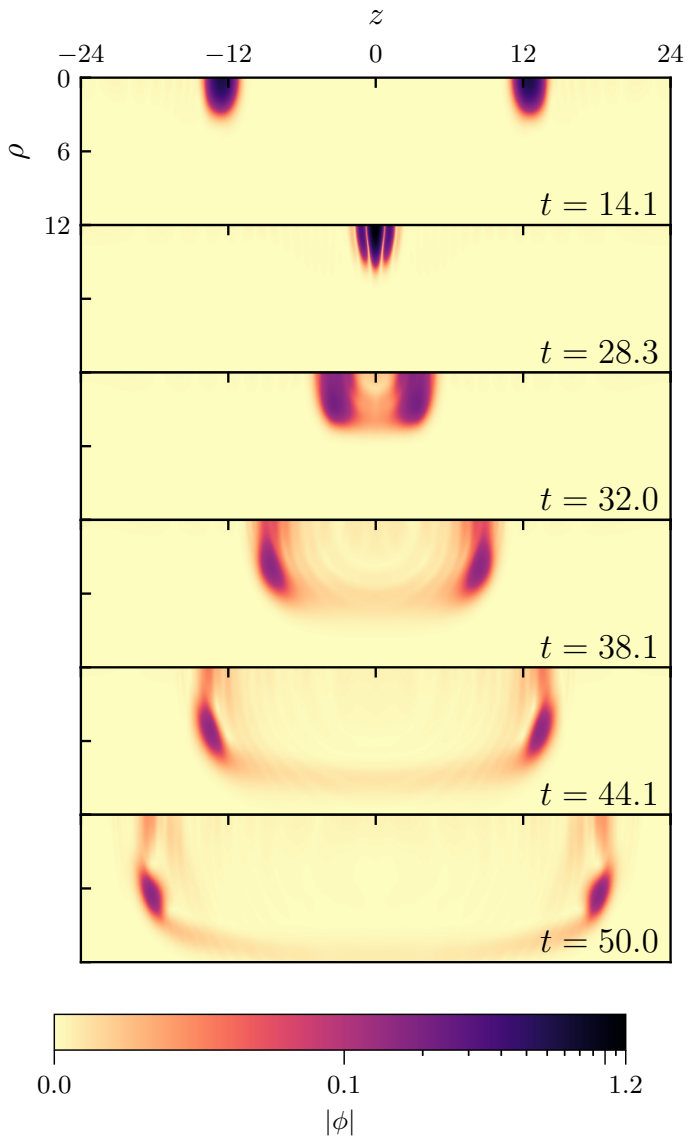

Figure 3.6: Evolution of the scalar field modulus $|\phi|$ for a collision of solutions of type LogC with equal charge, velocity $v = 0.9$, and phase difference $\alpha = 0$. The Q-balls collide at $t \approx 27$. After the collision, a scalar radiation pattern appears (fourth panel) and the field content predominantly takes the form of two Q-rings. Note that a hybrid colormap is used: field values below $|\phi| = 0.1$ are mapped linearly to zero while values above this threshold are mapped logarithmically to the field maximum.

that the gauged Q-rings formed in this way are transient objects (even if the growth of error prevents us from making this statement definitively).

Next, we discuss the effects of phase difference for collisions involving solution LogC. Similar to the case of non-gauged Q-balls, the main effect of altering the phase is to induce charge transfer during the collision. However, the large electric charge associated with LogC produces several novel effects. The first is the absence of charge transfer at small collision velocities $v \lesssim 0.3$. Similar to the case when $\alpha = 0$, the Coulomb repulsion prevents the scalar field of each Q-ball from significantly interacting and so the charge transfer process is never observed. At larger velocities, the Q-balls have sufficient kinetic energy to fully interact and the result is a net transfer of charge in a manner similar to the case of small gauge coupling.

One significant difference between charge transfer in the small- and large-coupling case is the final fate of the Q-balls after the collision. In the case of small gauge coupling, the Q-balls typically propagate away after the collision and retain a coherent shape (though occasionally leaving behind a small remnant Q-ball along the axis of symmetry). However, for the case of solution LogC (for example), the most common outcome is that the Q-balls created during the charge transfer process will quickly break apart into smaller components. This phenomenon is depicted in Figure 3.7 for a collision involving solution LogC with a phase difference of $\alpha = \pi/4$ and velocity $v = 0.5$. Initially, the Q-balls are Lorentz-boosted toward each other and collide at $t \approx 50$. In this process, approximately 35% of the charge is transferred. As the larger Q-ball is formed, it is also highly perturbed, inducing its decay into smaller Q-balls and Q-rings. Depending on the collision parameters, this instability can manifest in a number of different ways such as by breaking apart into smaller Q-balls, into Q-rings, or into a combination of Q-balls and Q-rings. This phenomenon is presumably due to the reduced parameter space of stable solutions which are allowed when the gauge coupling is large [1].

In general, we find that the charge transfer is maximal at intermediate velocities $0.4 \lesssim v \lesssim 0.6$ for solution LogC. At higher velocities, the effect is still observed but the amount of charge transfer is reduced (for example, the collision of solution LogC at $v = 0.7$, $\alpha = \pi/4$ results in $\sim 10\%$ of the charge transferred while the same collision at $v = 0.9$ results in only $\sim 1\%$ transferred). At these higher velocities, the charge transfer manifests through slight asymmetries in the size and trajectory of the Q-ring pattern. An example of this behaviour for solution LogC at $v = 0.7$, $\alpha = \pi/4$ is given in Appendix B.1 (Figure B.3).

We have tested the amount of charge transfer at different phase differences in the range $\alpha \in (0, \pi)$, finding that the transfer is maximal for $\alpha \lesssim \pi/4$. The general phenomena associated with charge transfer is similar for all α tested, though the individual dynamics may differ slightly depending on the collision parameters. However, one exception to the

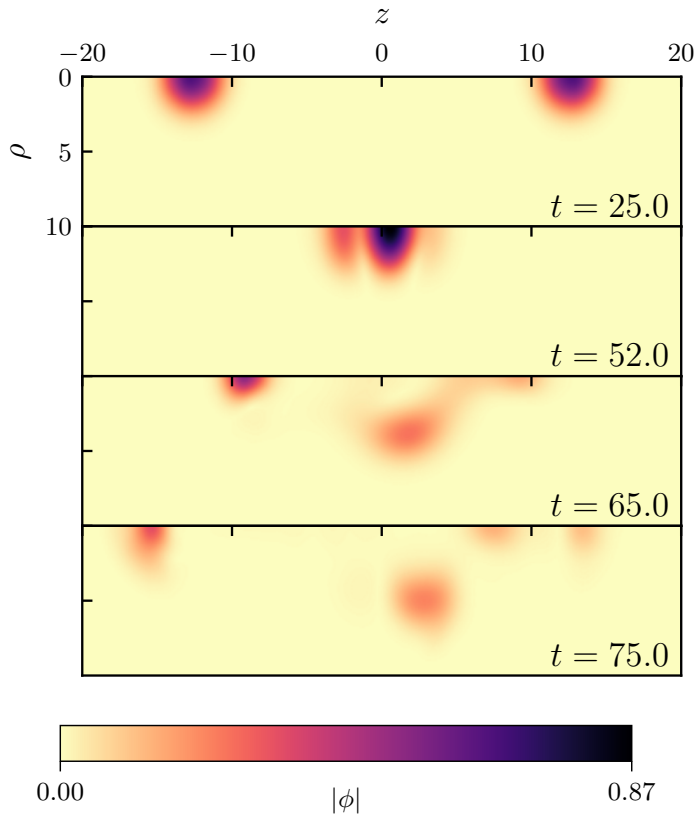

Figure 3.7: Evolution of the scalar field modulus $|\phi|$ for a collision of solutions of type LogC with equal charge, velocity $v = 0.5$, and phase difference $\alpha = \pi/4$. The Q-balls collide at $t \approx 50$ and transfer charge (as can be seen in the second panel). After the collision, the larger Q-ball created in this process quickly breaks apart into smaller components which propagate on and away from the axis of symmetry. The smaller Q-ball travels toward $z = -\infty$ while highly perturbed.

previously-described behaviour is for the case of $\alpha = \pi$. Similar to what has been observed for small gauge coupling, these out-of-phase Q-balls tend to experience a total repulsion at the moment of impact: the fields are momentarily compressed before the Q-balls "bounce back" and form Q-balls or Q-rings in manner symmetric about $z = 0$ (i.e., there is no charge transfer).

Finally, let us discuss Q-ball/anti-Q-ball interactions at large gauge coupling. As was the case for small gauge coupling, the general outcome of such collisions is the annihilation of charge. However, unlike the case for equal-charge collisions, the oppositely-charged Q-balls now experience an attractive Coulomb force which leads to acceleration prior to the moment of impact; this effect is most noticeable at low velocities. This can lead to an increase in the effective collision velocity as discussed previously.

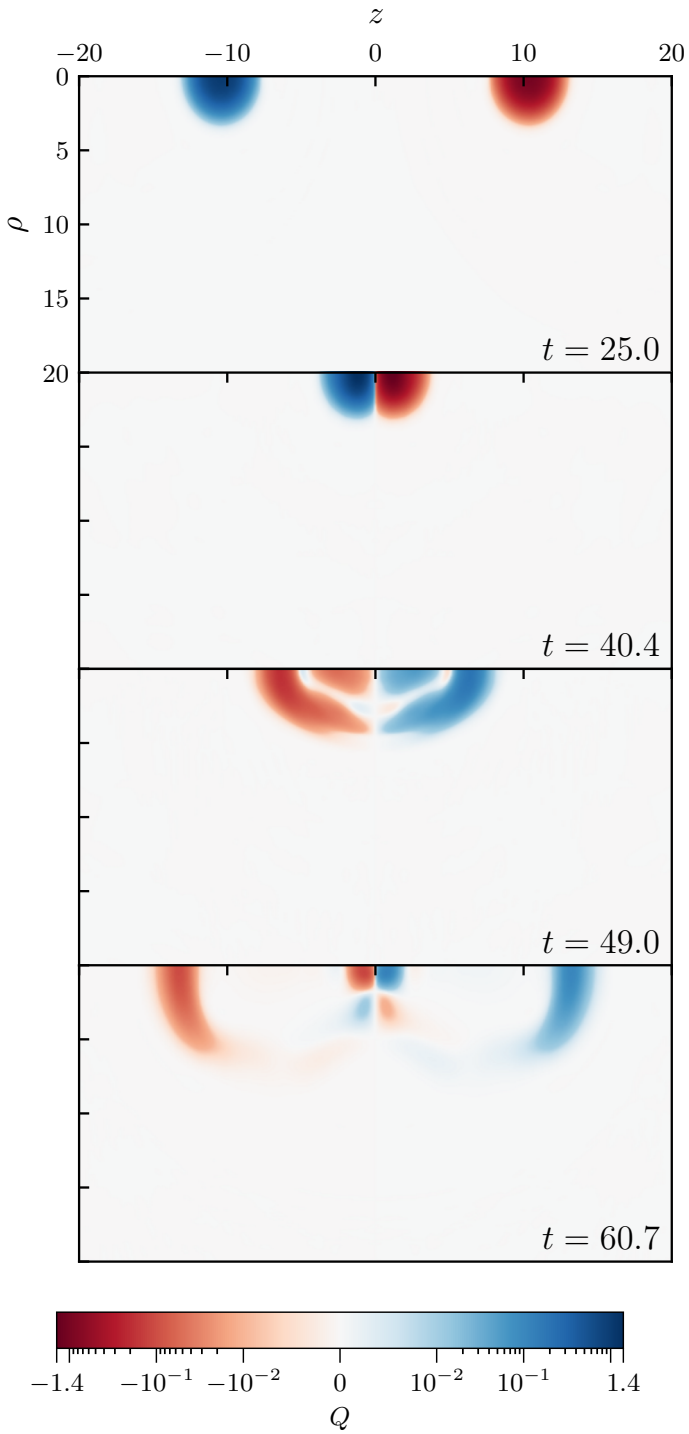

Figure 3.8: Evolution of the Noether charge Q for a collision of solutions of type LogC with opposite charge, velocity $v = 0.6$, and phase difference $\alpha = 0$. The Q-balls collide at $t \approx 40$ and partially annihilate charge. After the collision, a significant portion of the charge content continues propagating along the axis of symmetry while a remnant of mixed positive and negative charge is left behind at the origin. Note that a hybrid colormap is used: charge values below $|Q| = 10^{-2}$ are mapped linearly to zero while values above this threshold are mapped logarithmically to the charge maximum.

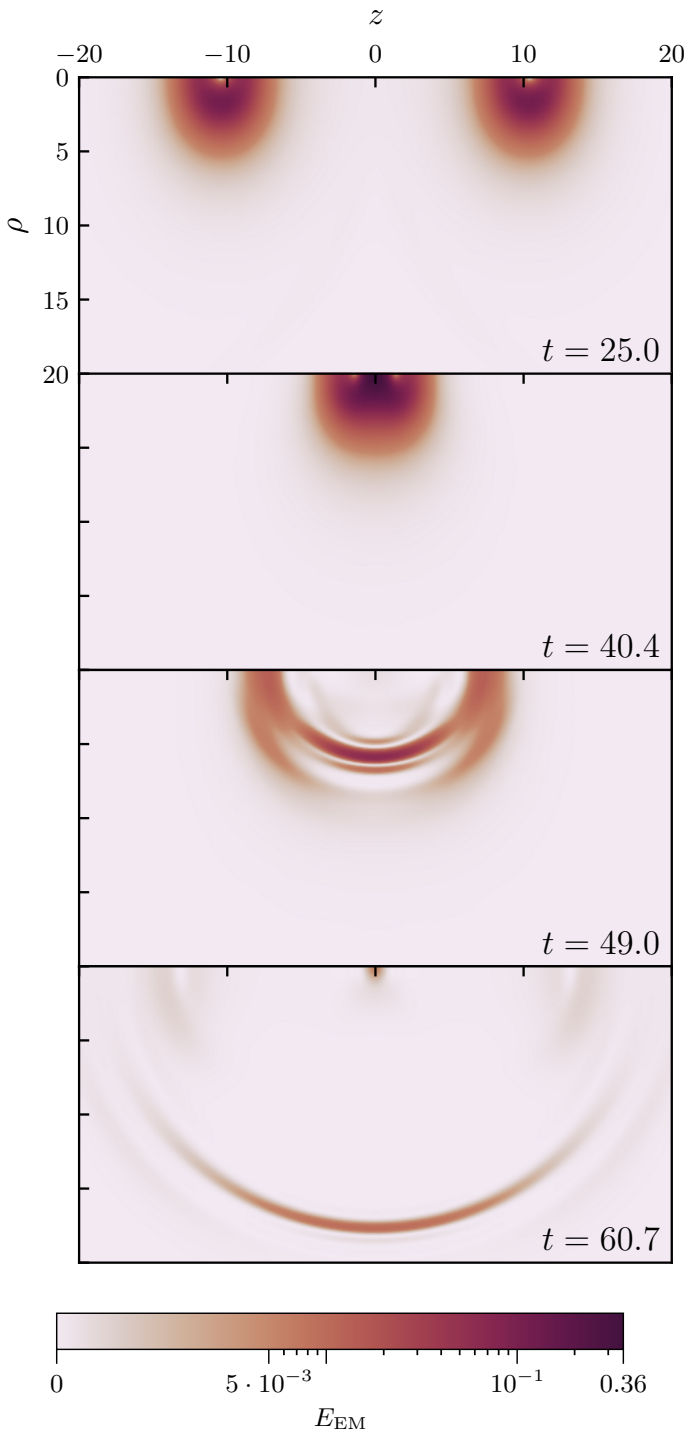

Figure 3.9: Evolution of the electromagnetic field energy E_{EM} for a collision of solutions of type LogC with opposite charge, velocity $v = 0.6$, and phase difference $\alpha = 0$. The Q-balls collide at $t \approx 40$ and partially annihilate charge. After the collision, a quasispherical pulse of electromagnetic energy emanates from the origin. Note that a hybrid colormap is used: energy values below $E_{\mathrm{EM}} = 5 \cdot 10^{-3}$ are mapped linearly to zero while values above this threshold are mapped logarithmically to the energy maximum.

Plotted in Figure 3.8 is the Noether charge Q for a collision involving solution LogC with opposite charge, velocity $v = 0.6$, and phase difference $\alpha = 0$. The Q-balls collide at $t \approx 40$ and partially annihilate. After the collision, a portion of each original Q-ball continues propagating along the axis of symmetry. Additionally, there is a small remnant of mixed charge left behind at the origin which resembles in some ways a charge-swapping Q-ball [47–49]. In this case, approximately $\sim 53\%$ of the initial charge is annihilated during the collision.

The partial charge annihilation which occurs during a Q-ball/anti-Q-ball collision can also result in the production of electromagnetic radiation. To observe this, we compute from (3.5) the energy contained in the electromagnetic field, which can be written as

$$E_{\mathrm{EM}} = \frac{1}{2}\left(|\vec{E}|^2 + |\vec{B}|^2\right), \tag{3.24}$$

where $\vec{E}$ and $\vec{B}$ are constructed from the components of the gauge field A_μ. The electromagnetic field energy for a collision involving solution LogC with opposite charge, velocity $v = 0.6$, and phase difference $\alpha = 0$ (i.e., the same collision as is plotted in Figure 3.8) is plotted in Figure 3.9. Initially, the motion of the charged Q-balls dominates the electromagnetic field energy. At the moment of impact, the Q-balls partially annihilate, converting a fraction of their total energy into a pulse of electromagnetic energy which propagates away from the origin. By comparing Figure 3.8 and Figure 3.9, one can see that the outgoing pulse does not correspond to any significant amount of charge. This fact supports our interpretation of the pulse as representing electromagnetic radiation. We note that we have not made an attempt to precisely quantify the amount of electromagnetic radiation produced in this manner. This is due primarily to the technical challenges associated with integrating the energy over arbitrary subregions of the computational domain during adaptive, highly-parallelized simulations. However, we comment that the size of the electromagnetic pulse is generally proportional to the amount of annihilation that occurs. For illustrative purposes, we also plot in Appendix B.1 (Figure B.4) a representation of the electric and magnetic fields for the collision depicted in Figure 3.8/3.9.

In the general case, we find that the dynamics of Q-ball/anti-Q-ball interactions depend primarily on the collision velocity. At the lowest velocities, the Q-balls tend to pass through each other after partially annihilating, then continue to travel along the axis of symmetry while oscillating weakly. This process is often accompanied by the partial fragmentation of the Q-balls into a small number of Q-balls or Q-rings. At intermediate velocities (e.g., $0.5 \lesssim v \lesssim 0.7$ for solution LogC), the collision becomes more violent: the resulting Q-balls and Q-rings may be greater in number and more strongly oscillatory after the collision. It is also within this intermediate regime that the charge annihilation is found to be maximal.

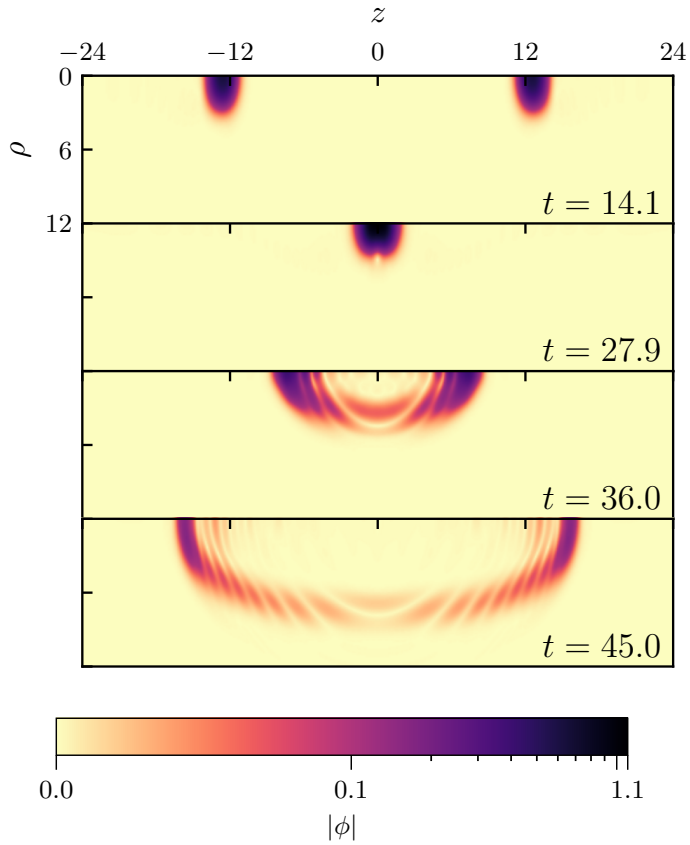

Figure 3.10: Evolution of the scalar field modulus $|\phi|$ for a collision of solutions of type LogC with opposite charge, velocity $v = 0.9$, and phase difference $\alpha = 0$. The Q-balls collide at $t \approx 27$ and interfere constructively. After the collision, the Q-balls continue propagating along the axis of symmetry and carry a long "tail" of scalar matter which exhibits an interference fringe pattern. Note that a hybrid colormap is used: field values below $|\phi| = 0.1$ are mapped linearly to zero while values above this threshold are mapped logarithmically to the field maximum.

At the highest velocities (e.g., $v \gtrsim 0.7$ for solution LogC), the outcome of the collision is once again dominated by two main Q-balls which continue propagating along the axis of symmetry. These Q-balls are accompanied by long "tails" of the scalar field which show a clear interference fringe pattern. This behaviour is shown in Figure 3.10 for solution LogC at $v = 0.9$ with opposite charges and $\alpha = 0$. The amount of charge annihilation is also reduced at high velocities (for example, only $\sim 14\%$ of the charge is annihilated for the collision depicted in Figure 3.10).

We have also studied Q-ball/anti-Q-ball collisions of solution LogC at various phase differences up to $\alpha = \pi$. We find that the phase difference has a minimal effect and the phenomena associated with these collisions resembles closely the $\alpha = 0$ case. This suggests

that the collision dynamics of gauged Q-balls with gauged anti-Q-balls are determined primarily by the collision velocity, in agreement with the case of small gauge coupling. It is interesting to note that we have not observed any cases of total annihilation where the initial Q-balls are converted completely into radiation. Such a phenomena has been observed in previous studies of non-gauged Q-ball collisions for a small range of collision parameters [77]. While total annihilation may still be possible for the gauged case, our analysis suggests that it might likewise occur for only a narrow range of parameters.

We conclude this section by returning to collisions under the polynomial model (3.20). For this purpose, we focus on solution PolyB in Table 3.1. This solution is notable in that it corresponds to a value of the gauge coupling e which is near the maximum allowed for the polynomial potential, $e_{max} \approx 0.182$ [96]. Considering first the equal-charge collisions of solution PolyB, we find once again that the Q-balls tend to repel at low velocities. This is in agreement with what has been discussed previously for the logarithmic model. However, for intermediate velocities (e.g., $0.35 \lesssim v \lesssim 0.6$), we observe that the colliding Q-balls can merge into a single Q-ball which remains at the origin. This is accompanied by the emission of charge as the merged Q-ball settles down into a near-stationary configuration. At slightly higher velocities (e.g., $0.65 \lesssim v \lesssim 0.85$), the Q-balls do not form a single stable Q-ball; instead, the fields dissipate shortly after the moment of impact in the form of outgoing waves. This situation is depicted in Figure 3.11. For collision velocities $v \gtrsim 0.85$, we find that the majority of the field content emerges along the axis of symmetry after the collision. However, the initial Q-balls are still difficult to distinguish in the aftermath as the field magnitudes are greatly reduced and are also elongated in the radial direction. This is accompanied by a spherical radiation pattern emanating from the origin. An example of this scenario is depicted in Appendix B.1 (Figure B.5). This lies in contrast to what is observed for the logarithmic model where the dominant field components after the collision take the form of gauged Q-rings (cf. Figure 3.6). However, regardless of the final structure, we conclude that the equal-charge collisions of solution PolyB can be considerably inelastic even at collision velocities which are near-luminal.

Turning next to collisions of solution PolyB with a relative phase difference, we find that charge transfer is once again the dominant outcome (as long as the kinetic energy is sufficient to overcome the Coulomb repulsion). Similar to what is observed for solution LogC, the Q-balls created in this manner are often unstable and may quickly fragment after the collision. In some cases, we even find that the instability can manifest via near-complete dispersal of the fields so that the end result of the collision is just one remaining gauged Q-ball. An example of this behaviour for solution PolyB is given in Appendix B.1 (Figure B.6). At the highest velocities and for large phase differences, we find that the amount of charge transfer is once again reduced. For collisions of opposite charges, the

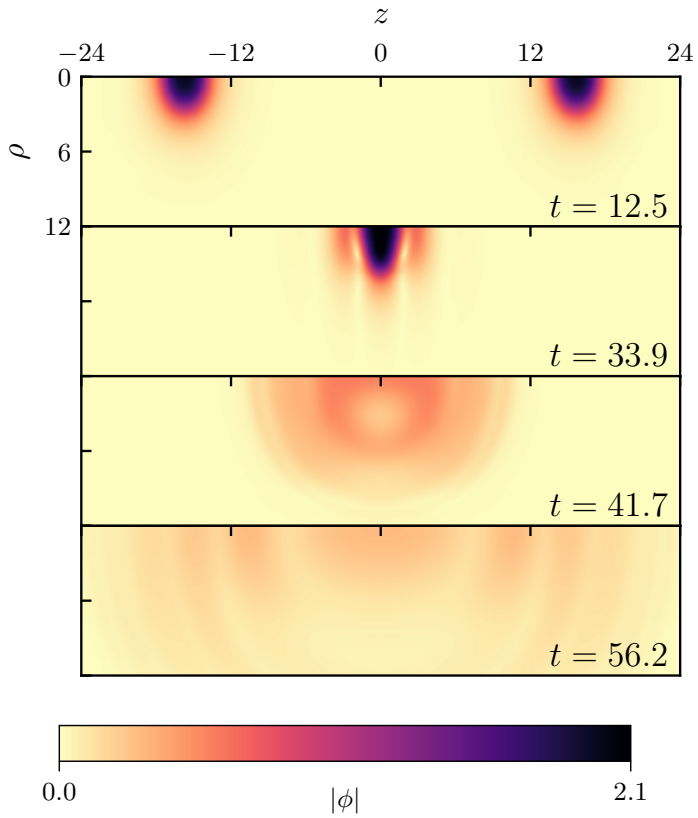

Figure 3.11: Evolution of the scalar field modulus $|\phi|$ for a collision of solutions of type PolyB with equal charge, velocity $v = 0.75$, and phase difference $\alpha = 0$. The Q-balls collide at $t \approx 33$ and form a destructive interference pattern. After the collision, it becomes difficult to distinguish any component of the field which clearly resembles a Q-ball. Instead, the field content appears to dissipate in the form of near-spherical waves which emanate from the origin.

dynamics are generally independent of the relative phase with the main result being the net annihilation of charge which is maximal at low collision velocities. In contrast to what is observed for solution LogC (cf. Figure 3.8), we do not observe the formation of any smaller Q-balls during opposite-charge collisions involving solution PolyB. Instead, the Q-balls tend to continue propagating uniformly along the axis of symmetry, though often being strongly perturbed by the annihilation process.

3.5 Conclusion

In this work, we have performed high-resolution numerical simulations to study head-on collisions of $U(1)$ gauged Q-balls. Focusing on the relativistic regime, we have studied the effects of various parameters (such as collision velocity, relative phase, relative charge, and

electromagnetic coupling strength) on the outcome of the collision. Our simulations suggest that the outcome can depend heavily on these parameters, resulting in dynamics which can be quite distinct from those observed during collisions of ordinary (non-gauged) Q-balls.

We first examined the dynamics of gauged Q-balls with small gauge coupling. Here it was found that the dynamics for equal-charge collisions can generally be divided into three regimes (the "merger", "fragmentation", and "elastic" regimes) depending on the collision velocity. We also studied the effect of phase-difference and opposite-charge collisions, finding evidence for charge transfer and annihilation, respectively. These findings are consistent with what has been previously reported for ordinary (non-gauged) Q-balls. Overall, these results suggest that gauged Q-balls with small gauge coupling can behave like non-gauged Q-balls during head-on collisions.

Turning to the case of large gauge coupling, we find that collisions of gauged Q-balls can lead to distinct dynamical behaviour due to the influence of the electromagnetic field. For equal-charge collisions, the Coulomb force can cause a repulsion which prevents the scalar field of each Q-ball from reaching a state of significant interaction. This occurs at low collision velocities. At higher velocities, we find that collisions are rarely an elastic process; instead, the main outcome is often a fragmentation of the colliding Q-balls into several smaller gauged Q-balls or Q-rings. This effect persists even at collision velocities very close to the speed of light. Studying the effect of phase difference on the collision outcome, we observe evidence for charge transfer. However, the gauged Q-balls created during this process are often unstable and tend to quickly break apart into smaller components. For the case of opposite-charge collisions, we find partial annihilation of the gauged Q-balls to be a generic outcome which can lead to the production of an electromagnetic radiation pulse. Having studied these behaviours using both polynomial and logarithmic scalar field potentials, we find that the collision dynamics can differ slightly depending on the choice of potential. However, we conclude that the main phenomena associated with gauged Q-ball collisions (such as charge transfer, annihilation, and the inelasticity of the collisions) are generally independent of the specifics of the model.

Since the present study has been limited to axisymmetry, it is interesting to ask how the dynamics may change in fully three-dimensional simulations. This question will be addressed in a future publication. It would also be interesting to consider how quantum effects may influence the dynamics of gauged Q-balls similar to what has recently been done for non-gauged Q-balls [143]. Finally, we comment that the results of this work could be extended by considering more general scenarios in axisymmetry (such as collisions between gauged Q-balls with unequal $|Q|$) or by studying in further detail the electromagnetic signal created during the collisions. These scenarios may be relevant for cosmological applications of gauged Q-balls [106–109].

Chapter 4

Dynamics of $U(1)$ Gauged Q-balls in Three Spatial Dimensions

4.1 Introduction

Q-balls are non-topological solitons that arise in scalar field theories admitting a $U(1)$ symmetry and a non-linear attractive potential[1]. First described by Coleman [27, 28], they have garnered significant attention in recent years due to their potential relevance to early-Universe cosmology (where they may act as dark matter candidates [34, 35]) and in condensed matter experiments (where they serve as relativistic analogues to various condensed matter solitons [68–70]). Q-balls also hold considerable theoretical interest as smooth, classical field configurations which constitute a rudimentary model of a particle.

An extension to the basic Q-ball theory can be made through the introduction of a $U(1)$ gauge field. This gives rise to so-called *gauged Q-balls* which couple to the electromagnetic field and carry an electric charge [84]. While gauged Q-balls share some similarities with ordinary (non-gauged) Q-balls, the additional electromagnetic coupling can also lead to several distinct features. For example, it may place restrictions on their allowable size and charge [87, 94], change their dynamical behaviour [1, 2], and even give rise to new types of solutions in the model (such as shell-shaped structures [86–88]). It has also been speculated that the repulsive Coulomb force arising from a gauged Q-ball might serve as a destabilizing mechanism which eventually destroys it [95]. This is an important issue because one should expect gauged Q-balls to be robust against generic perturbations in order to be considered viable physical objects. However, the stability analysis of these objects is challenging because the application of standard methods for establishing classical stability (such as linear perturbation analyses or known stability theorems) are hindered by

[1]The content of this chapter has previously been published in [3].

the presence of the $U(1)$ gauge field. In particular, it is known that gauged Q-balls can be classically stable against spherically-symmetric and axially-symmetric perturbations [1, 95], but the case of general three-dimensional perturbations has yet to be explored.

In the present work, we address this problem of gauged Q-ball stability by performing fully non-linear numerical evolutions of the equations of motion in three spatial dimensions. For gauged Q-balls in both logarithmic and polynomial scalar field models, we find numerical evidence for solutions which are classically stable against generic three-dimensional perturbations over long dynamical timescales. In these cases, we find that the stable gauged Q-balls respond to the perturbations by oscillating continuously or weakly radiating before evolving toward a state that is close to the initial configuration. In other cases, we also observe examples of unstable configurations which are eventually destroyed by the perturbations (for instance, by fragmentation into smaller gauged Q-balls). Our results are found to be generally consistent with previous numerical work on gauged Q-ball stability under spherical and axial symmetry assumptions [1, 95]. Motivated by the very recent analysis of [92], we also investigate the case of the polynomial scalar field potential at small gauge coupling and find a new result for the instability transition point in comparison to what was reported in [1].

Another question we explore relates to the behaviour of gauged Q-balls during relativistic collisions. In [2], it was shown that gauged Q-balls can exhibit a range of remarkable interaction phenomena such as mergers, fragmentation, charge transfer, charge annihilation, Q-ring formation, and radiation production. However, these results have also been limited by the assumption of axial symmetry. It is worthwhile to ask whether any of these phenomena are peculiar to axial symmetry or whether they also extend to a more realistic three-dimensional setting. Moreover, it is interesting to ask how the dynamics may change during gauged Q-ball collisions with non-zero impact parameter (a scenario which was not accessible under previous symmetry assumptions). In the present work, we address these questions by considering both head-on and off-axis collisions of gauged Q-balls in three spatial dimensions.

This paper is organized as follows: in Section 4.2, we present the basic equations of the theory. In Section 4.3, we describe our numerical implementation of the evolution equations along with our initial data procedure. In Section 4.4, we present our main numerical results. In Section 4.5, we provide some concluding remarks.

Throughout this work, we employ units where $c = \hbar = 1$. For brevity, we interchangeably use the terms "Q-ball" and "gauged Q-ball" when the distinction between the gauged and non-gauged solutions is made obvious by context.

4.2 Equations of Motion

The theory of $U(1)$ gauged Q-balls can be described by the Lagrangian density

$$\mathcal{L} = -\left(D_\mu \phi\right)^* D^\mu \phi - V\left(|\phi|\right) - \frac{1}{4} F_{\mu\nu} F^{\mu\nu}. \tag{4.1}$$

Here, ϕ is the complex scalar field, A_μ is the $U(1)$ gauge field, $D_\mu = \nabla_\mu - ieA_\mu$ is the gauge covariant derivative with coupling constant e, $F_{\mu\nu} = \partial_\mu A_\nu - \partial_\nu A_\mu$ is the electromagnetic field tensor, and $V(|\phi|)$ is the scalar potential. The equations of motion for the theory take the form

$$D_\mu D^\mu \phi - \frac{\partial}{\partial \phi^*} V(|\phi|) = 0, \tag{4.2}$$

$$\nabla_\mu F^{\mu\nu} + e j^\nu = 0, \tag{4.3}$$

where

$$j^\nu = -i(\phi^* D^\nu \phi - \phi (D^\nu \phi)^*) \tag{4.4}$$

is the Noether current density. Consistent with previous work [1, 2], we consider two forms for the scalar field potential:

$$V_{\log}(|\phi|) = -\mu^2 |\phi|^2 \ln(\beta^2 |\phi|^2), \tag{4.5}$$

$$V_6(|\phi|) = m^2 |\phi|^2 - \frac{k}{2}|\phi|^4 + \frac{h}{3}|\phi|^6, \tag{4.6}$$

where μ, β, m, k, and h are real, positive parameters. Additionally, we employ the Minkowski line element,

$$ds^2 = -dt^2 + dx^2 + dy^2 + dz^2, \tag{4.7}$$

and fix the gauge with the Lorenz condition,

$$\nabla_\mu A^\mu = 0, \tag{4.8}$$

in order to write the equations of motion (4.2)–(4.3) in a form which is suitable for numerical evolution (see Appendix C.1). In addition to these equations, solutions in the theory (4.1) must also satisfy the constraints

$$\nabla_i E^i = e j^0, \tag{4.9}$$

$$\nabla_i B^i = 0. \tag{4.10}$$

Here, E^i and B^i represent the components of the electric and magnetic field vectors, respectively, which are determined from the electromagnetic field tensor, $F_{\mu\nu}$. Solutions in the theory (4.1) are expected to satisfy (4.9)–(4.10) everywhere in the solution domain. The amount by which these constraints are violated therefore provides a relative measure of the error in the numerical evolution; this issue will be discussed in further detail below.

4.3 Numerical Implementation

As stated previously, we use a numerical framework to study the dynamics of the model in three spatial dimensions. Here we provide the details of this approach.

4.3.1 Initial Data

In order to generate initial data which describes gauged Q-balls, we begin by making a spherically-symmetric ansatz for the fields,

$$\phi(t,\vec{x}) = f(r)e^{i\omega t}, \tag{4.11}$$

$$A_0(t,\vec{x}) = A_0(r), \tag{4.12}$$

$$A_i(t,\vec{x}) = 0. \tag{4.13}$$

With this ansatz, the equations of motion reduce to a system of two coupled differential equations,

$$f''(r) + \frac{2}{r}f'(r) + f(r)g(r)^2 - \frac{1}{2}\frac{d}{df}V(f) = 0, \tag{4.14}$$

$$A_0''(r) + \frac{2}{r}A_0'(r) + 2ef(r)^2 g(r) = 0, \tag{4.15}$$

where we have defined $g(r) = \omega - eA_0(r)$. To find gauged Q-ball solutions which are smooth with finite energy, we impose the boundary conditions:

$$\frac{df}{dr}(0) = 0, \qquad \lim_{r\to\infty} f(r) = 0, \tag{4.16}$$

$$\frac{dA_0}{dr}(0) = 0, \qquad \lim_{r\to\infty} A_0(r) = 0. \tag{4.17}$$

Together, the differential system (4.14)–(4.17) is akin to an eigenvalue problem for the parameter ω. As described in [1], we use a numerical shooting technique to solve this system for $f(r)$ and $A_0(r)$ to a good approximation. The resultant solutions provide the spherically-symmetric profile functions for gauged Q-balls at a given value of ω.

To initialize the fields in three dimensions, it is necessary to compute the values of the spherical functions $f(r)$ and $A_0(r)$ at arbitrary points in space using the coordinate system

defined by (4.7). For this purpose, we apply fourth-order Neville interpolation [23] to the numerical profiles of $f(r)$ and $A_0(r)$ and set the values of ϕ and A_μ using the ansatz (4.11)–(4.13). With this procedure, it is straightforward to construct the initial data for a single stationary gauged Q-ball which is centered at the origin. This is the form of initial data we use to study gauged Q-ball stability.

When studying relativistic collisions of gauged Q-balls, the previously-described procedure must be adjusted. The main difference comes from the need to initialize a binary configuration of Q-balls which are Lorentz-boosted at a relativistic velocity v (where $v = 1$ is the speed of light in our units). In this case, an initial displacement from the origin is chosen for each Q-ball and the Neville interpolation procedure is performed separately about the center point for each soliton. Each gauged Q-ball is then given a Lorentz boost in a direction parallel to the z-axis and toward the origin. Finally, the fields of each gauged Q-ball are superposed to complete the initial data specification.

As discussed in [2], some care must be taken when implementing the above procedure for binary gauged Q-balls. In particular, if the Q-balls in the binary are not sufficiently separated at the initial time, the long-range behaviour of the gauge field can lead to unphysical violations of the constraint equation (4.9). These arise due to the influence of the gauge field from one Q-ball on the scalar field of the other. In an ideal case, one could avoid this problem by picking a sufficiently large separation distance so that these influences are negligible. However, this proves to be impractical for our numerical simulations because large initial separation distances incur a greater computational cost. Instead, we address this problem by implementing an FAS multigrid algorithm with fourth-order defect correction [113] to re-solve the constraint equation (4.9) at the initial time for general superpositions of gauged Q-balls (see also [144]). This provides an order-of-magnitude reduction in the constraint violation associated with our binary initial data.

4.3.2 Diagnostic Quantities

Here we describe a number of diagnostic quantities which can be used to assess the numerical results. Foremost among these are the total energy E and total Noether charge Q which are conserved in the continuum limit. For the theory described by (4.1), the energy-momentum tensor takes the form

$$\begin{aligned} T_{\mu\nu} = & F_{\mu\alpha}F_{\nu\beta}g^{\beta\alpha} - \frac{1}{4}g_{\mu\nu}F_{\alpha\beta}F^{\alpha\beta} \\ & + D_\mu\phi(D_\nu\phi)^* + D_\nu\phi(D_\mu\phi)^* \\ & - g_{\mu\nu}(D_\alpha\phi(D^\alpha\phi)^* + V(|\phi|)). \end{aligned} \tag{4.18}$$

Using (4.18), we define the total energy contained in the system as $E = \int T_{00}\, d^3x$. Likewise, the total Noether charge can be computed from the current density (4.4) as $Q = \int j^0\, d^3x$. In all simulations discussed below, these quantities are monitored to ensure that they do not deviate from their initial values by more than $O(1\%)$.

In order to investigate the dynamical stability of gauged Q-balls, it is necessary to introduce small perturbations into the system. For this purpose, we incorporate an auxiliary scalar field into the theory (4.1) which serves as a diagnostic tool. The modified Lagrangian density of the theory takes the following form:

$$\begin{aligned}\mathcal{L} = &- (D_\mu \phi)^* D^\mu \phi - V(|\phi|) - \frac{1}{4} F_{\mu\nu} F^{\mu\nu} \\ &- \partial_\mu \chi \partial^\mu \chi - U(|\phi|, \chi).\end{aligned} \tag{4.19}$$

Here, χ is a massless real scalar field which couples to the complex Q-ball field ϕ via the interaction potential $U(|\phi|, \chi)$. As discussed in [1], the auxiliary field χ can act as an external perturbing agent if the initial data and interaction potential $U(|\phi|, \chi)$ are chosen so that χ exerts a small, temporary influence on ϕ. In particular, if χ is chosen to take the form of an aspherical pulse which implodes onto a stationary gauged Q-ball at the origin, the interaction governed by $U(|\phi|, \chi)$ is expected to excite all underlying modes of the configuration. If the configuration is stable, we expect the oscillations of these modes to remain bounded and the Q-ball to stay intact. However, if the configuration is unstable, we expect that one or more modes will grow exponentially, eventually bringing about the destruction of the gauged Q-ball in some manner (for example, via fragmentation or dispersal of the fields). In this way, we can probe the stability properties of gauged Q-balls by observing their interaction with the auxiliary field χ.

Here we choose the scalar interaction potential in (4.19) to take the form

$$U(|\phi|, \chi) = \gamma |\phi|^2 \chi^2 \tag{4.20}$$

and initialize the perturbing field according to

$$\chi(0, x, y, z) = A \exp\left[- \left(\frac{\Delta - r_0}{\delta} \right)^2 \right] \tag{4.21}$$

where

$$\Delta = \sqrt{\frac{(x - x_0)^2}{a_x^2} + \frac{(y - y_0)^2}{a_y^2} + \frac{(z - z_0)^2}{a_z^2}}. \tag{4.22}$$

In the above, A, δ, r_0, a_x, a_y, a_z, x_0, y_0 and z_0 are real, positive parameters which determine the initial profile of χ. In particular, if r_0 is large, then (4.21) resembles a shell-like con-

centration of the field which approximately vanishes in the vicinity of the Q-ball at $t = 0$. This shell can be made to implode upon the origin at some time $t > 0$ by setting

$$\partial_t \chi(0, x, y, z) = \frac{\chi + x\partial_x \chi + y\partial_y \chi + z\partial_z \chi}{\sqrt{x^2 + y^2 + z^2}}. \tag{4.23}$$

The form of the interaction potential (4.20) means that, after implosion, χ will propagate out toward infinity at late times, leaving no significant remnant near the origin. Thus, χ represents a time-dependent perturbation whose influence on the Q-ball field ϕ can be directly controlled via the parameter A in (4.21) (or similarly, via γ in (4.20)).

While the auxiliary field χ serves as a convenient diagnostic tool for our purposes, we emphasize that it is by no means the only form of perturbation which exists in the system. In particular, our finite-difference approach for solving the equations of motion (to be described below) inherently introduces small-scale errors into our simulations which also act as perturbations. However, given the nature of the finite-difference scheme we use, as well as the typical numerical resolution we adopt, this type of perturbation is typically very small; this can make it difficult to definitively assess the stability of the Q-ball unless the simulation timescale is very long. By introducing the field χ in (4.19), we gain an additional level of control over the perturbative dynamics of the system beyond what is possible in the original (unmodified) theory (4.1).

4.3.3 Evolution Scheme

To solve the equations of motion of the system in three spatial dimensions, we use a fourth-order finite-difference scheme implemented using the Finite Difference Toolkit (FD) [121]. A fourth-order classic Runge-Kutta method [23] is used for the time integration. Additionally, a sixth-order Kreiss-Oliger dissipation operator is added to the equations of motion in order to reduce deleterious effects of grid-scale solution components arising from the finite-difference computations. We also utilize a modified Berger-Oliger adaptive mesh refinement (AMR) algorithm [118] in order to tailor the numerical resolution of our simulations according to local truncation error estimates. We discuss the validation of our numerical code in Appendix C.2.

As in [2], we find it advantageous when solving the equations of motion to invoke a change of coordinates $x^\mu = (t, x, y, z) \to x^{\mu'} = (t, X, Y, Z)$ according to

$$x = d\exp(cX) - d\exp(-cX), \tag{4.24}$$

$$y = d\exp(cY) - d\exp(-cY), \tag{4.25}$$

$$z = d\exp(cZ) - d\exp(-cZ), \tag{4.26}$$

where c and d are positive, real parameters. With the transformations defined by (4.24)–(4.26), the simulation domain can be approximately compactified at large coordinate values while retaining coordinates near the origin that are close to their untransformed values. This transformation is advantageous for two reasons. First, it allows us to observe the dynamics in scenarios where appreciable field content may propagate swiftly away from the origin and reach large coordinate distances. Second, it greatly simplifies the process of setting appropriate boundary conditions for the problem. In particular, our fourth-order finite-difference scheme requires a spatial stencil which spans at least five grid points in each spatial dimension (or seven grid points when applying sixth-order Kreiss-Oliger dissipation). While this is straightforward to implement in the interior of the domain, the boundary regions (and surrounding area) require a meticulous treatment in terms of fourth-order backward and forward difference operators. However, with the coordinate transformations defined by (4.24)–(4.26), the simulation domain can be made large enough so that Dirichlet conditions can be imposed as a reasonable approximation at the physical boundaries and at boundary-adjacent points. This greatly reduces the complexity of the implementation.

For all results presented in this work, we set a base-level grid resolution of 129^3 points and utilize up to 8 levels of additional mesh refinement with a refinement ratio of 2:1. We select a Courant factor of $\lambda = dt/\{dX, dY, dZ\} = 0.25$ and choose $c = 0.05$, $d = 10$ in the transformations (4.24)–(4.26). When investigating the stability of gauged Q-balls, we use a domain $-150 \leq X, Y, Z \leq 150$, corresponding to a physical domain given by approximately $-18000 \leq x, y, z \leq 18000$. When investigating relativistic collisions of gauged Q-balls, we use a domain with $-75 \leq X, Y, Z \leq 75$, corresponding to approximately $-425 \leq x, y, z \leq 425$. In both cases, the Dirichlet boundary conditions imposed during the evolution are sampled from the grid function values at the initial time. We have also verified that these boundary conditions do not introduce any significant errors which propagate inward and pollute the interior solution.

4.4 Numerical Results

Here we present results from our numerical evolutions of the gauged Q-ball system. As stated above, we consider two forms for the scalar potential (logarithmic (4.5) and polynomial (4.6)) and set $\mu = \beta = m = k = 1$ and $h = 0.2$ following previous work [1, 2]. Due to the large computational cost associated with fully three-dimensional evolutions, we restrict our analysis to a few values of gauge couplings e. In particular, for the logarithmic potential $V_{\log}(|\phi|)$ in (4.5), we examine $e = 1.1$, while for the polynomial potential $V_6(|\phi|)$ in (4.6), we examine $e = 0.17$ (which is near the maximum allowable value for our choice of the potential parameters [96]) and $e = 0.02$. To illustrate some of the salient dynamics in these models, we will use three specific gauged Q-ball configurations which are listed in

Configuration	Potential	e	$\lvert\phi(0,0,0)\rvert$	$A_0(0,0,0)$	ω	E	$\lvert Q\rvert$	Stable?
A	Logarithmic	1.1	0.6461	1.383	2.522	52.08	22.37	Yes
B	Logarithmic	1.1	2.448×10^{-13}	0.9803	3.078	260.3	92.76	No
C	Polynomial	0.17	1.973	2.515	0.9976	405.1	387.5	Yes

Table 4.1: Table of representative gauged Q-ball configurations which are used to illustrate the dynamics in the theory (4.1). The configurations A and B correspond to the logarithmic potential (4.5). The configuration C corresponds to the polynomial potential (4.6). From left to right, the remaining columns give the value of the electromagnetic coupling constant e, the initial central value of the scalar field $|\phi(0,0,0)|$, the initial central value of the gauge field $A_0(0,0,0)$, the Q-ball oscillation frequency ω, the total energy E of the solution (when stationary), and the total Noether charge $|Q|$ of the solution. The final column indicates the stability of the configuration as determined through our numerical simulations.

Table 4.1.

While all calculations in this section are performed using the compactified coordinates defined by (4.24)–(4.26), we will hereafter present all results using the original coordinates defined by the line element (4.7). This is done mainly for ease of interpretation.

4.4.1 Stability

For the purposes of this work, we define the stability of a gauged Q-ball configuration in terms of its response to small dynamical perturbations. Specifically, we consider a configuration to be stable if physical quantities influenced by the perturbation—such as the field maxima—remain bounded in time (aside from small numerical drifts which may arise due to the long timescales used in our simulations). Unstable configurations, on the other hand, are those for which some component of the fields may grow continuously in response to the perturbation until the initial Q-ball is destroyed.

As mentioned previously, we use an auxiliary real massless scalar field χ as an external perturbing agent. The field χ takes the form of an imploding pulse which is slightly aspherical and off-center from the origin at the initial time. This choice ensures that the gauged Q-ball (which is initially centered at the origin) will experience a generic three-dimensional perturbation which is likely to excite all underlying modes of the solution. After the field χ explodes through the origin, the subsequent behaviour of the Q-ball can be observed. To make an assessment of stability, we compute the maximal value of $|\phi|$ over the entire numerical domain. If this maximal value (which is presumed to be attained near the Q-ball center) oscillates continuously near the initial value in response to the perturbation, we conclude that the configuration is stable. We also visualize the fields in 3D to observe whether there is any change in shape or behaviour. If the field maximum or shape of the Q-ball significantly and permanently deviates from the initial configuration (such as by breaking apart into smaller structures), we conclude that the configuration is unstable.

To begin the analysis, we use the shooting procedure described in Section 4.3.1 to obtain gauged Q-ball solutions for the potentials (4.5) and (4.6). The space of solutions for the logarithmic potential (4.5) with $e = 1.1$ is depicted in Figure 4.1. In the figure, each dot represents one distinct gauged Q-ball configuration which is found via the shooting procedure. For each of these configurations, we evolve the system twice to assess its stability. First, the evolution is performed with the auxiliary field χ acting as an perturbing agent; for this we set $\gamma = 0.1$ in (4.20) and $A = 0.1$ in (4.21) so that the field has a material impact on the evolution of the Q-ball field ϕ. Second, we perform the same evolution with $\gamma = 0$ so that χ and ϕ do not interact. In this case, the gauged Q-ball is subject only to the small perturbations arising from the truncation error of the scheme or other numerical sources (such as those associated with the AMR algorithm [145]). For both of these evolutions, we

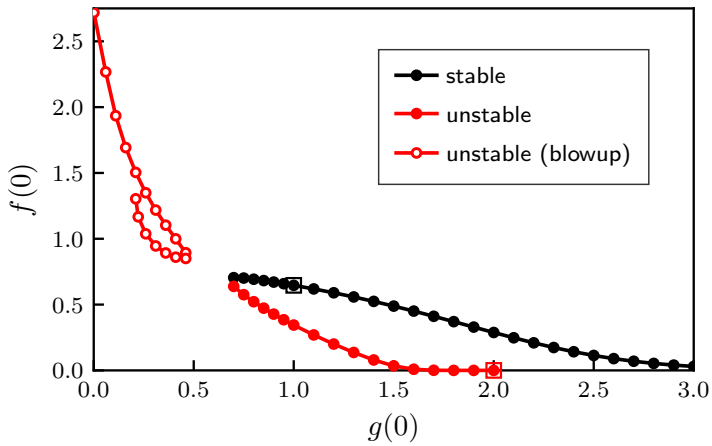

Figure 4.1: Shooting results and regions of stability and instability for gauged Q-balls in the logarithmic model (4.5) with $e = 1.1$. Plotted is the Q-ball's central scalar field value $f(0)$ versus the numerical shooting parameter $g(0) = \omega - eA_0(0)$. The black solid circles represent configurations which are found to be stable with respect to generic three-dimensional perturbations. The red solid and open circles represent configurations which are found to be unstable with respect to these perturbations. The open squares represent configurations A and B from Table 4.1.

evolve the system until at least $t = 1200$ which typically corresponds to $O(100)$ internal oscillations of the Q-ball. The outcome of the evolution is then classified depending on whether an instability is observed. In Figure 4.1, the stable configurations are marked by black solid circles while the unstable configurations are marked by red solid and open circles.

By looking at Figure 4.1, one can observe several interesting features. The first is the existence of both stable and unstable branches in the space of gauged Q-ball solutions. By direct comparison with previous work, one can see that the regions of stability and instability correspond exactly with what has been found for axisymmetric perturbations (cf. Figure 3 of [1]). This suggests that three-dimensional perturbations do not excite any additional unstable modes for gauged Q-balls with $e = 1.1$ in the logarithmic model. The appearance of a stable branch also addresses the general question of gauged Q-ball stability which was originally posed in [95] (namely, whether the Coulomb force will eventually destroy any gauged Q-ball when symmetry assumptions are relaxed). This reaffirms the possibility of gauged Q-balls as viable physical objects in realistic three-dimensional settings.

Let us discuss in further detail the behaviour of these stable configurations. As previously stated, we perturb each configuration in two ways: first, by the implosion of the field χ, and second, by truncation errors. In both cases, we find that the Q-balls respond to the perturbations by oscillating continuously around the equilibrium configurations. An illustration of this behaviour is given in Figure 4.2. Initially, the gauged Q-ball remains

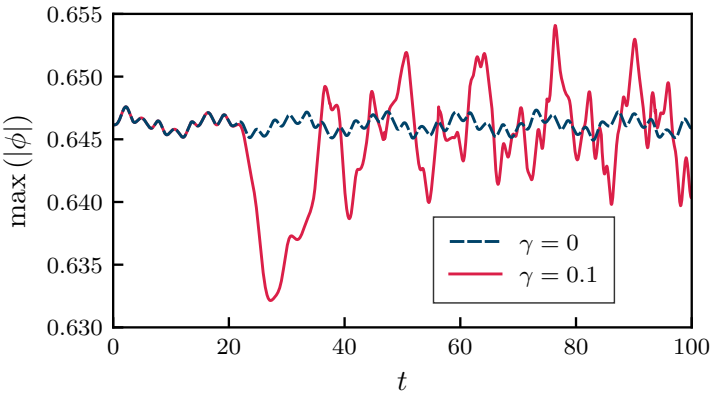

Figure 4.2: Oscillations in the maximum of the scalar field modulus $|\phi|$ for the stable gauged Q-ball corresponding to configuration A in Table 4.1. The results from two evolutions are shown. For the case where $\gamma = 0$ in (4.20), the field χ has no influence on the evolution of the Q-ball and the fields are perturbed only by the inherent error of the numerical simulation. For the case where $\gamma = 0.1$, the field χ interacts with the Q-ball starting at $t \approx 20$ and induces relatively large oscillations in the Q-ball modulus. We note that the amplitude of the induced oscillations for the case of $\gamma = 0.1$ is highly dependent on the precise shape of the pulse as defined through (4.21)–(4.22).

at the origin and is perturbed only by truncation error. At $t \approx 20$, the field χ suddenly implodes through the origin. For the case where $\gamma = 0.1$, this pulse interacts with the Q-ball and induces relatively large oscillations in the scalar field modulus $|\phi|$ which slightly distort the Q-ball profile. Additionally, the asymmetry of the imploding pulse imparts a small momentum "kick" to the Q-ball which sets it drifting away from the origin very slowly. However, for the case of $\gamma = 0$, the imploding pulse has no effect on the Q-ball and it remains stationary. By continuing the evolution until $t = 1200$, we observe that these general behaviours continue indefinitely—there is no significant change to the oscillatory pattern in either case. We therefore conclude that the corresponding solutions are stable.

Turning next to the unstable configurations in Figure 4.1, we observe two disconnected branches with distinct behaviour. On the leftmost branch in the figure (labelled "blowup" and marked by red open circles), we find that the evolutions quickly become singular as the scalar field grows without bound in response to the perturbations. As described in [1], this behaviour can reasonably be attributed to the potential (4.5) being unbounded from below. In particular, it may become energetically favourable for the scalar field modulus to increase as the perturbations drive the field to a state of minimal $V(|\phi|)$. However, since there is no lower bound on $V(|\phi|)$ for large $|\phi|$, the energy density can become locally negative and the growth can continue indefinitely in a runaway effect. Since the resulting configurations do not retain any resemblance to the initial Q-ball, we classify them as unstable. We note that similar behaviour has also been observed in other Q-ball models which can attain negative

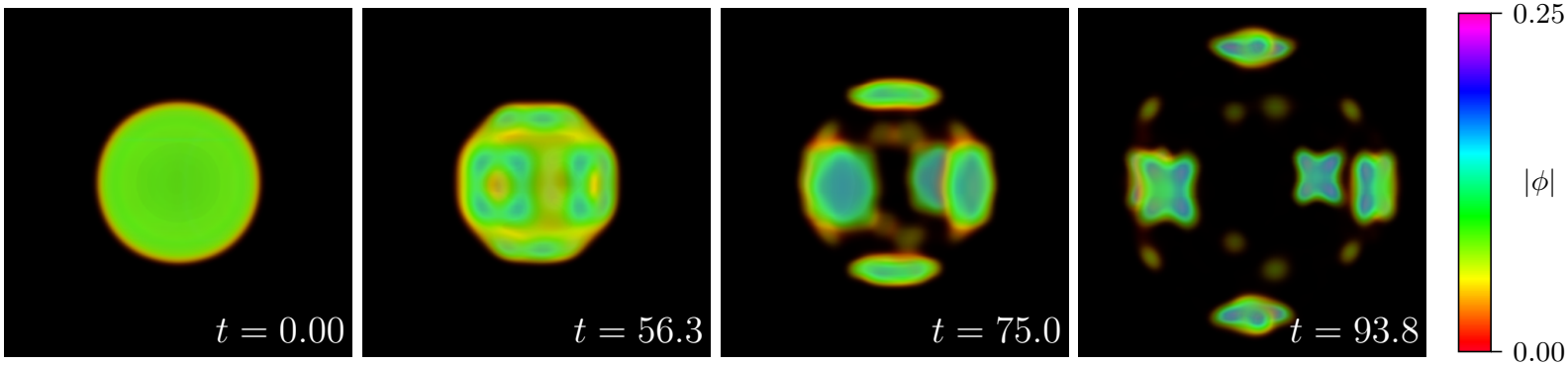

Figure 4.3: Evolution of the scalar field modulus $|\phi|$ for the "gauged Q-shell" corresponding to configuration B in Table 4.1. A three-dimensional view is shown; at the initial time, the fields are shell-like. As the evolution proceeds, the shell quickly breaks apart into smaller components which propagate away from the origin. Note that we have set $\gamma = 0$ for this evolution (i.e., the fields are perturbed only by the inherent numerical error of the simulation).

energy densities [135, 136].

On the rightmost unstable branch of Figure 4.1 (marked by red solid circles), we observe that the gauged Q-balls are quickly destroyed in response to the perturbations and can evolve in several ways. The most common outcome is the fragmentation of the original Q-ball into several smaller components. As an illustrative example, we plot in Figure 4.3 the evolution of a gauged Q-ball which corresponds to configuration B in Table 4.1. This configuration is noteworthy in that it represents a shell-like concentration of the fields (a "gauged Q-shell" [88]) at the initial time. As the evolution proceeds, we observe that the Q-shell eventually breaks apart into six main components which travel coincident with the coordinate axes. We note that this instability, along with every other instability on the unstable branches of Figure 4.1, can manifest quickly even without the influence of the perturbing field χ (i.e., with $\gamma = 0$). However, the specific manner in which the Q-ball breaks apart will depend on the configuration under study.

One notable feature of the evolution depicted in Figure 4.3 is the absence of any ring-like structures ("gauged Q-rings") after the Q-shell has broken apart. For the equivalent evolution in axisymmetry (see Figure 7 of [1]), it has been reported that this particular configuration can result in the formation of gauged Q-rings which survive for some time. However, the absence of such structures in Figure 4.3 suggests that the creation of Q-rings may be suppressed in full 3D. While we have still observed the formation of rings in other cases, we find that they are rare and usually break apart into smaller gauged Q-balls shortly after they appear. This indicates that long-lived gauged Q-rings may be considerably less common in three spatial dimensions (at least, for the type of evolutions and perturbations described here).

Next, we consider gauged Q-ball stability for the polynomial potential (4.6) with $e = 0.17$. Once again, we begin the analysis by applying the shooting procedure of Section 4.3.1 to find gauged Q-ball configurations in the model. The space of solutions for this case is shown in Figure 4.4. As stated previously, the choice $e = 0.17$ is near the maximum allowable for the polynomial potential and no gauged Q-balls can be found with $\omega > 1$ [96]. This significantly limits the range of possible solutions at large gauge coupling. Similar to the case of the logarithmic model, we evolve each configuration in Figure 4.4 twice (once with $\gamma = 0$ and once with $\gamma = 0.1$) up to at least $t = 1200$ in order to assess the stability. Notably, we find no evidence for configurations which are unstable with respect to three-dimensional perturbations. This agrees with what has previously been reported for the equivalent evolutions in axisymmetry [1].

To conclude this section, let us examine the stability of gauged Q-balls for the polynomial potential (4.6) with $e = 0.02$. In this case, the gauge coupling is much smaller than what has been considered above and the space of possible solutions is correspondingly larger. We

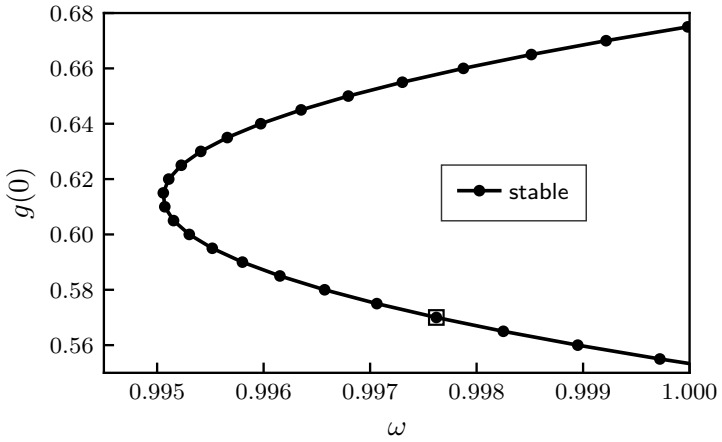

Figure 4.4: Shooting results and regions of stability for gauged Q-balls in the polynomial model (4.6) with $e = 0.17$. Plotted is the numerical shooting parameter $g(0) = \omega - eA_0(0)$ versus the Q-ball oscillation frequency ω. All configurations tested in the model (represented by black solid circles) are found to be stable with respect to generic three-dimensional perturbations. The open square represents the location of configuration C from Table 4.1.

previously examined this scenario in axisymmetry [1] and found that the transition points between stability and instability in the solution space match closely with the transition points predicted for non-gauged Q-balls with $e = 0$. However, it was also noted that some solutions near the transition point exhibit "large oscillations in the Q-ball interior which significantly disrupt the shape of the configuration but do not cause the Q-ball to immediately break apart". Since these solutions could not definitively be said to retain their initial shape, they were classified as unstable. Moreover, the recent results of [92] suggest a discrepancy between the transition point predicted by analytical calculations and the transition point identified numerically in [1]. Motivated by these factors, we now revisit this scenario and examine the same phenomenon using our fully three-dimensional code.

In Figure 4.5, we plot the space of solutions for gauged Q-balls in the polynomial model (4.6) with $e = 0.02$. The curve can be broken down into three branches: an upper unstable branch I, a stable branch II, and a lower unstable branch III. Notably, the lower part of branch II and all of branch III are characterized by scalar field profiles which are step function-like and resemble the thin-wall Q-balls [22]. Once again, we perturb each configuration twice by setting $\gamma = 0$ and $\gamma = 0.1$. Any gauged Q-balls which are clearly destroyed in response to either perturbation are classified as unstable while those which oscillate weakly or return toward the original configuration are classified as stable. For the solutions along branch I, we also observe that the Q-balls appear to collapse into solutions which lie along the stable branch II; we also classify these as unstable, though we comment that this behaviour makes it somewhat difficult to precisely identify the onset of instability.

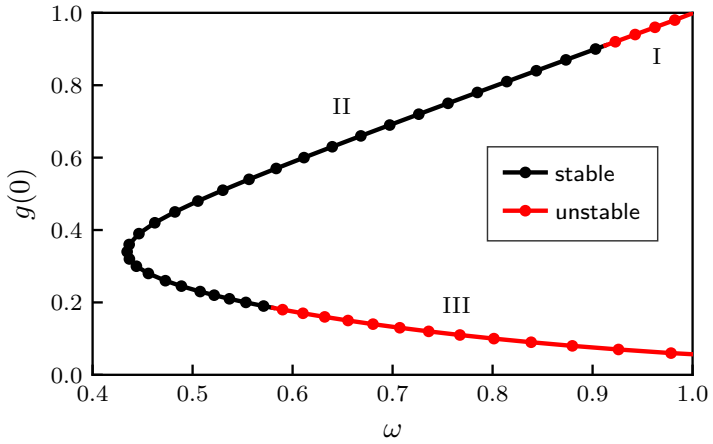

Figure 4.5: Shooting results and regions of stability and instability for gauged Q-balls in the polynomial model (4.6) with $e = 0.02$. Plotted is the numerical shooting parameter $g(0) = \omega - eA_0(0)$ versus the Q-ball oscillation frequency ω. The black solid circles along branch II represent configurations which are found to be stable with respect to generic three-dimensional perturbations. The red solid circles along branches I and III represent configurations which are found to be unstable with respect to these perturbations.

The salient feature of Figure 4.5 in comparison to Figure 12 of [1] is the different location for the transition point between branches II and III of the figure. In particular, this transition point is found to occur at a larger value of ω in three spatial dimensions and the "large oscillations" observed in axisymmetry are altogether absent. To verify this claim further, we have evolved the configurations with $g(0) < 0.34$ in Figure 4.5 up to at least $t = 5000$. Since the 3D simulations are expected to fully capture all unstable modes which would arise under axisymmetry assumptions, we conclude that this is a distinct result from what was reported in [1].

The origin of the "large oscillations" observed in axisymmetry is therefore puzzling, though it might reasonably be attributed to the unique numerical challenge of evolving the gauged Q-balls which lie along the lower part of branch II and branch III. In particular, the large thin-wall shape of these solutions results in sharp field gradients arising near the edge of the Q-ball. This can make it difficult to smoothly resolve the Q-ball boundary unless significant computational resources are expended. At the same time, we find that the instabilities of the Q-balls along this branch may only definitively manifest after several thousand time steps. This contrasts what is observed for other unstable gauged Q-balls in the logarithmic and polynomial models where the instabilities become obvious rather quickly. Together, these factors might result in the accumulation of numerical errors at late times which obscure the stability picture. For example, the oscillations observed in axisymmetry might possibly be due to a "de-phasing" of the periodic parts (real and imaginary) of

the complex scalar field which eventually build up and disfigure the Q-ball profile. However, the fourth-order finite-difference scheme used in the present work is of a higher accuracy than the second-order method used in [1], so this may explain why such numerical artefacts are not observed here. Alternatively, the oscillations observed in axisymmetry may arise due to the different boundary conditions used or due to problems with the regularity of the evolved fields along the axis of symmetry at late times. In any case, the results of Figure 4.5 suggest that the location of the instability threshold for these gauged Q-balls does not correspond so nearly with the prediction made by the stability criterion $(\omega/Q)\, dQ/d\omega < 0$ [132]. This contrasts what was previously reported in [1] but appears to agree with recent analytical findings [92].

4.4.2 Collisions

We now consider relativistic collisions of gauged Q-balls in three spatial dimensions. To construct the binary system, we use the procedure described in Section 4.3.1. The Q-balls are initialized at $z = \pm 25$ with initial velocities in the range $0.2 \leq v \leq 0.8$. Additionally, we define the impact parameter b as the linear distance between the center of the each Q-ball in the plane perpendicular to the initial motion. In our evolutions, we also test the effects of the relative phase difference α and the relative sign of the Noether charge Q on the outcome of the collision. The phase difference α is defined through a modification of the basic Q-ball ansatz (4.11),

$$\phi(t, \vec{x}) = f(r)\, e^{\epsilon(i\omega t) + i\alpha}. \tag{4.27}$$

By adjusting $\alpha \in [0, \pi]$ for one Q-ball in the binary, a relative difference in phase can be introduced into the system. This phase difference is preserved until the moment of impact for collisions of Q-balls with identical ω. Additionally, adjusting the parameter $\epsilon = \pm 1$ (while also taking $A_0(r) \to -A_0(r)$ in (4.12)) for one Q-ball in the binary can flip the overall sign of its Noether charge Q. In this manner, the dynamics of Q-ball/anti-Q-ball collisions can be investigated.

For all results presented below, we restrict our analysis to collisions involving configurations A and C in Table 4.1. Since configuration A is identical to configuration LogC in [2], and since configuration C is identical to configuration PolyB in [2], this enables a direct comparison between the collision dynamics in axisymmetry and the equivalent dynamics in three spatial dimensions. To facilitate this comparison, we have performed a number of head-on collision simulations of gauged Q-balls in 3D; we find the dynamics of these collisions to be broadly consistent with the axisymmetric case. In the discussion below, we will briefly review these results before turning to collision scenarios with non-zero impact parameter (which are unique to 3D).

We first discuss the effects of the initial velocity v on the outcome of head-on collisions with equal charge. For both A and C in Table 4.1, we find that the Coulomb repulsion of the gauged Q-balls can prevent any significant overlap of their respective scalar field content at low collision velocities. Instead, the Q-balls travel toward each other, reach a turning point of vanishing speed and then propagate back toward the boundaries. This occurs for $v \lesssim 0.3$ for configuration A and $v \lesssim 0.2$ for configuration C. At higher velocities, the gauged Q-balls are able to overcome their mutual repulsion and can behave in several different ways. For configuration A, we find that the outcome is typically a fragmentation of the gauged Q-balls into several smaller components. In most cases, a significant fraction of each original Q-ball continues to travel along the z-axis after the collision. This is usually accompanied by the formation of smaller field remnants which are left behind near the origin and may travel away in different directions. For the case of configuration C, we find that the equivalent collisions result in the merger of the gauged Q-balls along with the emission of significant field content in the form of outgoing waves. At the highest collision velocities (e.g., $v \gtrsim 0.7$ for configuration A and configuration C), an increasing fraction of the field content travels parallel to the z-axis after the collision. As illustrated in Figure 4.6, this is accompanied by the development of a destructive interference pattern in $|\phi|$ at the moment of impact as well as the formation of gauged Q-rings in the case of configuration A.

We now turn to head-on collisions of gauged Q-balls with phase differences and opposite charges. It is well-known that the introduction of a phase difference can induce charge transfer between colliding Q-balls [77]. Here we observe similar behaviour using $\alpha = \pi/4$ as a sample value. As in [2], we find that the gauged Q-balls created during the charge transfer process will often fragment into smaller Q-balls or even create transient Q-rings. In the case of configuration C, we also find some examples where the gauged Q-balls created during the collision will almost completely dissipate. However, the rate of charge transfer is found to decrease as $v \to 1$ in both cases. For head-on collisions with opposite charges, we find that the Coulomb force (which is now attractive) can accelerate the gauged Q-balls prior to the moment of impact. After the collision, the total Noether charge in the system is reduced as the Q-balls have partially annihilated. This process can create smaller Q-ball remnants which lag the main Q-balls (which are now highly perturbed) and propagate along or away from the z-axis. It can also produce a wake of scalar radiation or a quasispherical pulse of electromagnetic radiation which emanates from the origin. In general, we find that the amount of charge which is annihilated depends on the collision velocity, with the least amount of annihilation occurring at the largest velocities.

While the above results are broadly consistent with the equivalent calculations in axisymmetry [2], we comment here on some subtle differences. One main difference relates to the behaviour of any gauged Q-rings which are created during the collisions. In axisymme-

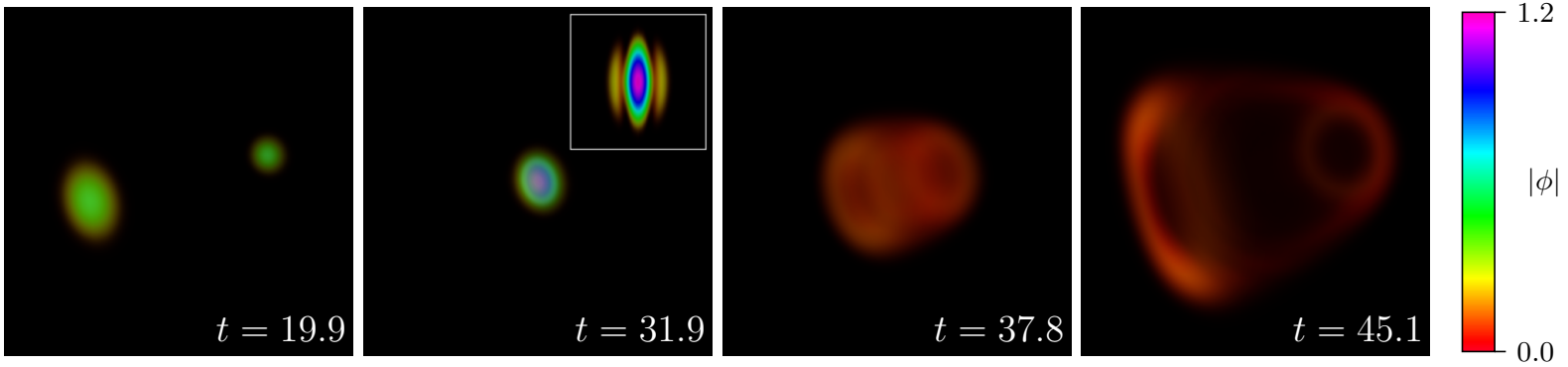

Figure 4.6: Evolution of the scalar field modulus $|\phi|$ for a collision involving configuration A from Table 4.1 with equal charge, velocity $v = 0.8$, phase difference $\alpha = 0$, and impact parameter $b = 0$. A three-dimensional off-angle view is shown. The Q-balls collide at $t \approx 32$ and interfere destructively; this is shown from a cross-sectional side-on perspective in the inset graphic of the second panel. After the collision, the field content predominantly takes the form of two Q-rings which also carry a cylindrical "wake" of scalar matter.

try, Q-rings were found to be a rather common outcome of intermediate- and high-velocity collisions that resulted in gauged Q-ball fragmentation. In these cases, the rings tended to propagate some distance away from the origin before collapsing back onto the axis of symmetry at late times (though this final fate could not be confirmed in all cases). While we have still observed the formation of gauged Q-rings in our fully three-dimensional simulations, we find that they tend to quickly break apart into a number of spherical gauged Q-balls in the majority of cases. It is only in rare circumstances (such as the scenario depicted in Figure 4.6) where we have observed that the Q-rings can survive long enough to reach a radius which is many times greater than the size of the original Q-ball. This reaffirms our comments in Section 4.4.1 that Q-ring formation, while not explicitly forbidden, may be a rare phenomenon in the absence of symmetry restrictions.

Having discussed the dynamics of head-on collisions, we now focus on the case where the impact parameter b is non-zero. Since these "off-axis" collisions are obviously forbidden in axisymmetry, they represent a novel dynamical scenario which has not been explored in the previous studies. We begin by considering off-axis collisions of equal-charge gauged Q-balls. In this case, we find that a common outcome is the "deflection" of the gauged Q-balls due to the influence of the repulsive gauge field. This can result in the Q-balls following a discernible curved trajectory which makes an angle θ with the z-axis at late times. The exact value of θ for a given collision can depend on several factors such as the initial velocity v and the impact parameter b. For equal-charge collisions, we find that θ is generally maximized when v and b are small (in fact, one could interpret the repulsive scenario discussed above for head-on collisions with equal charge and low velocity as a case of maximal deflection where $\theta = \pi$). However, when v is sufficiently large and b is not larger than the approximate Q-ball width, the scalar fields from each Q-ball can "graze" each other during the collision. In this case, the end result may be a fragmentation or merger of the gauged Q-balls. In Figure 4.7, we plot a "grazing" collision of configuration A from Table 4.1 with equal charge, velocity $v = 0.6$, phase difference $\alpha = 0$, and impact parameter $b = 2$. The gauged Q-balls collide at $t \approx 43$ with a majority of the field content emerging at an angle $\theta \approx \pi/4$ with respect to the z-axis. We also observe that the initial gauged Q-balls have partially fragmented into smaller objects which travel close to the z-axis. Repeating the calculation shown in Figure 4.7 for a variety of choices of v and b, we find that the outcomes are broadly consistent with what has been described above, though the deflection angles and fragmentation products may differ depending on the specific collision parameters.

In Figure 4.8, we plot a collision involving configuration C from Table 4.1 with equal charge, velocity $v = 0.4$, phase difference $\alpha = 0$, and impact parameter $b = 4$. In contrast to what is shown in Figure 4.7 for configuration A, here we see that the end result is a merger

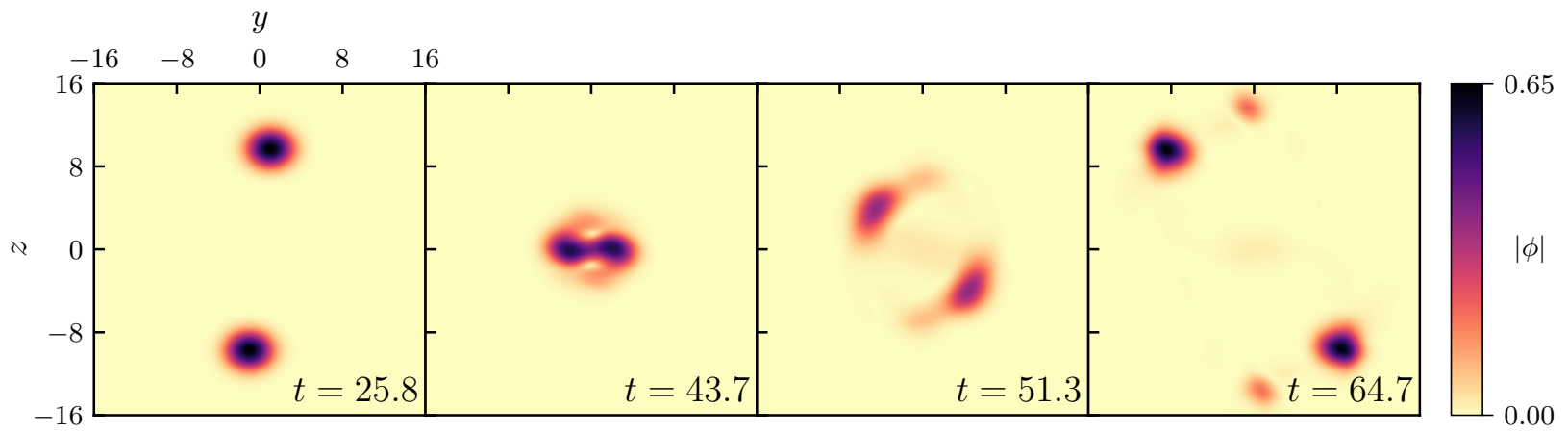

Figure 4.7: Evolution of the scalar field modulus $|\phi|$ for a collision involving configuration A from Table 4.1 with equal charge, velocity $v = 0.6$, phase difference $\alpha = 0$, and impact parameter $b = 2$. A two-dimensional slice through the $x = 0$ plane is shown. The Q-balls collide at $t \approx 43$ and fragment into smaller components which travel away in different directions. While the dynamics in this case are mostly planar, we comment that small amounts of field content also propagate away from the collision plane; this field content is not shown in the figure.

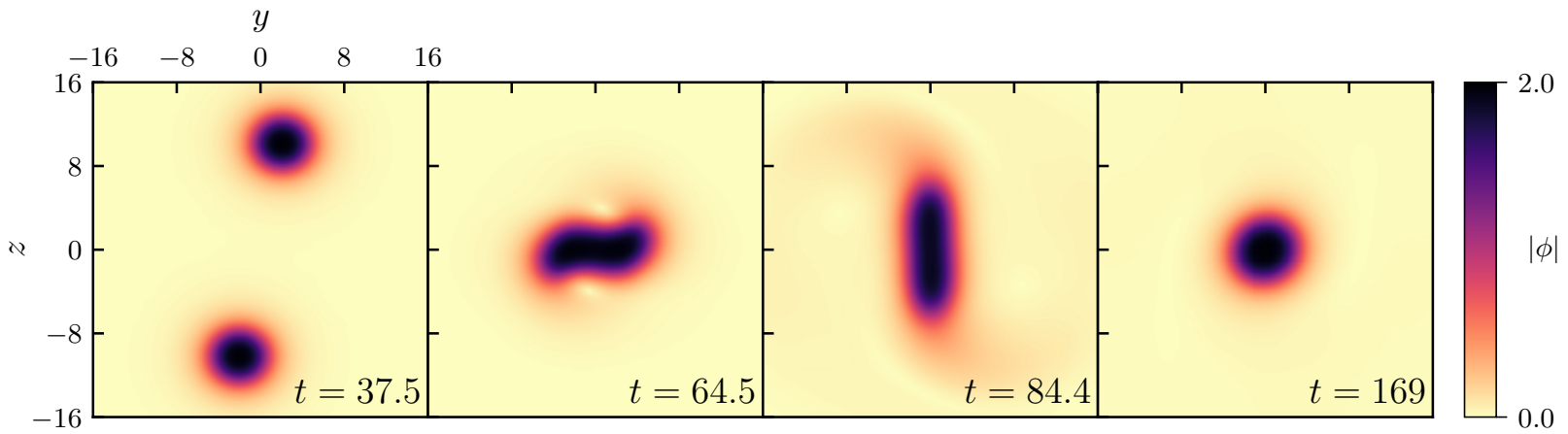

Figure 4.8: Evolution of the scalar field modulus $|\phi|$ for a collision involving configuration C from Table 4.1 with equal charge, velocity $v = 0.4$, phase difference $\alpha = 0$, and impact parameter $b = 4$. A two-dimensional slice through the $x = 0$ plane is shown. The Q-balls collide at $t \approx 64$ and merge into a single gauged Q-ball which remains at the origin. In this process, a considerable amount of the field content is radiated away toward the boundaries.

of the original gauged Q-balls. During the merger process, a significant amount of field content is radiated away toward the boundaries in the form of aspherical waves. By $t \approx 169$ (the last panel in the figure), the merged configuration has settled down into a single gauged Q-ball centered at the origin which remains slightly perturbed. The properties of this final merged state turn out to be similar in some ways to the properties of configuration C before the collision. For example, the scalar field attains a value of $|\phi| \approx 1.98$ at the origin by $t \approx 169$ while the oscillation frequency (which we determine by tracking the real part of the scalar field during the collision) is found to be $\omega \approx 0.99$ in the merged state. This result might be expected for gauged Q-balls with $e = 0.17$ in the potential (4.6) since the space of possible solutions is extremely small (see Figure 4.4). For configuration C, we find that mergers are a common outcome for moderate values of the collision velocity and impact parameter. At larger values of v and b, the gauged Q-balls can avoid the merged state through (for example) deflection of the fields.

It is worthwhile to discuss the final state of Figure 4.8 in greater detail. Due to the off-axis motion of the binary, the total angular momentum of the system is non-zero at the initial time. It is plausible that some of this angular momentum may be retained by the merged configuration at late times, potentially representing an object analogous to a spinning Q-ball [43, 44]. At a visual level, the elongated and "rotating" appearance of $|\phi|$ in the second and third panel of Figure 4.8 may also seem to support this idea. However, there are several reasons why the final merged state is unlikely to represent a configuration of this type. First, we observe that the gauged Q-ball very quickly returns to a near-spherical shape by $t \approx 169$ through the emission of significant field content toward the boundaries. However, field configurations with angular momentum are not expected to be spherically-symmetric and may also be characterized by the presence of nodes away from the center [43]. Second, we have explicitly computed the angular momentum tensor,

$$M^{ij} = \int (x^i T^{j0} - x^j T^{i0})\, d^3x, \tag{4.28}$$

and found that the x-component of the angular momentum, $J_x = M^{23}$, is almost totally radiated away from the origin by $t \approx 169$. Since the angular momentum of a spinning Q-ball (at least, in the non-gauged case) is expected to be an integer multiple of the Noether charge Q, we conclude that mergers of this type are unlikely to represent the usual spinning structures. At the same time, we cannot rule out the possibility that some small amount of angular momentum will still be retained in the merged state even at later times. If so, the configuration might be analogous to the "slowly rotating" Q-balls recently proposed in [46].

Next we turn to off-axis collisions of gauged Q-balls with opposite charges. Unlike

the repulsive behaviour seen for the equivalent collisions with equal charge, here we observe that the Q-balls experience an attractive acceleration which curves their trajectories toward the origin. If the impact parameter and initial velocity are sufficiently large, the Q-balls may pass by one another without any significant interaction between their respective scalar fields. This is similar to the "deflection" described above for the equal-charge collisions, though now the deflection occurs in the opposite direction (i.e., toward the other Q-ball in the binary rather than away from it). If the impact parameter is small, the Q-balls will generally experience a "grazing" collision which can result in several possible outcomes. Most commonly, the gauged Q-balls will partially annihilate and fragment into a number of smaller components (for the case of configuration A) or radiate a portion of the field content toward the boundaries (for the case of configuration C); this is similar to their behaviour during head-on collisions. In Figure 4.9, we plot the Noether charge density Q for a grazing collision involving configuration A from Table 4.1 with initial velocity $v = 0.5$, phase difference $\alpha = 0$, and impact parameter $b = 4$. During the collision, the Q-balls complete a partial orbit around each other before escaping along a trajectory which is roughly perpendicular to their initial motion. A number of positively- and negatively-charged remnants are also created during the collision in the vicinity of the origin. By $t \approx 70.9$, approximately half of the total charge in the system has been annihilated. The acceleration and annihilation of charges during this process can also result in the production of an electromagnetic radiation pulse. In Figure 4.10, we plot the energy contained in the electromagnetic field,

$$E_{\mathrm{EM}} = \frac{1}{2}\left(|\vec{E}|^2 + |\vec{B}|^2\right), \tag{4.29}$$

where $\vec{E}$ and $\vec{B}$ are the electric and magnetic field vectors, respectively. By comparing Figure 4.9 and Figure 4.10, we can see that a pulse of outgoing energy is created in the electromagnetic field which does not correspond to any significant amount of charge. We interpret this as representing electromagnetic radiation. We find the production of electromagnetic radiation to be a general phenomenon associated with gauged Q-ball/anti-Q-ball collisions, though the exact amount of radiation produced may depend on both the motion of the charges and the total amount of annihilation which occurs in the system.

To conclude this section, let us comment briefly on the off-axis collision of gauged Q-balls with a phase difference of $\alpha = \pi/4$. Similar to the case of head-on collisions, we find that the introduction of a relative phase difference can result in the transfer of charge between the colliding Q-balls. When the impact parameter is non-zero, the dynamics of this charge transfer can be altered in minor ways. For example, the charge transfer may occur asymmetrically such that the resulting Q-balls are left travelling at an angle relative to their initial motion; this angle can depend on both the collision velocity and the impact

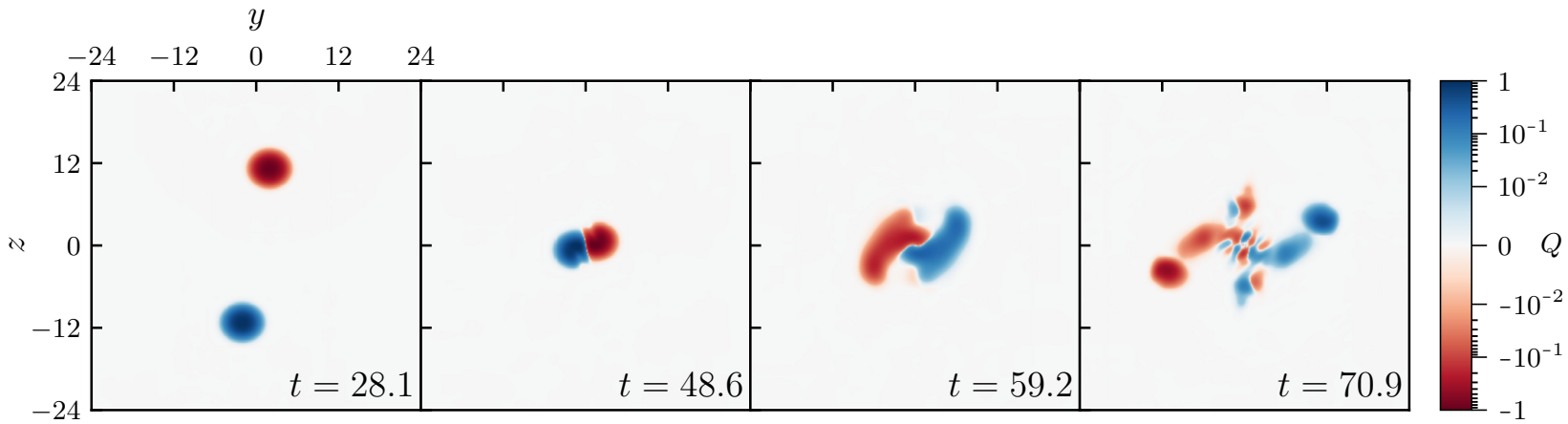

Figure 4.9: Evolution of the Noether charge Q for a collision involving configuration A from Table 4.1 with opposite charge, velocity $v = 0.5$, phase difference $\alpha = 0$, and impact parameter $b = 4$. A two-dimensional slice through the $x = 0$ plane is shown. The Q-balls collide at $t \approx 48$ and fragment into smaller components after partially annihilating. While the dynamics in this case are mostly planar, we comment that small portions of charge also propagate away from the collision plane; these small charges are not shown in the figure. Note that a hybrid colormap is used: charge values below $|Q| = 10^{-2}$ are mapped linearly to zero while values above this threshold are mapped logarithmically to the charge maximum.

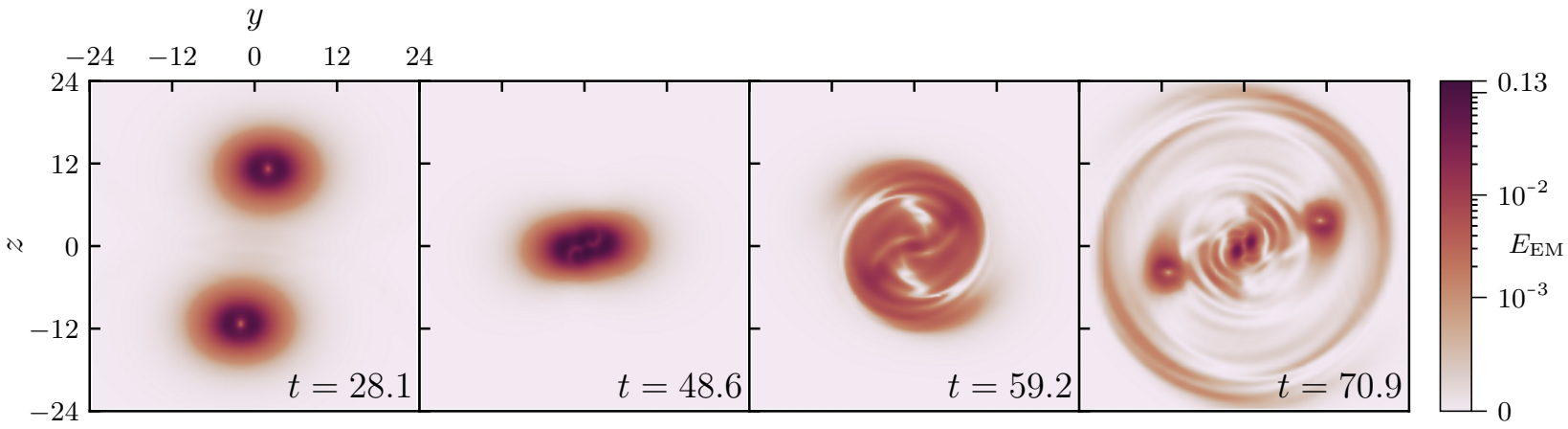

Figure 4.10: Evolution of the electromagnetic field energy E_{EM} for a collision involving configuration A from Table 4.1 with opposite charge, velocity $v = 0.5$, phase difference $\alpha = 0$, and impact parameter $b = 4$. A two-dimensional slice through the $x = 0$ plane is shown. The Q-balls collide at $t \approx 48$ and fragment into smaller components after partially annihilating. After the collision, a pulse of electromagnetic energy emanates from the origin (fourth panel). The shape of this pulse is not limited to the y–z plane shown here; it can be seen to propagate in all directions when viewed three-dimensionally. Note that a hybrid colormap is used: energy values below $E_{\mathrm{EM}} = 10^{-3}$ are mapped linearly to zero while values above this threshold are mapped logarithmically to the energy maximum.

parameter. As the impact parameter is further increased, the amount of charge transfer appears to be reduced due to the smaller surface of contact between the colliding Q-balls. Otherwise, the charge transfer during off-axis collisions can generally be said to resemble the results for head-on collisions (including phenomena such as fragmentation or dissipation of the resulting Q-balls).

4.5 Conclusion

In this work, we have studied the dynamical behaviour of $U(1)$ gauged Q-balls using fully three-dimensional numerical evolutions. First, we investigated the classical stability of gauged Q-balls with respect to generic three-dimensional perturbations. Second, we explored the dynamics of gauged Q-balls during head-on and off-axis collisions at relativistic velocities.

With regard to stability, we have found numerical evidence for gauged Q-balls which remain stable against generic perturbations over long dynamical timescales. To reach this conclusion, we have perturbed the Q-balls in two different ways: through the inherent numerical error of our finite-difference implementation and through the interaction of an auxiliary scalar field which acts as a perturbing agent. Testing configurations in the logarithmic model, we have found evidence for both stable and unstable branches in the solution space. The solutions on the stable branch tend to respond to the perturbations by oscillating continuously near the initial configuration. The solutions on the unstable branch are found to break apart in various ways (usually into a number of smaller gauged Q-balls). We have also tested configurations in the sixth-order polynomial scalar field model, finding no evidence of unstable configurations for our choice of the model parameters with $e = 0.17$. Finally, we have revisited the case of $e = 0.02$ in the polynomial model and found a new result for the transition point between stability and instability in the solution space. This result differs from what was found in [1] but appears to be in agreement with recent analytical findings [92].

With regard to relativistic collisions of gauged Q-balls, we have tested the effect of the initial velocity, relative phase, relative charge, and impact parameter on the outcome of the collision. For the case of head-on collisions, we have found that the dynamics in three spatial dimensions are broadly consistent with previous results reported under axisymmetry assumptions [2]. For the case of off-axis collisions, we have found that the impact parameter can play a significant role in modifying the collision outcome. For example, the gauged Q-balls can experience attractive or repulsive "deflections" from their initial trajectories depending on their relative charges, velocities, and the collision impact parameter. In other cases, the Q-balls may experience "grazing" collisions which can modify the dynamics during Q-ball fragmentation and mergers. Aside from these differences, the main phenom-

ena associated with these collisions (such as charge transfer, annihilation, and radiation production) are found to be similar to the head-on case.

The results of this work are significant for several reasons. First, they address the general question of gauged Q-ball classical stability which was originally raised in [95]. Second, they provide new insights into the time-dependent behaviour of gauged Q-balls in realistic three-dimensional settings. Together, these results may be relevant for future studies of Q-balls in various physical contexts (such as in early-Universe cosmology). At the same time, we hope that this work may inspire further numerical explorations of related soliton models such as Proca Q-balls [90], spinning Q-balls [43, 44, 46], and charge-swapping Q-balls [47–49].

Chapter 5

Conclusion

In this thesis, we have studied a class of non-topological solitons which are known as gauged Q-balls. Using numerical simulations as the primary tool, we have explored the time-dependent behaviour of these objects in various scenarios. Our work has focused on two open questions in the literature: the stability of gauged Q-balls with respect to perturbations of the fields and the dynamics of gauged Q-balls during relativistic collisions.

In Chapter 2, we investigated the stability of gauged Q-balls under assumptions of axial symmetry. There we found evidence for both stable and unstable configurations in logarithmic and polynomial scalar field models. For those solutions belonging to the stable branch, the gauged Q-balls tended to respond to the perturbations by oscillating lightly or weakly radiating before returning toward a stationary configuration. For those solutions on the unstable branch, the gauged Q-balls were eventually destroyed or disfigured by the growth of the initial perturbations. In some cases, we observed that the instabilities could result in the formation of ring-like structures which we called "gauged Q-rings". When the gauge coupling was small, we also found evidence for non-spherical unstable modes and mapped the approximate regions of stability and instability in the solution space.

In Chapter 3, we investigated the dynamics of gauged Q-balls during head-on collisions at relativistic velocities. Working again in axisymmetry, we tested the effects of the initial velocity, relative phase, relative charge, and electromagnetic coupling strength on the collision outcome. Consistent with previous studies of non-gauged Q-balls, we found that relative phase differences could result in the transfer of charge during the collision and that the Q-balls could partially annihilate if they collided with opposite charge. Unique to the gauged case, we also found that this charge annihilation could result in the creation of an electromagnetic radiation pulse. With regard to the collision velocity, we found that the long-range Coulomb force could accelerate or decelerate the gauged Q-balls prior to the moment of impact. At high velocities, electromagnetic effects significantly reduced the

elasticity of the collisions when the gauge coupling was large. Broadly speaking, these phenomena were found to be independent of the choice of the scalar field potential.

In Chapter 4, we investigated the stability and collisions of gauged Q-balls in three spatial dimensions. Extending the analyses of Chapter 2 and Chapter 3, we considered novel dynamical scenarios which were not accessible under previous symmetry assumptions. This includes the stability of gauged Q-balls with respect to generic 3D perturbations and the collisions of gauged Q-balls with a non-zero impact parameter. The principal new result from this study is the observation that gauged Q-balls can remain stable even when subject to these generic perturbations. A secondary result is the identification of the impact parameter as a relevant factor in gauged Q-ball collisions. We also reexamined several head-on collision scenarios and found the results to be consistent with those observed in axisymmetry.

Having surveyed the broad features of gauged Q-ball dynamics, it would be interesting to study some aspects in further detail. For example, our simulations showed that the formation of gauged Q-rings can be a common outcome of dynamical processes involving gauged Q-balls. It would be worthwhile to investigate these structures more closely to determine their lifetimes and other properties. With respect to gauged Q-ball collisions, the parameter space of possible scenarios is very large and our study could not be exhaustive. It may be useful to continue this exploration, particularly in three dimensions. Finally, our computer code would be well-suited to studying other time-dependent Q-ball phenomena such as superradiance [146–148] and charge-swapping behaviour [47–49]. We leave this as future work.

In closing, we comment that the study of soliton behaviour remains a fertile ground for exploration and discovery. While our work has been limited to gauged Q-balls in particular, it isn't difficult to imagine that the dynamics of related soliton models may be equally rich and compelling. As the pace of research in this area accelerates, we hope that numerical experimentation in the spirit of this thesis will continue to yield valuable insights into soliton behaviour.

Bibliography

[1] M. P. Kinach and M. W. Choptuik, Phys. Rev. D **107**, 035022 (2023).

[2] M. P. Kinach and M. W. Choptuik, Phys. Rev. D **110**, 015012 (2024).

[3] M. P. Kinach and M. W. Choptuik, Phys. Rev. D **110**, 075033 (2024).

[4] S. Coleman, "Classical Lumps and Their Quantum Descendants," in *New Phenomena in Subnuclear Physics: Part A*, edited by A. Zichichi (Springer, Boston, MA, United States, 1977) pp. 297–421.

[5] F. Marin, "Solitons: Historical and Physical Introduction," in *Encyclopedia of Complexity and Systems Science*, edited by R. A. Meyers (Springer, New York, NY, United States, 2009) pp. 8464–8479.

[6] R. Rajaraman, *Solitons and Instantons: An Introduction to Solitons and Instantons in Quantum Field Theory*, 1st ed. (North-Holland, Amsterdam, The Netherlands, 1982).

[7] E. J. Weinberg, *Classical Solutions in Quantum Field Theory: Solitons and Instantons in High Energy Physics*, 1st ed., Cambridge Monographs on Mathematical Physics (Cambridge University Press, Cambridge, England, 2012).

[8] J. S. Russell, *Report on Waves: Made to the Meetings of the British Association in 1842–43* (British Association Reports, London, England, 1845).

[9] D. J. Korteweg and G. de Vries, Philos. Mag. **39**, 422 (1895).

[10] E. Fermi, J. Pasta, S. Ulam, and M. Tsingou, *Studies of Nonlinear Problems*, Tech. Rep. LA-1940 (Los Alamos National Laboratory, 1955).

[11] N. J. Zabusky and M. D. Kruskal, Phys. Rev. Lett. **15**, 240 (1965).

[12] T. H. R. Skyrme, Proc. R. Soc. Lond. A **260**, 127 (1961).

[13] T. H. R. Skyrme, Nucl. Phys. **31**, 556 (1962).

[14] M. Toda, J. Phys. Soc. Jpn. **23**, 501 (1967).

[15] M. Toda, Prog. Theor. Phys. Suppl. **45**, 174 (1970).

[16] N. Manton and P. Sutcliffe, *Topological Solitons*, 1st ed., Cambridge Monographs on Mathematical Physics (Cambridge University Press, Cambridge, England, 2004).

[17] Y. M. Shnir, *Topological and Non-Topological Solitons in Scalar Field Theories*, 1st ed., Cambridge Monographs on Mathematical Physics (Cambridge University Press, Cambridge, England, 2018).

[18] G. H. Derrick, J. Math. Phys. **5**, 1252 (1964).

[19] S. Theodorakis, Phys. Rev. D **61**, 047701 (2000).

[20] I. E. Gulamov, E. Y. Nugaev, and M. N. Smolyakov, Phys. Rev. D **87**, 085043 (2013).

[21] D. Bazeia, M. A. Marques, and R. Menezes, Eur. Phys. J. C **76**, 241 (2016).

[22] J. Heeck, A. Rajaraman, R. Riley, and C. B. Verhaaren, Phys. Rev. D **103**, 045008 (2021).

[23] W. H. Press, S. A. Teukolsky, W. T. Vetterling, and B. P. Flannery, *Numerical Recipes: The Art of Scientific Computing*, 3rd ed. (Cambridge University Press, Cambridge, England, 2007).

[24] G. Rosen, J. Math. Phys. **9**, 996 (1968).

[25] R. Friedberg, T. D. Lee, and A. Sirlin, Phys. Rev. D **13**, 2739 (1976).

[26] J. Heeck and M. Sokhashvili, Eur. Phys. J. C **83**, 526 (2023).

[27] S. Coleman, Nucl. Phys. **B262**, 263 (1985).

[28] S. Coleman, Nucl. Phys. **B269**, 744 (1986).

[29] A. Kusenko, Phys. Lett. B **405**, 108 (1997).

[30] S. Kasuya and M. Kawasaki, Phys. Rev. D **61**, 041301(R) (2000).

[31] M. Dine and A. Kusenko, Rev. Mod. Phys. **76**, 1 (2004).

[32] J. A. Frieman, G. B. Gelmini, M. Gleiser, and E. W. Kolb, Phys. Rev. Lett. **60**, 2101 (1988).

[33] A. Kusenko, Phys. Lett. B **406**, 26 (1997).

[34] A. Kusenko and M. Shaposhnikov, Phys. Lett. B **418**, 46 (1998).

[35] A. Kusenko and P. J. Steinhardt, Phys. Rev. Lett. **87**, 141301 (2001).

[36] S. L. Liebling and C. Palenzuela, Living Rev. Relativ. **15**, 6 (2012).

[37] J. Heeck and M. Sokhashvili, Phys. Rev. D **107**, 016006 (2023).

[38] G. Rosen, Phys. Rev. **183**, 1186 (1969).

[39] G. C. Marques and I. Ventura, Phys. Rev. D **14**, 1056 (1976).

[40] K. Enqvist and J. McDonald, Phys. Lett. B **425**, 309 (1998).

[41] E. J. Copeland and M. I. Tsumagari, Phys. Rev. D **80**, 025016 (2009).

[42] H. Arodź and J. Lis, Phys. Rev. D **77**, 107702 (2008).

[43] M. S. Volkov and E. Wöhnert, Phys. Rev. D **66**, 085003 (2002).

[44] L. Campanelli and M. Ruggieri, Phys. Rev. D **80**, 036006 (2009).

[45] H. Arodź, J. Karkowski, and Z. Świerczyński, Phys. Rev. D **80**, 067702 (2009).

[46] Y. Almumin, J. Heeck, A. Rajaraman, and C. B. Verhaaren, Eur. Phys. J. C **84**, 364 (2024).

[47] E. J. Copeland, P. M. Saffin, and S.-Y. Zhou, Phys. Rev. Lett. **113**, 231603 (2014).

[48] Q.-X. Xie, P. M. Saffin, and S.-Y. Zhou, J. High Energy Phys. **07**, 062 (2021).

[49] S.-Y. Hou, P. M. Saffin, Q.-X. Xie, and S.-Y. Zhou, J. High Energy Phys. **07**, 060 (2022).

[50] N. Sakai, H. Ishihara, and K.-I. Nakao, Phys. Rev. D **84**, 105022 (2011).

[51] T. Tamaki and N. Sakai, Phys. Rev. D **86**, 105011 (2012).

[52] E. Nugaev and A. Shkerin, Phys. Rev. D **90**, 016002 (2014).

[53] K. Griest and E. W. Kolb, Phys. Rev. D **40**, 3231 (1989).

[54] D. F. Jackson Kimball, D. Budker, J. Eby, M. Pospelov, S. Pustelny, T. Scholtes, Y. V. Stadnik, A. Weis, and A. Wickenbrock, Phys. Rev. D **97**, 043002 (2018).

[55] S. Afach *et al.*, Ann. Phys. **536**, 2300083 (2024).

[56] A. Kusenko and I. M. Shoemaker, Phys. Rev. D **80**, 027701 (2009).

[57] Y. Takenaga *et al.* (Super-Kamiokande Collaboration), Phys. Lett. B **647**, 18 (2007).

[58] S. Kasuya, M. Kawasaki, and T. T. Yanagida, Prog. Theor. Exp. Phys. **2015**, 053B02 (2015).

[59] T. Chiba, K. Kamada, and M. Yamaguchi, Phys. Rev. D **81**, 083503 (2010).

[60] D. Croon, A. Kusenko, A. Mazumdar, and G. White, Phys. Rev. D **101**, 085010 (2020).

[61] K. D. Lozanov, M. Sasaki, and V. Takhistov, Phys. Lett. B **848**, 138392 (2024).

[62] S. Kasuya, M. Kawasaki, and K. Murai, J. Cosmol. Astropart. Phys. **05**, 053 (2023).

[63] M. Kawasaki and K. Murai, J. Cosmol. Astropart. Phys. **01**, 050 (2024).

[64] A. Derevianko and M. Pospelov, Nat. Phys. **10**, 933 (2014).

[65] C. Kouvaris, E. Papantonopoulos, L. Street, and L. C. R. Wijewardhana, Phys. Rev. D **102**, 063014 (2020).

[66] C. Blanco, B. Elshimy, R. F. Lang, and R. Orlando, Phys. Rev. D **105**, 115031 (2022).

[67] A. Ansari, L. S. Bhandari, and A. M. Thalapillil, Phys. Rev. D **109**, 023003 (2024).

[68] K. Enqvist and M. Laine, J. Cosmol. Astropart. Phys. **08**, 003 (2003).

[69] Y. M. Bunkov and G. E. Volovik, Phys. Rev. Lett. **98**, 265302 (2007).

[70] S. Autti, P. J. Heikkinen, G. E. Volovik, V. V. Zavjalov, and V. B. Eltsov, Phys. Rev. B **97**, 014518 (2018).

[71] G. Dvali, F. Kühnel, and M. Zantedeschi, Phys. Rev. Lett. **129**, 061302 (2022).

[72] G. Dvali, O. Kaikov, F. Kühnel, J. S. Valbuena-Bermúdez, and M. Zantedeschi, Phys. Rev. Lett. **132**, 151402 (2024).

[73] V. Makhankov, G. Kummer, and A. Shvachka, Phys. Lett. A **70**, 171 (1979).

[74] M. Axenides, S. Komineas, L. Perivolaropoulos, and M. Floratos, Phys. Rev. D **61**, 085006 (2000).

[75] T. Multamäki and I. Vilja, Phys. Lett. B **482**, 161 (2000).

[76] T. Multamäki and I. Vilja, Phys. Lett. B **484**, 283 (2000).

[77] R. A. Battye and P. M. Sutcliffe, Nucl. Phys. **B590**, 329 (2000).

[78] J. H. Al-Alawi and W. J. Zakrzewski, J. Phys. A **42**, 245201 (2009).

[79] P. Bowcock, D. Foster, and P. Sutcliffe, J. Phys. A **42**, 085403 (2009).

[80] B. Gutierrez, *Relativistic Scattering of Solitons in Nonlinear Field Theory*, Ph.D. thesis, University of British Columbia (2013).

[81] V. Rubakov, *Classical Theory of Gauge Fields*, 1st ed. (Princeton University Press, Princeton, NJ, United States, 2002).

[82] G. Rosen, J. Math. Phys. **9**, 999 (1968).

[83] T. F. Morris, Can. J. Phys. **57**, 2171 (1979).

[84] K. Lee, J. A. Stein-Schabes, R. Watkins, and L. M. Widrow, Phys. Rev. D **39**, 1665 (1989).

[85] C. H. Lee and S. U. Yoon, Mod. Phys. Lett. A **6**, 1479 (1991).

[86] H. Arodź and J. Lis, Phys. Rev. D **79**, 045002 (2009).

[87] T. Tamaki and N. Sakai, Phys. Rev. D **90**, 085022 (2014).

[88] J. Heeck, A. Rajaraman, and C. B. Verhaaren, Phys. Rev. D **104**, 016030 (2021).

[89] J. Heeck, A. Rajaraman, R. Riley, and C. B. Verhaaren, Phys. Rev. D **103**, 116004 (2021).

[90] J. Heeck, A. Rajaraman, R. Riley, and C. B. Verhaaren, J. High Energy Phys. **10**, 103 (2021).

[91] Y. Almumin, arXiv:2404.03053 [hep-th].

[92] A. Rajaraman, arXiv:2406.02817 [hep-th].

[93] I. E. Gulamov, E. Y. Nugaev, and M. N. Smolyakov, Phys. Rev. D **89**, 085006 (2014).

[94] I. E. Gulamov, E. Y. Nugaev, A. G. Panin, and M. N. Smolyakov, Phys. Rev. D **92**, 045011 (2015).

[95] A. G. Panin and M. N. Smolyakov, Phys. Rev. D **95**, 065006 (2017).

[96] A. Y. Loginov and V. V. Gauzshtein, Phys. Rev. D **102**, 025010 (2020).

[97] M. I. Tsumagari, E. J. Copeland, and P. M. Saffin, Phys. Rev. D **78**, 065021 (2008).

[98] A. Tranberg and D. J. Weir, J. High Energy Phys. **04**, 184 (2014).

[99] V. Loiko and Y. Shnir, Phys. Rev. D **106**, 045021 (2022).

[100] M. Mai and P. Schweitzer, Phys. Rev. D **86**, 076001 (2012).

[101] M. Mai and P. Schweitzer, Phys. Rev. D **86**, 096002 (2012).

[102] M. Laue, Ann. Phys. **340**, 524 (1911).

[103] M. V. Polyakov and P. Schweitzer, Int. J. Mod. Phys. A **33**, 1830025 (2018).

[104] V. Benci and D. Fortunato, J. Math. Phys. **52**, 093701 (2011).

[105] V. Benci and D. Fortunato, Chaos Soliton Fract. **58**, 1 (2014).

[106] J.-P. Hong, M. Kawasaki, and M. Yamada, Phys. Rev. D **92**, 063521 (2015).

[107] J.-P. Hong, M. Kawasaki, and M. Yamada, J. Cosmol. Astropart. Phys. **08**, 053 (2016).

[108] J.-P. Hong and M. Kawasaki, Phys. Rev. D **95**, 123532 (2017).

[109] S. Jiang, F. P. Huang, and P. Ko, J. High Energy Phys. **07**, 053 (2024).

[110] A. Kusenko, V. Kuzmin, M. Shaposhnikov, and P. G. Tinyakov, Phys. Rev. Lett. **80**, 3185 (1998).

[111] V. Dzhunushaliev and K. G. Zloshchastiev, Cent. Eur. J. Phys. **11**, 325 (2013).

[112] M. J. Berger and J. Oliger, J. Comput. Phys. **53**, 484 (1984).

[113] U. Trottenberg, C. W. Oosterlee, and A. Schüller, *Multigrid*, 1st ed. (Academic Press, San Diego, CA, United States, 2000).

[114] M. Choptuik, "Lectures for VII Mexican School on Gravitation and Mathematical Physics," http://laplace.phas.ubc.ca/People/matt/Teaching/06Mexico/mexico06.pdf, accessed 2024-07-01.

[115] R. J. LeVeque, *Finite Difference Methods for Ordinary and Partial Differential Equations*, 1st ed. (Society for Industrial and Applied Mathematics, Philadelphia, PA, United States, 2007).

[116] J. Crank and P. Nicolson, Math. Proc. Cambridge Philos. Soc. **43**, 50 (1947).

[117] F. Pretorius, *Numerical Simulations of Gravitational Collapse*, Ph.D. thesis, University of British Columbia (2002).

[118] F. Pretorius and M. W. Choptuik, J. Comput. Phys. **218**, 246 (2006).

[119] L. Richardson, Phil. Trans. R. Soc. A **210**, 307 (1911).

[120] R. L. Marsa, *Radiative Problems in Black Hole Spacetimes*, Ph.D. thesis, University of Texas at Austin (1995).

[121] A. Akbarian Kaljahi, *Numerical Studies in Gravitational Collapse*, Ph.D. thesis, University of British Columbia (2015).

[122] *Maple User Manual* (Maplesoft, 2022).

[123] E. Seidel and W.-M. Suen, Phys. Rev. Lett. **66**, 1659 (1991).

[124] A. Kusenko and A. Mazumdar, Phys. Rev. Lett. **101**, 211301 (2008).

[125] E. Y. Nugaev and A. V. Shkerin, J. Exp. Theor. Phys. **130**, 301 (2020).

[126] B. Kleihaus, J. Kunz, and M. List, Phys. Rev. D **72**, 064002 (2005).

[127] Y. Almumin, J. Heeck, A. Rajaraman, and C. B. Verhaaren, Eur. Phys. J. C **82**, 801 (2022).

[128] B. W. Lynn, Nucl. Phys. **B321**, 465 (1989).

[129] T. Multamäki and I. Vilja, Phys. Lett. B **542**, 137 (2002).

[130] T. Tamaki and N. Sakai, Phys. Rev. D **83**, 044027 (2011).

[131] M. Axenides, E. Floratos, S. Komineas, and L. Perivolaropoulos, Phys. Rev. Lett. **86**, 4459 (2001).

[132] F. P. Correia and M. Schmidt, Eur. Phys. J. C **21**, 181 (2001).

[133] M. N. Smolyakov, Phys. Rev. D **97**, 045011 (2018).

[134] S. H. Hawley and M. W. Choptuik, Phys. Rev. D **62**, 104024 (2000).

[135] D. L. T. Anderson and G. H. Derrick, J. Math. Phys. **11**, 1336 (1970).

[136] A. G. Panin and M. N. Smolyakov, Eur. Phys. J. C **79**, 150 (2019).

[137] D. Levkov, E. Nugaev, and A. Popescu, J. High Energy Phys. **12**, 131 (2017).

[138] A. Cohen, S. Coleman, H. Georgi, and A. Manohar, Nucl. Phys. **B272**, 301 (1986).

[139] J.-P. Hong and M. Kawasaki, Phys. Rev. D **96**, 103526 (2017).

[140] E. Radu and M. S. Volkov, Phys. Rep. **468**, 101 (2008).

[141] B. Schwabe, J. C. Niemeyer, and J. F. Engels, Phys. Rev. D **94**, 043513 (2016).

[142] V. Cardoso, S. Hopper, C. F. B. Macedo, C. Palenzuela, and P. Pani, Phys. Rev. D **94**, 084031 (2016).

[143] Q.-X. Xie, P. M. Saffin, A. Tranberg, and S.-Y. Zhou, J. High Energy Phys. **01**, 165 (2024).

[144] J. W. York Jr. and T. Piran, in *Spacetime and Geometry: The Alfred Schild Lectures*, edited by R. A. Matzner and L. C. Shepley (University of Texas Press, Austin, TX, United States, 1982).

[145] M. Radia, U. Sperhake, A. Drew, K. Clough, P. Figueras, E. A. Lim, J. L. Ripley, J. C. Aurrekoetxea, T. França, and T. Helfer, Class. Quantum Grav. **39**, 135006 (2022).

[146] P. M. Saffin, Q.-X. Xie, and S.-Y. Zhou, Phys. Rev. Lett. **131**, 111601 (2023).

[147] V. Cardoso, R. Vicente, and Z. Zhong, Phys. Rev. Lett. **131**, 111602 (2023).

[148] G.-D. Zhang, F.-M. Chang, P. M. Saffin, Q.-X. Xie, and S.-Y. Zhou, Phys. Rev. D **110**, 043504 (2024).

[149] M. W. Choptuik, Phys. Rev. D **44**, 3124 (1991).

Appendix A

Appendices for Chapter 2

A.1 Evolution Equations in Axisymmetry

Here we present the full set of evolution equations for our model, the boundary conditions used, and the regularity conditions imposed on the axis of symmetry.

The evolution equations for the scalar and gauge fields can be expressed in cylindrical coordinates as

$$\begin{aligned}\partial_t^2\phi_1 = &\frac{1}{\rho}\partial_\rho\phi_1 + \partial_\rho^2\phi_1 + \partial_z^2\phi_1 + 2e\left(-A_t\partial_t\phi_2 + A_\rho\partial_\rho\phi_2 + A_z\partial_z\phi_2\right)\\ &- e^2\phi_1\left(-A_t^2 + A_\rho^2 + A_z^2 + \frac{1}{\rho^2}A_\varphi^2\right) - \frac{1}{2}\partial_{\phi_1}V(\phi_1,\phi_2),\end{aligned} \tag{A.1}$$

$$\begin{aligned}\partial_t^2\phi_2 = &\frac{1}{\rho}\partial_\rho\phi_2 + \partial_\rho^2\phi_2 + \partial_z^2\phi_2 - 2e\left(-A_t\partial_t\phi_1 + A_\rho\partial_\rho\phi_1 + A_z\partial_z\phi_1\right)\\ &- e^2\phi_2\left(-A_t^2 + A_\rho^2 + A_z^2 + \frac{1}{\rho^2}A_\varphi^2\right) - \frac{1}{2}\partial_{\phi_2}V(\phi_1,\phi_2),\end{aligned} \tag{A.2}$$

$$\partial_t^2 A_t = \frac{1}{\rho}\partial_\rho A_t + \partial_\rho^2 A_t + \partial_z^2 A_t + 2e\left(\phi_1\partial_t\phi_2 - \phi_2\partial_t\phi_1\right) - 2e^2\left(\phi_1^2+\phi_2^2\right)A_t, \tag{A.3}$$

$$\partial_t^2 A_\rho = \frac{1}{\rho}\partial_\rho A_\rho + \partial_\rho^2 A_\rho + \partial_z^2 A_\rho - \frac{A_\rho}{\rho^2} + 2e\left(\phi_1\partial_\rho\phi_2 - \phi_2\partial_\rho\phi_1\right) - 2e^2\left(\phi_1^2+\phi_2^2\right)A_\rho, \tag{A.4}$$

$$\partial_t^2 A_\varphi = -\frac{1}{\rho}\partial_\rho A_\varphi + \partial_\rho^2 A_\varphi + \partial_z^2 A_\varphi - 2e^2\left(\phi_1^2+\phi_2^2\right)A_\varphi, \tag{A.5}$$

$$\partial_t^2 A_z = \frac{1}{\rho}\partial_\rho A_z + \partial_\rho^2 A_z + \partial_z^2 A_z + 2e\left(\phi_1\partial_z\phi_2 - \phi_2\partial_z\phi_1\right) - 2e^2\left(\phi_1^2+\phi_2^2\right)A_z, \tag{A.6}$$

where the subscripts $\{t,\rho,\varphi,z\}$ correspond to the spacetime coordinates and the subscripts $\{1,2\}$ correspond to the real and imaginary parts, respectively, of the scalar field ϕ. For

numerical purposes, we find it convenient to define new evolutionary variables

$$\begin{aligned} \Pi_1 &= \partial_t \phi_1, & \Pi_2 &= \partial_t \phi_2, \\ G_t &= \partial_t A_t, & G_\rho &= \partial_t A_\rho, \\ G_\varphi &= \partial_t A_\varphi, & G_z &= \partial_t A_z, \end{aligned} \tag{A.7}$$

which are first-order in time.

To complete our specification of the problem, we must impose appropriate boundary conditions along the axis of symmetry and at the outer domain boundaries $\rho = \rho_{\max}$, $z = z_{\min}$, and $z = z_{\max}$. For the outer boundaries, we apply outgoing boundary conditions of the form

$$\sqrt{\rho^2 + z^2}\, \partial_t f + f + \rho\, \partial_\rho f + z\, \partial_z f = 0, \tag{A.8}$$

where $f = f(t, \rho, z)$ represents each of the evolved variables in (A.1)–(A.7). Strictly speaking, the condition (A.8) assumes the field f is massless and purely radially outgoing at the domain boundary. For non-spherical pulses or massive fields, the approximation can break down and lead to unphysical reflections. However, these partial reflections can be mitigated by taking the outer boundaries sufficiently far away and by stopping the evolution when appreciable field content reaches the boundaries. With these considerations, we find condition (A.8) to be sufficient for the purposes of this work.

Along the axis of symmetry, we find it useful to define the regularized variables

$$\tilde{G}_\rho = \frac{G_\rho}{\rho}, \qquad \tilde{G}_\varphi = \frac{G_\varphi}{\rho^2}. \tag{A.9}$$

With this definition, we identify G_t, $\tilde{G}_\rho$, $\tilde{G}_\varphi$, G_z, Π_1, and Π_2 as having even character as $\rho \to 0$. We can therefore demand that the radial derivative of these fields should vanish in this limit, yielding appropriate regularity (boundary) conditions along the axis of symmetry.

A.2 Code Validation

We have performed a number of tests in order to assess the validity of our numerical code. For all calculations presented in this appendix, we evolve generic Gaussian-like initial data which is smooth everywhere. The fields ϕ_1, ϕ_2, Π_1, Π_2, A_t, $\tilde{A}_\rho$, and A_z are chosen to be arbitrary overlapping profiles of the form

$$f(\rho, z) = A \exp\left[- \left(\frac{\sqrt{(\rho - \rho_0)^2 + (z - z_0)^2}}{\delta} \right)^2 \right], \tag{A.10}$$

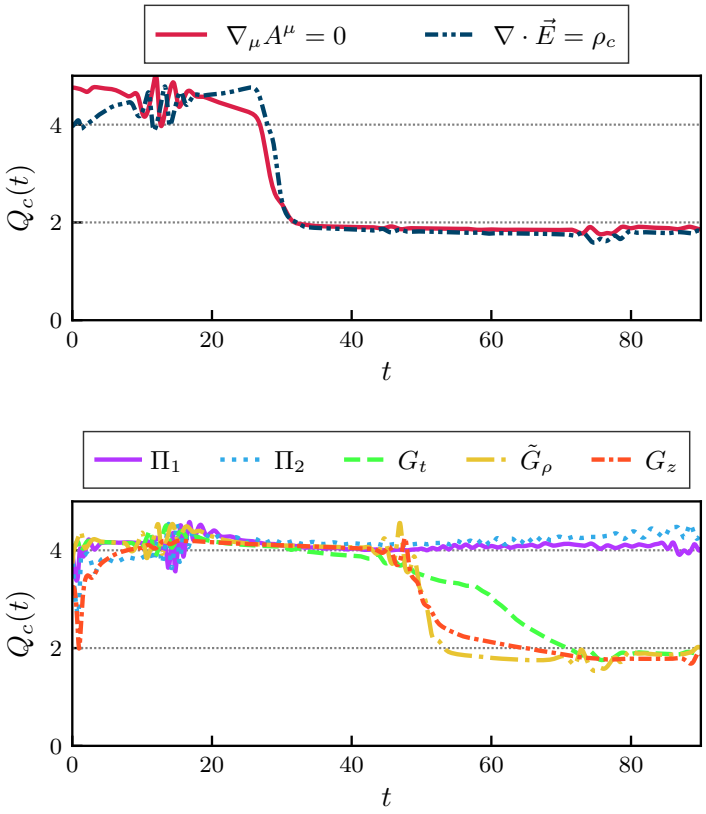

Figure A.1: Convergence factors $Q_c(t)$ for the constraint equations (top) and several first-order evolved variables Π_1, Π_2, G_t, $\tilde{G}_\rho$, and G_z (bottom). Here, $Q_c(t)$ is computed using a three-level convergence test at resolutions 257×513, 513×1025 and 1025×2049. In each case, the quantities are found to be convergent at approximately second-order until the fields hit the boundaries, at which point first-order convergence is observed. For the data shown here, the potential (2.4) is used with parameters $e = 0.25$, $h = 0.2$, and $m = k = 1.0$.

where A, δ, ρ_0 and z_0 are real parameters which can be different for each field. The fields G_t, $\tilde{G}_\rho$, and G_z are then found using a successive over-relaxation scheme [23] in order to approximately satisfy the constraints at the initial time.

As a primary test, we evolve this generic Gaussian-like data on a uniform grid at several different grid resolutions in order to explicitly compute the rate of convergence of our code. Let us define the convergence factor $Q_c(t)$ as

$$Q_c(t) = \frac{\|u^{4h} - u^{2h}\|}{\|u^{2h} - u^{h}\|}, \tag{A.11}$$

where h represents the spacing between points on the numerical grid, u^n represents the solution computed with grid spacing n, and $\|\cdot\|$ denotes the L_2-norm. For a second-order-accurate finite-difference scheme, it can be shown that $Q_c(t) \to 4$ as $h \to 0$. In Figure A.1,

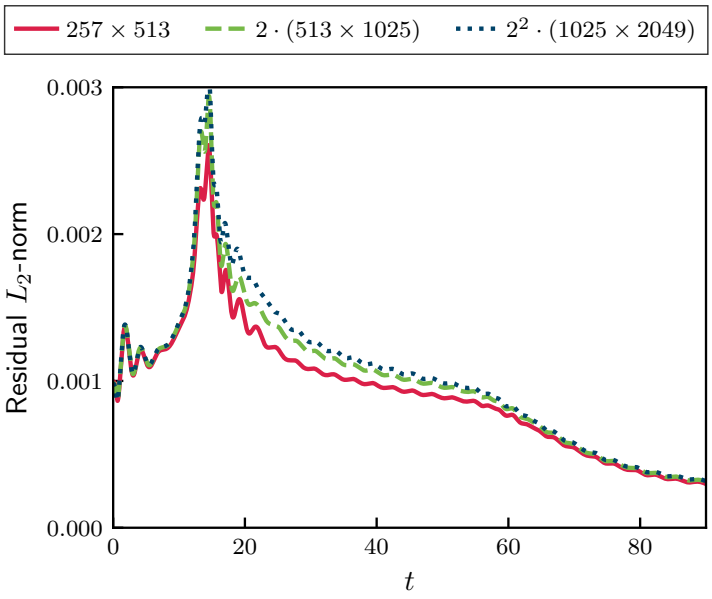

Figure A.2: Residual L_2-norm values for the evolution equation (A.1) computed at several different grid resolutions. The L_2-norm has been scaled by factors of 2^n for increasing resolutions. Overlapping of the curves indicates the expected first-order convergence of the residuals.

we plot the convergence factor resulting from our test for the constraint equations and several representative fields. The rate of convergence is found to be approximately second-order (corresponding to $Q_c(t) = 4$) which is to be expected for our second-order Crank-Nicolson finite-difference implementation.

As a secondary measure, we have performed an independent residual test [114] to verify that our discrete numerical solution is converging to the true continuum solution of the underlying system (A.1)–(A.6). For this test, we substitute the numerical solution found via the second-order Crank-Nicolson discretization into a separate first-order forward discretization of the evolution equations. Results of this test are shown in Figure A.2. The residuals are found to approximately overlap when rescaled by factors of 2^n, indicating the expected first-order convergence. For brevity, only the (A.1) residual is presented here—other residuals are found to be similar.

In solving the equations of motion, we have used a free evolution scheme wherein a solution to the evolution equations is expected to solve the constraint equations at the initial time [149]. However, it is possible for constraint violation to grow during the course of the evolution, indicating lack of convergence. The degree to which the constraints are violated is therefore a relative measure of the error in the numerical solution. In all of our simulations, we monitor the L_2-norm of the constraint residuals to ensure that they

do not grow significantly over the timescales explored. For the results reported here, the L_2-norm of the constraint residuals remains within $O(10^{-4})$. In addition, we also monitor the integrated total energy E and the charge Q during the course of the evolution to confirm that these quantities remain approximately conserved to within $O(1\%)$.

Appendix B

Appendices for Chapter 3

B.1 Supplemental Figures

To supplement the figures presented in the main text, here we provide additional plots which illustrate several interesting cases of gauged Q-ball dynamics.

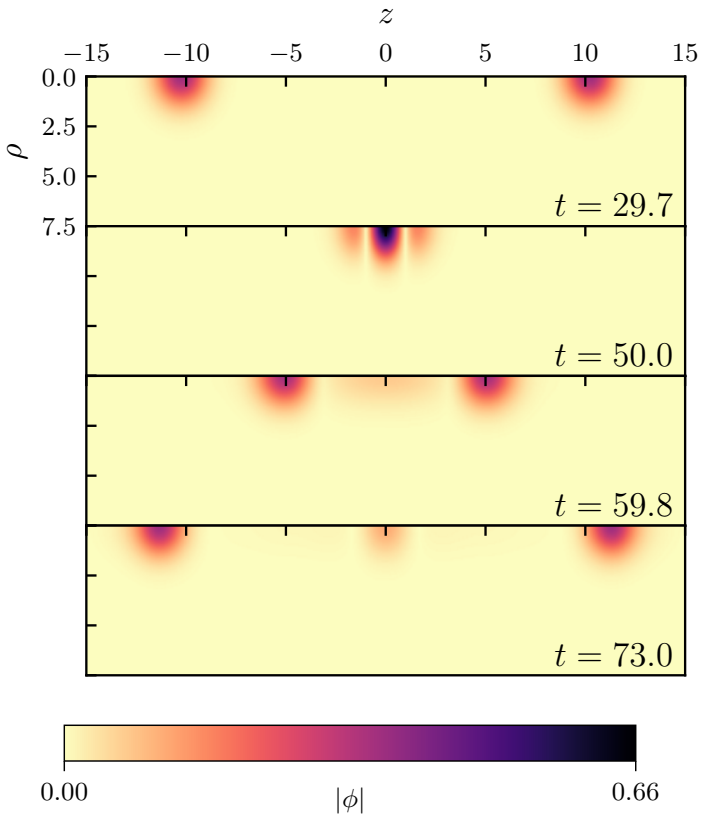

Figure B.1: Evolution of the scalar field modulus $|\phi|$ for a collision of solutions of type LogA with equal charge, velocity $v = 0.5$, and phase difference $\alpha = 0$. The Q-balls collide at $t \approx 50$ and pass through each other, leaving behind a smaller Q-ball remnant which remains perturbed at the origin.

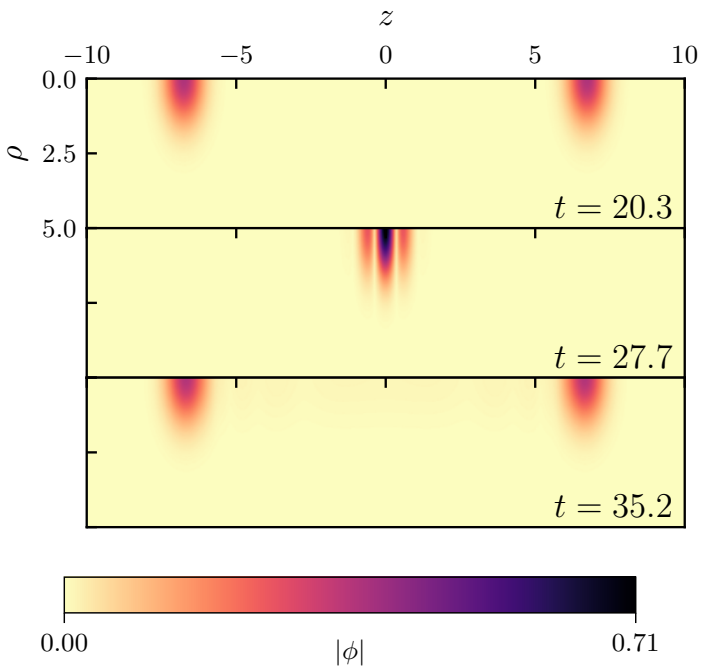

Figure B.2: Evolution of the scalar field modulus $|\phi|$ for a collision of solutions of type LogA with equal charge, velocity $v = 0.9$, and phase difference $\alpha = 0$. The Q-balls collide at $t \approx 27$ and exhibit a destructive interference pattern. After the collision, the Q-balls emerge with profiles nearly identical to their initial state.

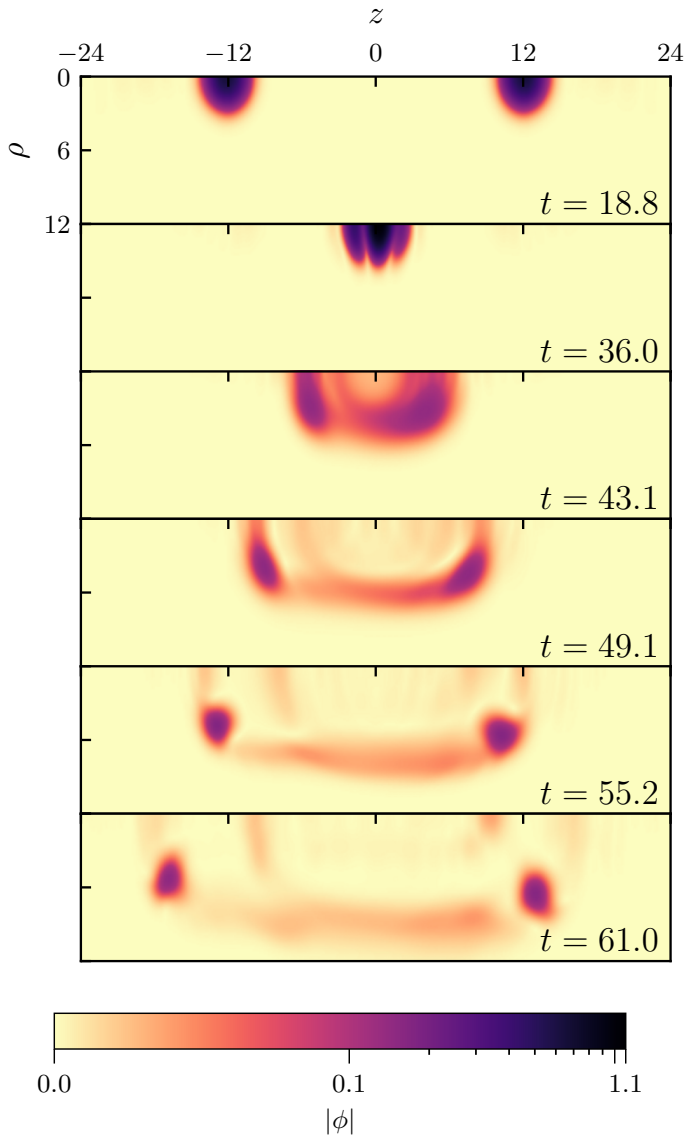

Figure B.3: Evolution of the scalar field modulus $|\phi|$ for a collision of solutions of type LogC with equal charge, velocity $v = 0.7$, and phase difference $\alpha = \pi/4$. The Q-balls collide at $t \approx 36$. After the collision, the field content predominantly takes the form of two Q-rings. In this case, the phase difference manifests as an asymmetry in the dynamics about the plane $z = 0$. Note that a hybrid colormap is used: field values below $|\phi| = 0.1$ are mapped linearly to zero while values above this threshold are mapped logarithmically to the field maximum.

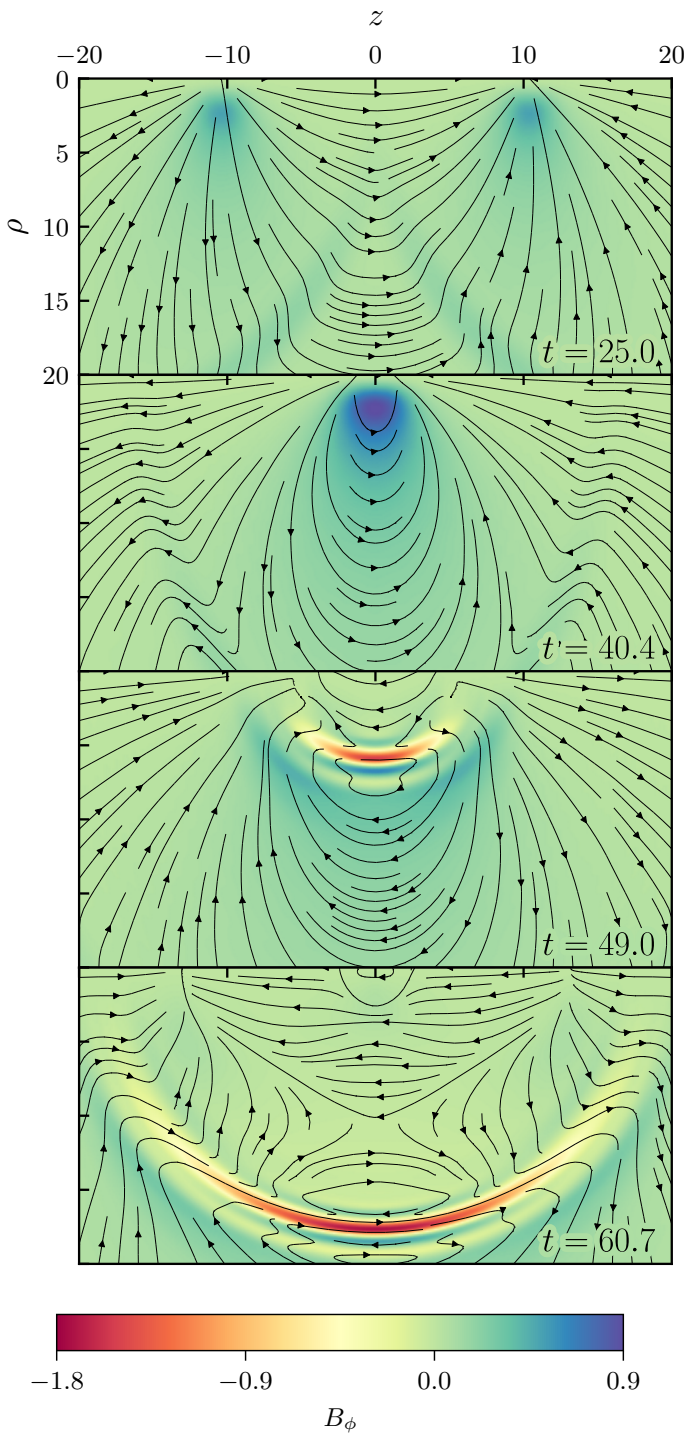

Figure B.4: Evolution of the electric field $\vec{E}$ and the magnetic field $\vec{B}$ for a collision of solutions of type LogC with opposite charge, velocity $v = 0.6$, and phase difference $\alpha = 0$. The magnitude of the only non-zero component of the magnetic field, B_ϕ, is represented using the colormap. The orientation of the electric field is represented using streamlines; the corresponding field magnitude is not reflected in the figure. The Q-balls collide at $t \approx 40$ and partially annihilate charge. After the collision, the fields resemble an outgoing wavefront. We note that the small-scale "pulse" which is visible for $\rho \gtrsim 10$ in the first and second panel exists as a technical artefact of the gauged Q-ball initialization procedure at $z = \pm 25$.

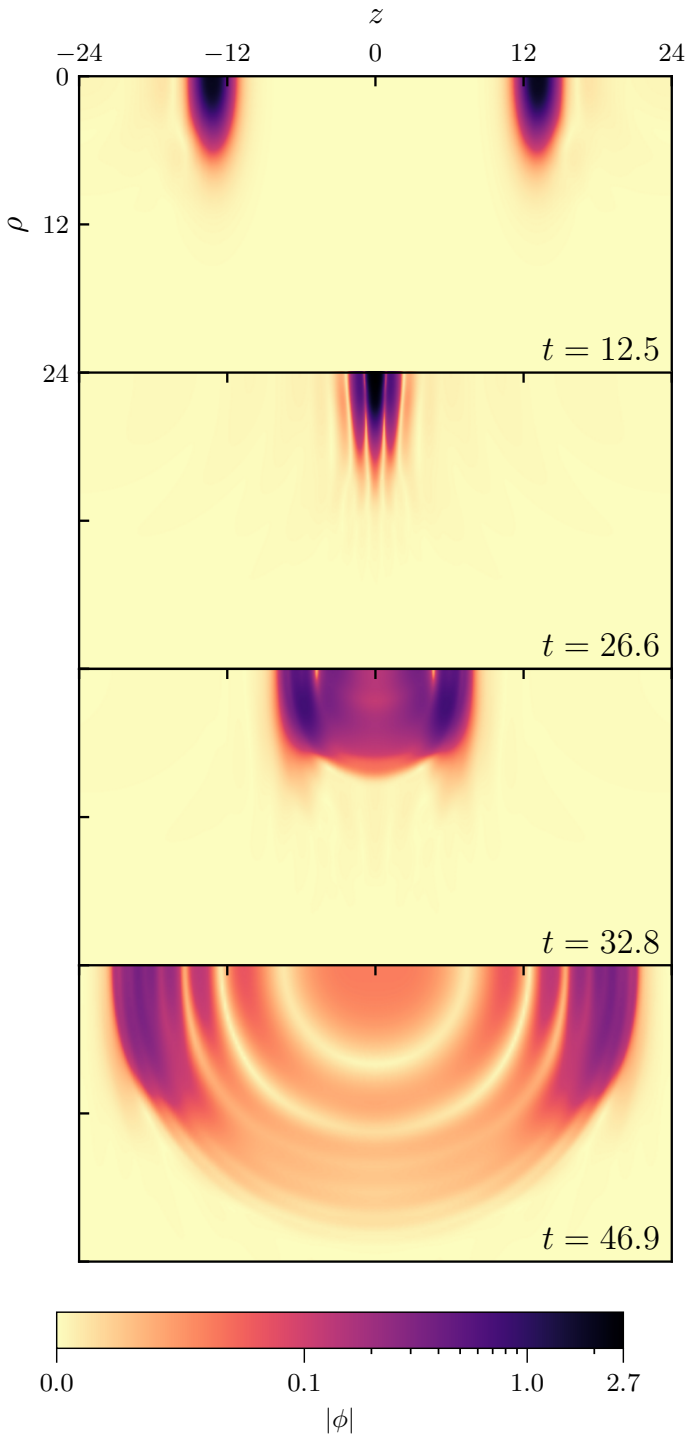

Figure B.5: Evolution of the scalar field modulus $|\phi|$ for a collision of solutions of type PolyB with equal charge, velocity $v = 0.95$, and phase difference $\alpha = 0$. The Q-balls collide at $t \approx 26$ and form a destructive interference pattern. After the collision, the majority of the field content continues travelling along the axis of symmetry and becomes elongated in the radial direction. Note that a hybrid colormap is used: field values below $|\phi| = 0.1$ are mapped linearly to zero while values above this threshold are mapped logarithmically to the field maximum.

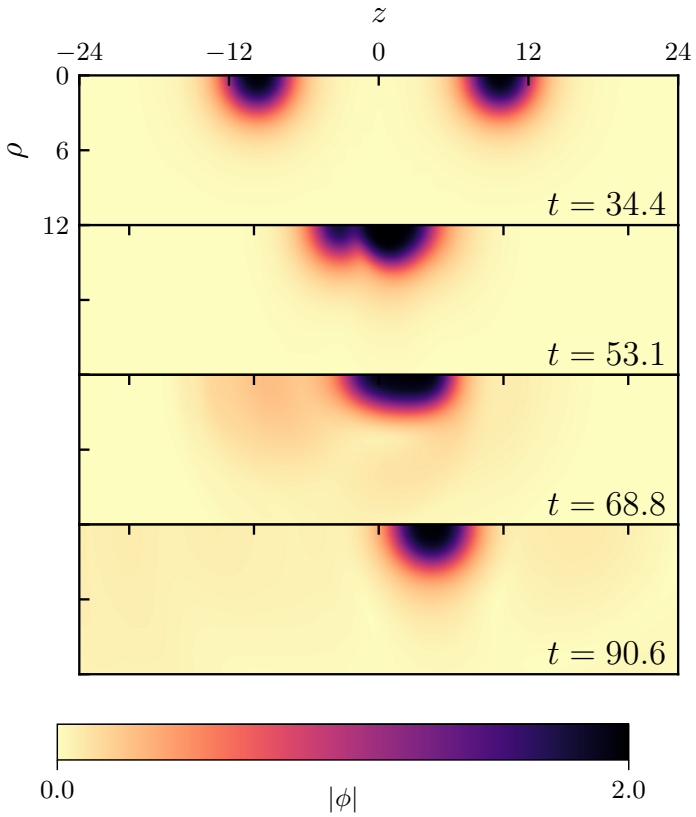

Figure B.6: Evolution of the scalar field modulus $|\phi|$ for a collision of solutions of type PolyB with equal charge, velocity $v = 0.45$, and phase difference $\alpha = \pi/4$. The Q-balls collide at $t \approx 53$ and transfer charge (as can be seen in the second panel). After the collision, the smaller Q-ball created in this process quickly dissipates while the larger Q-ball travels slowly along the axis of symmetry.

Appendix C

Appendices for Chapter 4

C.1 Evolution Equations in Three Spatial Dimensions

When expressed using the coordinates defined by (4.7), the evolution equations for the system (4.2)–(4.3) take on the following form:

$$\begin{aligned}\partial_t^2\phi_1 = \partial_x^2\phi_1 + \partial_y^2\phi_1 + \partial_z^2\phi_1 + 2e\left(-A_t\partial_t\phi_2 + A_x\partial_x\phi_2 + A_y\partial_y\phi_2 + A_z\partial_z\phi_2\right) \\ - e^2\phi_1\left(-A_t^2 + A_x^2 + A_y^2 + A_z^2\right) - \frac{1}{2}\partial_{\phi_1}V(\phi_1,\phi_2),\end{aligned} \tag{C.1}$$

$$\begin{aligned}\partial_t^2\phi_2 = \partial_x^2\phi_2 + \partial_y^2\phi_2 + \partial_z^2\phi_2 - 2e\left(-A_t\partial_t\phi_1 + A_x\partial_x\phi_1 + A_y\partial_y\phi_1 + A_z\partial_z\phi_1\right) \\ - e^2\phi_2\left(-A_t^2 + A_x^2 + A_y^2 + A_z^2\right) - \frac{1}{2}\partial_{\phi_2}V(\phi_1,\phi_2),\end{aligned} \tag{C.2}$$

$$\partial_t^2 A_t = \partial_x^2 A_t + \partial_y^2 A_t + \partial_z^2 A_t + 2e\left(\phi_1\partial_t\phi_2 - \phi_2\partial_t\phi_1\right) - 2e^2\left(\phi_1^2 + \phi_2^2\right)A_t, \tag{C.3}$$

$$\partial_t^2 A_x = \partial_x^2 A_x + \partial_y^2 A_x + \partial_z^2 A_x + 2e\left(\phi_1\partial_x\phi_2 - \phi_2\partial_x\phi_1\right) - 2e^2\left(\phi_1^2 + \phi_2^2\right)A_x, \tag{C.4}$$

$$\partial_t^2 A_y = \partial_x^2 A_y + \partial_y^2 A_y + \partial_z^2 A_y + 2e\left(\phi_1\partial_y\phi_2 - \phi_2\partial_y\phi_1\right) - 2e^2\left(\phi_1^2 + \phi_2^2\right)A_y, \tag{C.5}$$

$$\partial_t^2 A_z = \partial_x^2 A_z + \partial_y^2 A_z + \partial_z^2 A_z + 2e\left(\phi_1\partial_z\phi_2 - \phi_2\partial_z\phi_1\right) - 2e^2\left(\phi_1^2 + \phi_2^2\right)A_z. \tag{C.6}$$

Here, the subscripts $\{t, x, y, z\}$ correspond to the spacetime coordinates while the subscripts $\{1, 2\}$ denote the real and imaginary parts of the scalar field, respectively. In deriving (C.1)–(C.6), we have invoked the Lorenz gauge condition (4.8) as a means to simplify the equations. After applying the coordinate transformations (4.24)–(4.26), we solve these equations using the fourth-order finite-difference scheme described in Section 4.3.3 together with the initial data procedure of Section 4.3.1.

C.2 Code Validation

In order to assess the validity of our code, we have performed a series of numerical tests of convergence. In these tests, we use generic Gaussian-like initial data which approximately satisfies the constraint equations (4.9)–(4.10) at the initial time. We evolve the data on a uniform grid at various resolutions and compute the convergence factor $Q_c(t)$ as

$$Q_c(t) = \frac{\|u^{4h} - u^{2h}\|}{\|u^{2h} - u^{h}\|}. \tag{C.7}$$

Here, h represents the spacing between grid points, u^n represents the solution computed with grid spacing n, and $\|\cdot\|$ denotes the L_2-norm. For a finite-difference scheme with $O(h^m)$ accuracy, one expects to find $Q_c(t) \to 2^m$ as $h \to 0$ [114]. We therefore expect to observe $Q_c(t) \approx 16$ for the fourth-order finite-difference scheme described in Section 4.3.3. In the top panel of Figure C.1, we plot the results of this test for the real part of the scalar field, ϕ_1, computed in the polynomial model (4.6) with $e = 0.5$, $h = 0.2$, and $m = k = 1$. Using grid resolutions of 65^3, 129^3, and 257^3 to compute $Q_c(t)$ in (C.7), we find that the implementation is convergent to approximately fourth-order, as we expect. In addition to ϕ_1, we have also repeated this test for all other evolved quantities in the equations of motion (C.1)–(C.6). We find similar fourth-order behaviour in each case.

As a secondary test, we have performed an independent residual evaluation [114] to verify that our numerical solution reasonably approximates the continuum solution of the problem. In this test, the solution obtained using our fourth-order finite-difference scheme is substituted into a separate second-order centered discretization of the equations of motion (C.1)–(C.6). If the residuals of these equations converge away at second-order in the grid spacing (corresponding to rescaling by factors of four), we conclude that the original finite-difference scheme has been correctly implemented. The results of this test are shown in the bottom panel of Figure C.1. Once again, we use grid resolutions of 65^3, 129^3, and 257^3 and pick equation (C.1) as a representative example. In the figure, we observe the expected convergence of the residual at second-order; the residuals for the other evolution equations (C.2)–(C.6) are found to behave in a similar way. This provides an additional check of the validity of our implementation.

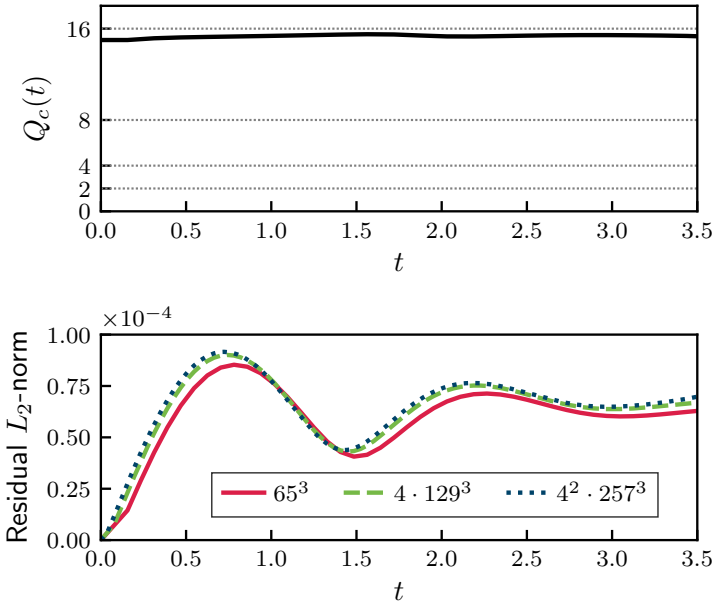

Figure C.1: Representative results for a three-level convergence test (top panel) and independent residual test (bottom panel) of the finite-difference implementation described in Section 4.3.3. In the top panel, the convergence factor $Q_c(t)$ is computed for the evolved variable ϕ_1. In the bottom panel, the L_2-norm for the independent residual of equation (C.1) is computed at grid resolutions of 65^3, 129^3 and 257^3. In both cases, the implementation is found to be convergent at the expected order.